Supplementary Materials for

Design of Polymeric Zwitterionic Solid Electrolytes with Superionic Lithium Transport

Authors: Seamus D. Jones[1,2,3], Howie Nguyen[4], Peter M. Richardson[2,3], Yan-Qiao Chen[2,5], Kira E. Wyckoff[2,4], Craig J. Hawker[2,4,5], Raphaële J. Clément[2,3,4], Glenn H. Fredrickson[1,2,3,4], Rachel A. Segalman[1,2,3,4*]

Affiliations:

[1]Department of Chemical Engineering, University of California, Santa Barbara, California, United States

[2]Materials Research Laboratory, University of California, Santa Barbara, California, United States

[3]Mitsubishi Chemical Center for Advanced Materials, University of California, Santa Barbara, California, United States

[4]Materials Department, University of California Santa Barbara, Santa Barbara, California, United Sates

[5]Department of Chemistry and Biochemistry, University of California, Santa Barbara, California, United States

*Corresponding author. Email: segalman@ucsb.edu,

Pages S1-S92

Tables S1-S17

Figures S1-S60

Contents

1 Materials and Methods

1.1 Chemicals

Acrylic acid N-hydroxy succinimide ester (NHS ester acrylate), trifluoromethanesulfonamide, and Sodium 3-Bromopropanesulfonate were purchased from TCI chemicals. The monomer was stored in a refrigerated compartment of a nitrogen containing glovebox until needed. Cyanomethyl dodecyl trithiocarbonate (CDDTC), aminopropyl imidazole, triethylamine (TEA), 3-Bromopropanesulfonic acid sodium salt, and 2,2′-Azobis(2-methylpropionitrile) (AIBN), and dimethylaminoethyl acrylate (DMAEA) were purchased from Sigma Aldrich. Diethyl ether (DEE), methanol (MeOH), tetrahydrofuran (THF), dichloromethane (DCM), and dimethylformamide (DMF) were purchased from Fisher chemicals. Lithium bis(trifluoromethanesulfonyl)imide (Li TFSI) was purchased from Solvonic and stored in a glove box until its use. Anhydrous casting solvents were purchased from Sigma Aldrich and placed and stored in a nitrogen containing glovebox before penetration of the sureseal container. AIBN was recrystallized 3x in methanol to yield white needle-like crystals which were stored at 0 °C.

1.2 Synthesis of poly(NHS-ester acrylate)

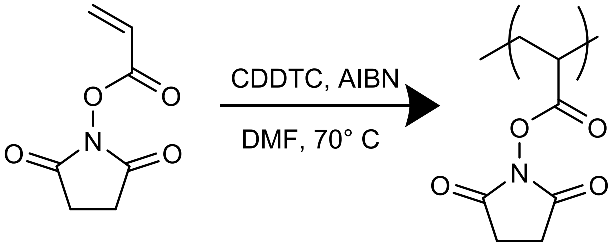

Controlled polymerization of poly(NHS ester acrylate) was performed via Reversible Addition Fragmentation Chain Transfer (RAFT) Polymerization as described by (Evans et al.). 5.246 g of NHS ester acrylate (31.01 mmol, 253 eq.), 39.0 mg of CDDTC (0.123 mmol 1 eq.), and 3.3 mg of AIBN (0.02 mmol, 0.16 eq.) were added to 10 mL of DMF in a 100 mL round bottom flask with a Teflon stir bar. The solution was sparged under stirring with Nitrogen gas and placed in a thermostated oil bath at 70°C for 18 hours. An aliquot for analysis was taken before the reaction began and immediately before quenching the reaction solution by placing the flask in an ice bath and opening the reactor to ambient conditions.

1.3 Synthesis of poly(N-(3-(1H-imidazol-1-yl)propyl)acrylamide)

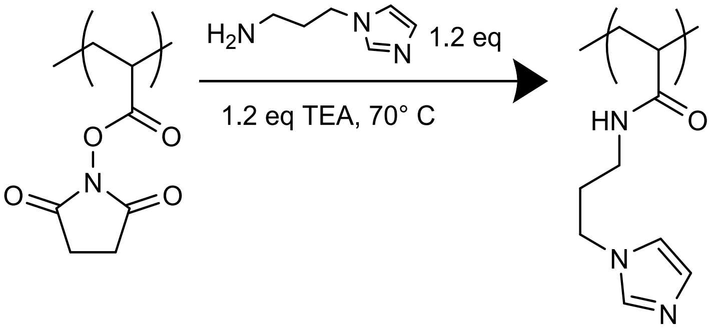

After quenching the polymerization, 1.2 eq. (relative to the monomer) of Aminopropyl imidazole (4.658 g) and TEA (3.761 g) were added to the polymerization reactor. The reaction mixture was returned to the thermostated bath (70°C) for another 24 hours under stirring. Over this period a small amount of white solid (TEA salts) precipitated from solution. The solution was filtered to remove this solid and subsequently precipitated into 100 mL of DEE to yield a viscous yellow fluid. This fluid was redissolved in THF and precipitated again in DEE. The product was collected and dried in vacuo to yield a yellow solid.

1.4 Synthesis of ((3-bromopropyl)sulfonyl)((trifluoromethyl)sulfonyl)amide triethylamine salt (TFSI-Br)

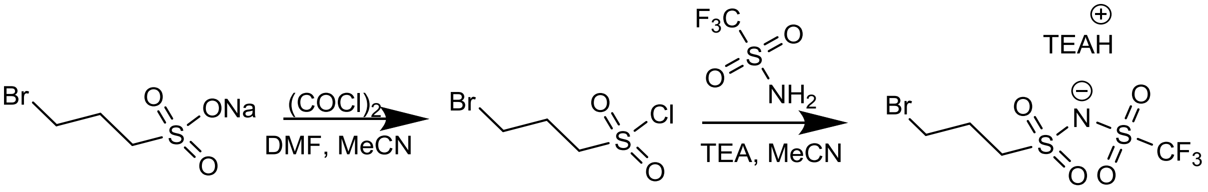

A Schlenk flask with a Teflon coated stir bar was charged with 1 g of 3-Bromopropanesulfonic acid sodium salt. Vacuum was pulled on the powder till the vacuum reached a baseline of ~10^{-2} torr and the solution was repressurized with nitrogen. 5 mL of anhydrous acetonitrile was added to the flask and stirred rapidly to form a suspension. Meanwhile, a second flask was charged with 5mL acetonitrile and 0.68 g (1.2 eq.) oxalyl chloride and placed under an active nitrogen sparge. After a few minutes of degassing, a catalytic (several drops) quantity of dry DMF was added to the flask. This flask was stirred for 30 minutes and adopted a yellowish color. After the activation of the oxalyl chloride, the Schlenk flask containing the suspension of the sulfonic acid was chilled to 0°C and the oxalyl chloride solution was added dropwise. The solution was allowed to slowly warm to room temperature overnight leaving a yellowish solution with a white crystalline precipitate. The liquid phase was transferred via syringe to a new Schlenk flask, leaving behind the precipitate. The precipitate was washed with an additional of 3mL of dry acetonitrile to capture additional entrained product. This wash was also syringe transferred to the same Schlenk flask.

A third Schlenk flask was charged with trifluoromethanesulfonamide 0.66 g (1 eq.) and dried to baseline before adding anhydrous TEA 0.79 g (3 eq.) and 2 mL of anhydrous acetonitrile. This solution was stirred for several minutes and added dropwise via cannula to the sulfonyl chloride containing flask at 0 °C. The addition of this solution resulted in immediate formation of white precipitate. This flask was stirred and allowed to reach room temperature overnight. After the overnight rest, the quantity of precipitate increased and the solution had turned brownish-yellow color. This solution was filtered to remove the salts and concentrated by rotatory evaporation to yield a brown oil. This oil was diluted in DCM and washed with distilled water and a dilute aqueous hydrogen chloride solution (0.5 M), in a separatory column. The organic layer was dried over magnesium sulfate and further dried in vacuo to yield a viscous brown oil. Conversion was verified by ^{1}H and ^{19}F NMR spectroscopy. ^{1}H NMR (600 MHz, Chloroform-d) 3.64 (t, J = 6.4 Hz, 1H), 3.27 – 3.21 (t, J = 7.4 Hz, 1H), 3.15 (qd, J = 7.3, 4.9 Hz, 6H on a triethylamine basis), 2.29 – 2.21 (m, 1H), 1.29 (t, J = 7.3 Hz, 9H on a triethylamine basis).

1.5 Quaternization of poly(N-(3-(1H-imidazol-1-yl)propyl)acrylamide) to Polyzwitterion (Im-TFSI PZIL)

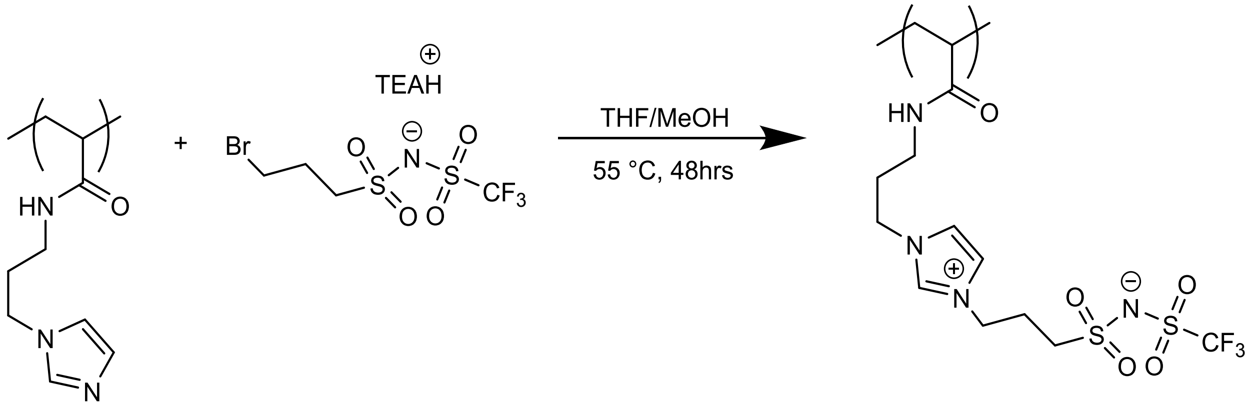

2 g of the dried polymer was redissolved in 8 mL of a 1/1 v/v mixture of THF and MeOH along with 1.5 eq. of Br-TFSI-TEA. The solution was sealed and heated to 55 °C for 48 hours. After 48 hours the solution was concentrated by rotatory evaporation and precipitated into isopropanol to yield a brown solid. The solid was thoroughly washed with IPA, redissolved in DMF and dialyzed (8 kDa Mw cutoff) against MeOH for 5 days with a solvent exchange once per day. The bulk solution remained optically clear even after contact with dialysis solution for 24 hrs. The final product was precipitated one final time in DEE to collect a brown leathery solid. This product was dried in vacuo for 48 hours at 80 °C before salt incorporation. BigSmiles representation: OC(=O)C(C)(C){[<]CCC(=O)NCCCn1cc[n+](CCCS(=O)(=O)[N-]S(=O)(=O)C(F)(F)F)c1[>]}SC(=S)SCCCCCCCCCCCC

1.6 Salt Incorporation

Li$^+$/TFSI$^-$ salts were incorporated into the PZIL by solution casting. In a nitrogen containing glovebox, polymer was dissolved in anhydrous MeOH and a stock solution of Li$^+$/TFSI$^-$ salt in anhydrous MeOH was prepared via gravimetric measurements. Salt concentration was controlled by volumetric addition of stock solution via a positive displacement micropipette. The solutions were blended until all components were mutually soluble and subsequently flash frozen in liquid nitrogen and placed in vacuo to remove solvent. Polymers were dried for 24 hours at ~10^{-3} torr in a vacuum oven at room temperature, then for an additional 24 hours at 70°C. These materials were transferred to an ultra-high vacuum oven at 10^{-8} – 10^{-9} torr for 24 hours at 55 °C and finally transferred to a nitrogen-containing glovebox for all storage and sample preparation. Salt concentration is parameterized by the molar ratio, 'r', of salt to zwitterionic residue (r=[Li$^+$/TFSI$^-$]/[ZI]).

1.7 Synthesis of 3-(1-ethyl-1H-imidazol-3-ium-3-yl)propane-1-sulfonate (SO_3-Imidazole ZIL)1.8 Synthesis of ((3-(1-ethyl-1H-imidazol-3-ium-3-yl)propyl)sulfonyl)((trifluoromethyl)sulfonyl)amide (TFSI-Imidazole ZIL)

0.4 g of 1-Ethyl-imidazole and 2.1 g of TFSI-Br were added to a vial along with 10 mL of acetonitrile and a stir bar. The solution was heated to 60°C under stirring for 96 hours. Stirring, the product was worked up first by precipitation 2x in isopropanol, resulting in a dark viscous liquid. This liquid was subsequently washed repeatedly with dichloromethane until the DCM phase appeared to absorb no color from the wash. After washing with DCM, a brown powdery product was isolated. The powder was dried in a vacuum oven at 70°C for 48 hours before transferring to a glovebox for all handling. ^{1}H NMR (600 MHz, DMSO-d6) δ 9.16 (s, 1H), 7.78 (s, 2H), 4.28 (t, J = 7.1 Hz, 2H), 4.16 (q, J = 7.3 Hz, 2H), 2.99 (t, J = 7.4 Hz, 2H), 2.27 – 2.06 (p, J=7.2 Hz 2H), 1.40 (t, J = 7.3 Hz, 3H). ^{13}C NMR (151 MHz, dmso) δ 136.40, 122.81, 122.69, 51.52, 47.81, 44.70, 25.30, 15.31.

1.8 Synthesis of poly(dimethylamino ethyl acrylate) (PDMAEA)

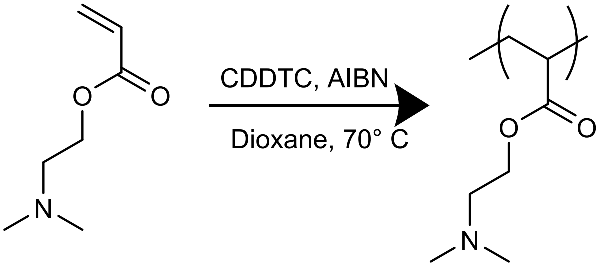

DMAEA was polymerized using standard RAFT techniques. DMAEA monomer was passed through a basic alumina plug to remove inhibitor immediately prior to use (note: it can be difficult to remove inhibitor from this monomer and a second plug was used to attain a clear-colored monomer). The monomer (14.6 g, 0.102 mol, 250 eq.) was added to a heavy-walled and oven-dried reaction flask along with a stir bar, DDMAT (0.148 g, 0.41 mmol, 1eq.), and AIBN (7mg, 0.04 mmol, 0.1 eq.) and 30mL of 1,4 dioxane. The reaction mixture was sparged with nitrogen and submerged in a thermostated oil bath at 70°C under moderate stirring. The reaction was allowed to proceed for 18 hours before quenching by submerging the reactor in an ice bath and exposing the reaction mixture to air. The polymer was purified by precipitation twice in cyclohexane and dried in vacuo to yield a viscoelastic liquid.

1.9 Quaternization of PDMAEA to Polyzwitterion with TFSI Anion (Am-TFSI-PZIL)

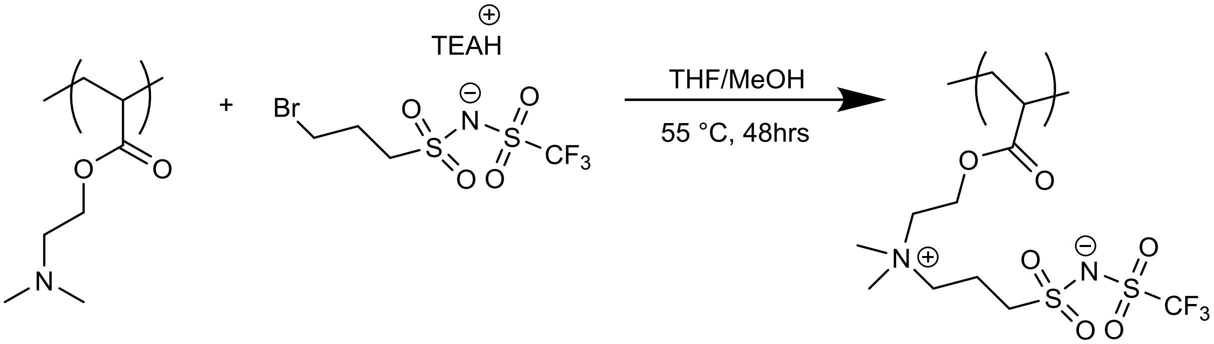

2 g of the dried polymer was redissolved in 8 mL of a 1/1 v/v mixture of THF and MeOH along with 1.5 eq. of Br-TFSI-TEA. The solution was sealed and heated to 55 °C for 48 hours. After 48 hours the solution was concentrated by rotatory evaporation and precipitated into

isopropanol to yield a brown solid. The solid was thoroughly washed with IPA, redissolved in DMF and dialyzed (8 kDa Mw cutoff) against MeOH for 5 days with a solvent exchange once per day. The bulk solution remained optically clear even after contact with dialysis solution for 24 hrs. The final product was precipitated one final time in DEE to collect a brown leathery solid. This product was dried in vacuo for 48 hours at 80 °C before salt incorporation.

1.10 Synthesis of ((3-chloropropyl)sulfonyl)((perfluorophenyl)sulfonyl)amide triethylamine salt (Cl-TFS-C6F5)

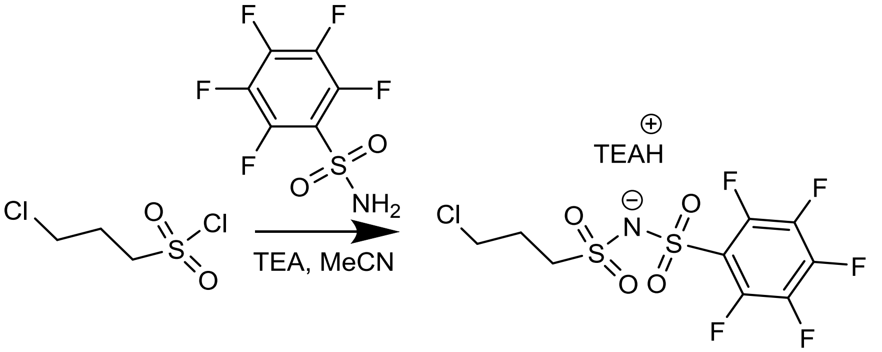

A Schlenk flask was charged with pentafluorophenylsulfonamide [1.02 g, 4.1 mmol] and dried to baseline before adding anhydrous TEA [1.73 mL, 12.4 mmol] and 5 mL of anhydrous acetonitrile. Sulfonyl chloride [0.5 mL, 4.1 mmol] was added dropwise to this stirring solution at 0 °C. The addition of the sulfonyl chloride resulted in immediate formation of a white precipitate. This flask was stirred and allowed to reach room temperature overnight. After the overnight rest, the quantity of precipitate increased and the solution had turned brownish-yellow color. This solution was filtered to remove the salts and concentrated by rotatory evaporation to yield a brown oil. This oil was diluted in DCM and washed with distilled water and a dilute aqueous hydrogen chloride solution (0.5 M), in a separatory column. The organic layer was dried over magnesium sulfate, solvent removed in vacuo to yield a viscous brown oil and used in the subsequent step without further purification. Conversion was verified by ^{1}H and ^{19}F NMR spectroscopy. ^{1}H NMR (600 MHz, Chloroform-d) δ 3.70 (t, J = 6.4 Hz, 2H), 3.33 (t, J = 7.3 Hz, 2H), 3.19 (qd, J = 7.3, 4.8 Hz, 6H on TEA Basis), 2.35 (tt, J = 13.8, 13.5, 7.5, 7.2 Hz, 2H), 1.38 (t, J = 7.3 Hz, 9H on TEA Basis). ^{19}F NMR (564 MHz, cdcl3) δ -79.05, -116.72, -117.24.

1.11 Quaternization of PDMAEA to Zwitterion with TFS Anion with Pentafluoro Group

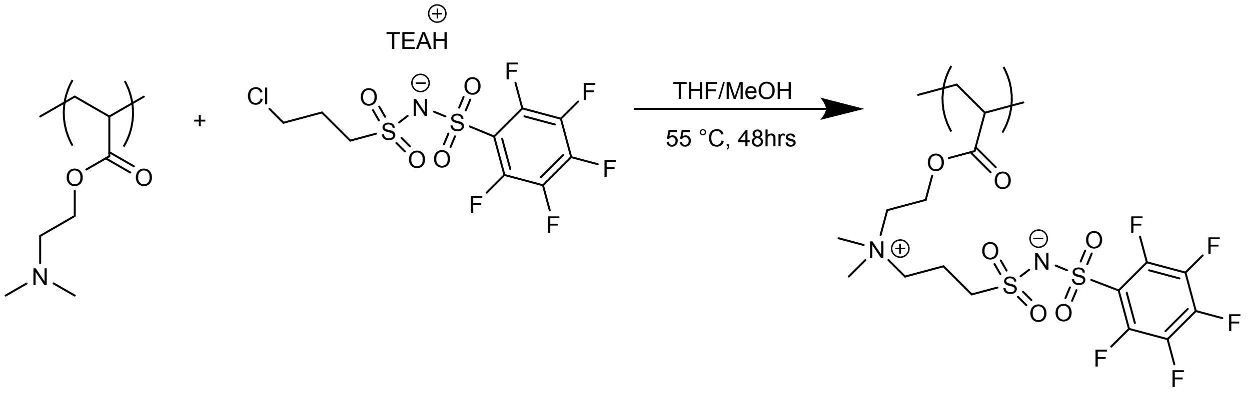

0.277 g of the dried polymer was redissolved in 4 mL of a 1/1 v/v mixture of Acetonitrile and MeOH along with 1.5 eq. of Cl-TFS-C6F5-TEAH (1 g). The solution was sealed and heated to 55 °C for 48 hours. After 48 hours the solution was concentrated by rotatory evaporation and precipitated into isopropanol to yield a brown solid. The solid was precipitated and thoroughly washed with IPA. This product was dried in vacuo for 48 hours at 80 °C before salt incorporation.

1.12 Rheological Studies

Rheological measurements were made on an ARES-G2 strain-controlled rheometer manufactured by TA instruments. Stainless steel 8 mm parallel plates were used for all measurements. Samples were prepared for rheology by compression molding into a disc mold before loading. Rheology samples were further compressed at 70 °C and 5N of force on the rheometer instrument. During operation all samples were enclosed in a nitrogen-purged oven chamber. Final sample thicknesses were maintained within a range of 0.3-0.5 mm. All measurements were made in the 'linear regime' as determined via strain sweep measurements. Temperature-dependent frequency measurements were performed as a sequence of experiments with 5 minutes of soak time between steps. To investigate long-time responses of the materials a stress relaxation experiments was also performed, however the terminal region could not be located.

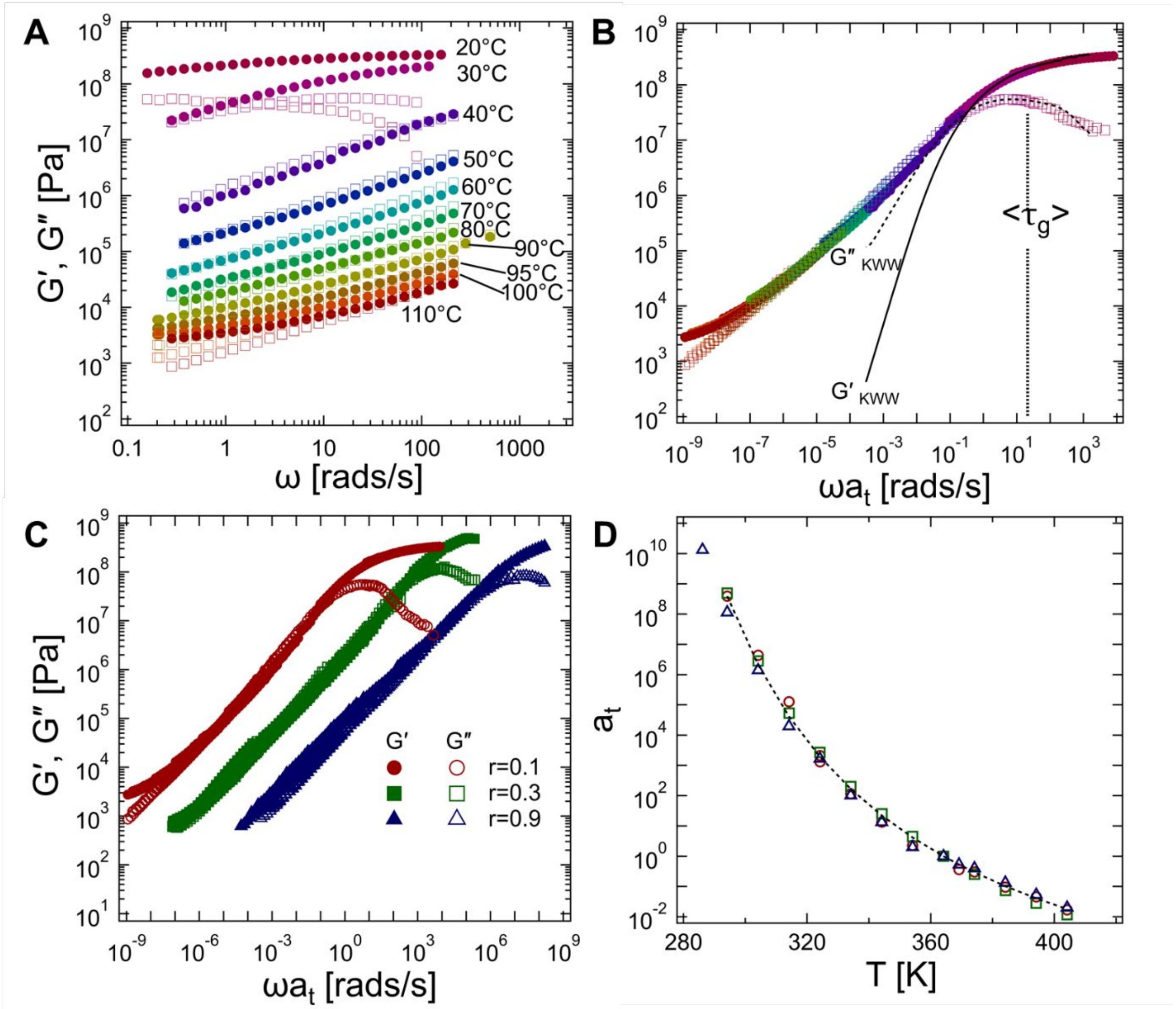

Figure S1: A) Individual frequency sweep curves from the r=0.1 zwitterionic system with closed symbols representing the storage modulus (G′) and open symbols representing the loss modulus (G″). B) The master curve for the r=0.1 system generated by shifting in frequency only and generated at a reference temperature of 303K. Solid and dotted fit lines correspond to the fitting of the glassy region to the KWW relation (Equation 1), which provides a phenomenological description of the glass transition. The marked τ_g curve represents the mean glassy relaxation timescale as estimated by the KWW fit. C) Master curves for all salt loaded polymers display similar behavior. The reference temperature of the r=0.1 curve is 303K, the r=0.3 and r-0.9 were selected at the same reference temperature and shifted by factors of 10^3 and 10^6 respectively so they can be more easily visualized in a single figure. D) The shift factor versus temperature curves for all salt loadings with a reference temperature of 90° C.

Since the structural relaxation rate generally plays a critical role in dictating the ionic conductivity of an electrolyte, it is useful to evaluate the ionic conduction performance of a material in the context of its structural relaxation rate. Frequently, the calorimetrically-determined glass transition temperature is the sole metric of polymer dynamics and ionic conductivity is classified in terms of the temperature difference from T_g i.e., ‘$T-T_g$’. This simplistic treatment of polymer dynamics is insufficient for fundamental studies of ion conduction as it cannot account for the nonlinear temperature dependence of polymer dynamics. Consequently, it is important to contextualize ion dynamics in terms of measured ion dynamic timescales.

Linear viscoelastic measurements are a robust means of assessing the temperature-dependence of polymer dynamics. Figure S1A shows individual frequency sweeps at small oscillatory strains of the r = 0.1 PZIL at various temperatures. Transformation of these curves by time-temperature superposition (TTS) yields the master curve shown in Figure S1B. Although TTS does not rigorously apply to thermo-rheologically complex materials, these master curves are nonetheless useful in determining dynamics over a broad range of frequencies. The master curve in Figure 1b displays typical glassy behavior at high effective frequencies (ωa_T) with a plateau in the storage modulus in the gigapascal regime and a local maximum in the loss modulus. This glassy regime was fit by the Kohlrausch-Williams-Watts (KWW) expression for the time-dependent modulus G(t) (Equation 1), a common phenomenological model for the glassy relaxation of polymers, which has been expressed in terms of its first moment, τ_g, corresponding to the average timescale of segmental rearrangement (note: fitting was performed in frequency space as described in our previous work[1], fitting utilized the 'libkww' library which provides an approximation for the Fourier transform of stretched exponential functions[2]). The 'β' parameter in this expression corresponds to the breadth of the glass transition, approaching unity in the case of a uniform relaxation and broadening as it approaches zero. The reference temperature in Equation 1 is the same as the reference temperature used to generate TTS curves (303 K). This glass transition is followed at longer effective times by a collective relaxation with scaling behavior $G' \approx G'' \sim \omega^{0.5}$ and finally, a long-lived plateau that is confirmed by stress relaxation experiments (Section S8). This relaxation scaling behavior and plateau is consistent with a percolated network of ionic crosslinks that results in long-lived elastic behavior[3], though detailed analysis of the viscoelastic behavior of the system is beyond the scope of this study.

$$G(t, T = T_{ref}) = G_g(0)\exp\left[-\left(\frac{t\Gamma(\beta^{-1})}{\tau_g(T_{ref})\beta}\right)^{\beta}\right] \qquad \text{Eqn. S1}$$

This construction and fitting of the master curves (S1.C) enables determination of the segmental relaxation timescale and its temperature dependence, $\tau_g(T)$, which is critical in understanding the overall polymer dynamics. Equation S2 illustrates the procedure used to generate the $\tau_g(T)$ function where $a_T(T)$ corresponds to the shift factor functions in Figure S1D. These functions are used to generate the Walden plot (Figure 1E).

$$\tau_g(T) = \tau_g(T_{ref})a_T(T) \qquad \text{Eqn. S2}$$

1.13 Density Measurements

The densities of materials were estimated from weighing discs of the material that were produced by the melt pressing techniques described in 1.10. The discs of material were never exposed to air during the measurements to prevent complications from water uptake.

1.14 X-ray Scattering

Samples were placed on a Kapton film suspended across a stainless-steel washer and were dried and annealed in an inert atmosphere at 80 °C. These samples were transferred to a glovebox where they were sealed in a nitrogen atmosphere. Measurements were conducted at the

National Synchrotron Light Source II (NSLS-II, beamline 11-BM, Brookhaven National Laboratory) with an X-ray energy of 13.5 keV and beam exposures of 10 seconds. Wide-angle x-ray scattering measurements were taken at two detector distances and combined to generate a single image.

1.15 Polymer Melt Pressing

Polymer melt pressing was accomplished using the VCM Essentials tool manufactured by MeltPrep. This melt press tool makes use of a vacuum compressive force to melt samples into well defined disc geometries in the absence of air. Polymers were melt pressed at a temperature of 50°C using the standard lid, which applies 16.5 bar of compaction pressure to the sample. Polymer samples were allowed to cool without active cooling and the geometry was disassembled in the glovebox. For the small molecule zwitterion samples, the processing temperature was set at 170°C. An ultra-low pressure lid setup was used, which applies <0.3 bar of pressure to the sample. After 3 minutes, the sample was transferred to active cooling. The ZIL samples were allowed to fully cool and rest for >48 hours before removing the separation foils. This cooling allowed the ZIL to crystallize completely to a dark solid material.

1.16 Blocking Electrode Electrochemical Impedance Spectroscopy Measurements

Electrochemical impedance spectroscopy (EIS) measurements were performed on polymer samples measured in a through-plane disc geometry with gold blocking electrodes. Electrodes were cleaned prior to use by subsequent 5-minute sonication steps in deionized water, isopropanol, and acetone followed by a 5-minute UV/ozone treatment. In a nitrogen containing glovebox, a disc of polymer was punched out from a uniform film and placed onto the clean electrodes. The polymer was sized to cover the entire electrode area so that no capacitive contribution from spacer materials could contribute to the measurement. The thickness of the electrolyte was monitored with a Mahr 1087R micrometer, which offers resolution to the nearest +/- 0.002 inches. The electrolyte was heated to 120°C and compressed with a spring. Once the thickness remained stable for 20 minutes, the electrode assembly was placed into a controlled environment sample holder (CESH) manufactured by BioLogic, sealed under nitrogen in the glovebox, and placed in an integrated temperature stage (ITS). The temperature of the stage was monitored during measurement by a thermocouple which was placed in contact with the sample slide. EIS sweeps were performed at temperatures ranging from -30 to 115 °C with 10 minutes of isothermal hold time after the set temperature was reached. Potentiostatic EIS was performed with a frequency range of 1 MHz to 10 mHz and an amplitude of 100 mV, which was found to correspond to the linear region of behavior. A second reverse sweep (from low to high frequency) was performed to check for hysteresis, which was not found to play a significant role. Temperature was sampled from low to high temperatures, incrementing 5°C every measurement and then the experiments were repeated in a reverse Temperature ladder (stopping at room temperature). No significant hysteresis effects associated with the temperature ramp were found. The sample cell was unloaded in the glovebox and the thickness of the electrolyte was measured with a micrometer. Differences in the initial and final thicknesses were less than 1% changes in every case. The dc-ionic conductivity was taken to be the value of the real part of the conductivity (σ') at the maximum in the loss tangent (see Section S4 for raw EIS curves). We note here that, in light of the sluggish crystallization dynamics of this material as observed by DSC, there may be a time-dependent element to the ionic conductivity of these materials as the structure evolves, here we report the initial properties of the PZILs after they are annealed and leave any studies regarding their long-term performance to future works.

1.17 Differential Scanning Calorimetry

Differential scanning calorimetry (DSC) measurements were performed on a TA Instruments DSC 2500. Approximately 6 mg of each polymer sample was weighed and loaded into aluminum ‘Tzero’ pans with hermetically sealed lids. All samples were heated to 160° on an initial heating cycle and cooled to -80°C. Glass transition measurements were recorded on the second heating cycle at a ramp rate of 20°C/minute. The glass transition temperature was analyzed via the midpoint analysis method.

1.18 Solid State NMR:

NMR measurements were performed on a Bruker 300 MHz super wide bore ultrashield spectrometer using a Diff50 probe. NMR samples were prepared inside an Argon-containing glovebox by loading the polymer inside a 4 mm alumina rotor. The rotor is then placed in an airtight 5 mm Young’s valved NMR tube. Resonant frequencies of 116.6 MHz and 282.4 MHz were used for ^{7}Li and ^{19}F, respectively. Chemical shift calibrations were done using 1 M NaF (Aq) (-118 ppm) and 1 M LiCl (Aq) (0 ppm). 90° pulse durations were calibrated to be 15.4 µs (16.2 kHz) at 100 W and 11.25 µs (22.2 kHz) at 50 W for ^{7}Li and ^{19}F, respectively. T_1 relaxation times were measured using a standard saturation recovery pulse sequence. The temperature was controlled using a N2 flow rate of 800 L hr^{-1}. 1D spectra were measured with a standard 90^{o} pulse and acquire sequence with a recycle delay of around $5 \cdot T_1$.

Pulse-field gradient NMR was performed using a standard Bruker diffusion pulse sequence (diffste), with stimulated echo pulses to protect the signal from shorter relaxation times in these solid-like samples. Diffusion constants could only be measured at 90°C for Li^+ (^{7}Li) but was measured for 90°C to 60°C for TFSI$^-$ (^{19}F), where short relaxation times were the limiting factor for measurement. The gradient strength, gradient duration, and diffusion time were varied for each measurement to acquire the full decay curve.

1.19 Size Exclusion Chromatography

Size exclusion chromatography was performed on a Waters instrument using a refractive index detector and Agilent PL gel 5 µm MiniMIX-D column. THF at 35 °C was used as the mobile phase with a flow rate of 1.0 mL/min. Polydispersity was determined against narrow polystyrene standards (Agilent).

1.20 Uniaxial Extension Experiments

Precut and premeasured strips of polymer film were loaded into a DMA 850 instrument manufactured by TA instruments with a tension clamp geometry installed. The oven was closed after loading the sample and a nitrogen purge stream was used to equilibrate the sample temperature at 25 °C for 5 minutes. The sample was prestrained to a force of 0.1N and the initial sample length was recorded at the prestrained sample length. After prestraining, the sample was deformed at a constant strain rate of 1mm/minute in accordance with a protocol defined by ASTM D1708. Due to the limited deformation range of the instrument, the samples could not be strained to break, but were strained to the maximum deformation length of the instrument before the run was terminated. The Young’s modulus (E) of the materials was calculated using the slope of the initial deformation. The toughness of the materials cannot be directly estimated since the samples were not fractured during extension, but numerical integration of the experimental data using a cubic spline was used to establish a lower bound for the toughness of the materials.

1.21 ZIL X-Ray Diffraction Experiments

X-ray diffraction of the crystalline ZIL was performed on a disc of powder which had been compressed at 5 tons of ram force. This disc was placed onto a zero-background silicon plate and loaded into an Empyrean XRD Diffractometer. The x-ray energy wavelength was 1.54 Å.

1.22 Limiting Current Measurements

Lithium-lithium symmetric cells containing the polymer electrolyte were prepared to measure the PZIL's transference number. The electrolyte was first melt pressed as described in S1.10. Lithium foils were purchased from Sigma Aldrich and a punch was used to obtain circular electrodes. A cell was assembled within the CESH (controlled environment sample holder) assembly, illustrated in Figure S2, with lithium electrodes and a gold-coated steel current collector.

These cells were allowed to rest overnight before loading into the ITS temperature-controlled chamber. The cells were heated up to 83°C and allowed to equilibrate for 4 hours. After 4 hours, the open-circuit voltage of the cell was measured and was found in all cases to have a magnitude of <1mV. An unbiased EIS step was run prior to polarization with a wide frequency range (5 MHz to 10 mHz). After a 30-minute rest step the polarization was initiated. Cells were first polarized at 20 mV (this small voltage acts as a small disturbance and is not anticipated to result in any significant electrochemical reaction), and a constant potential was then applied across the cell until a steady state was reached. Every 20 minutes an EIS step was performed with a bias equal to the polarization potential of the cell. This step used a small sinus amplitude (10 mV) and a smaller frequency range (1MHz to 1Hz) to minimize the distortion of the polarization curve. Once the cell reached a constant equilibrated current, a final unbiased EIS step was taken over a larger frequency range again.

1.23 Single-crystal Structural Analysis

Large single crystals of the TFSI-Imidazolium-ZIL were prepared by 3x recrystallization of the ZIL compound in hexanes and placed in vacuo for storage until the measurement could be made. After 3 recrystallizations, the ZIL maintained the slight brown color that was characteristic of all polymers used in the study. The persistent coloration despite the high purity inherent to large single-crystalline product is evidence that any discolored impurity is scant in these materials. The single crystals were analyzed using a Kappa Apex II Diffractometer with active nitrogen flow to prevent uptake of water by the ZIL.

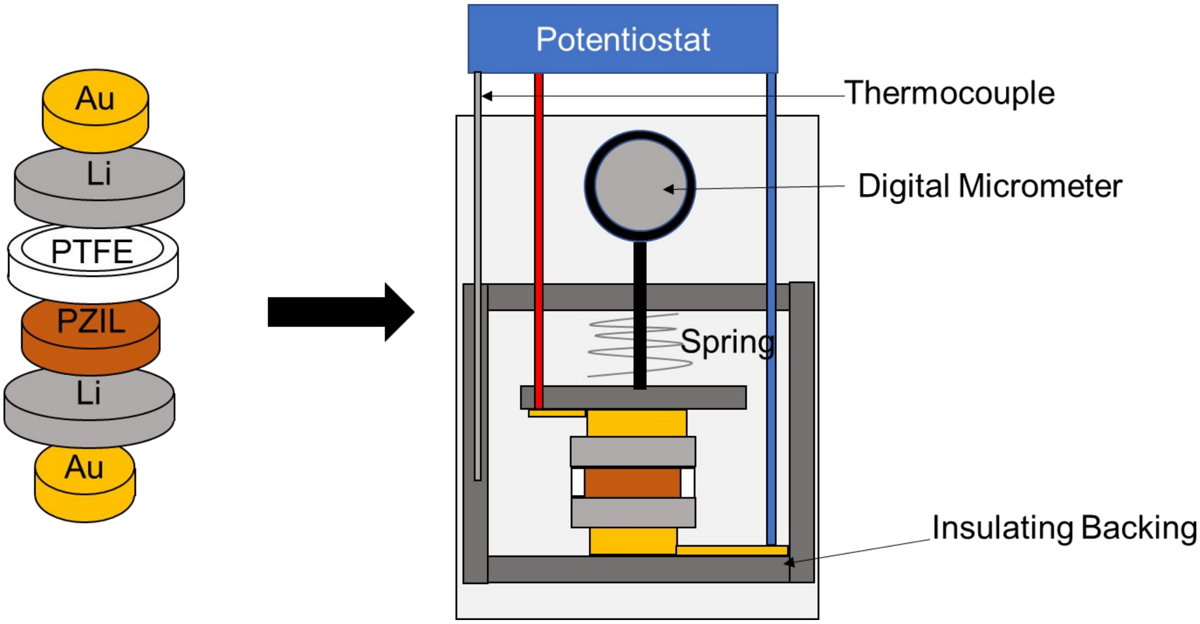

Figure S2: Limiting current measurements are performed using gold-plated steel current collectors and lithium electrodes. A PTFE spacer is used to set the thickness of the cell stack during testing, as well as to contain the PZIL sample. During measurement, the cell assembly is loaded into an inert-gas environment with temperature control.

1.24 Thermogravimetric Analysis

Thermogravimetric analysis (TGA) was performed on the materials to monitor their thermal stability and to confirm removal of volatiles. TGA was performed using a TA instruments Discovery TGA with an aluminum hangdown pan and an Aluminum oxide crucible. Sample masses of ~2mg were loaded into pre-tared crucibles in an air environment. The samples were exposed to a thermal ramp of 10°C/minute from room temperature to 600°C under an inert nitrogen atmosphere.

1.25 Electrochemical Stability Testing

The electrochemical stability of the PZIL electrolyte was tested through galvanostatic cycling of a lithium half-cell composed of a composite PZIL cathode and a lithium metal anode. The composite PZIL cathode was prepared by hand mixing the PZIL with carbon additives and PTFE binder in a 72:18:10 ratio by mass. Cathodes were punched out with loadings between 5.5 mg cm^{-1} and 8.0 mg cm^{-1}. Electrochemical tests were carried out using a Swagelok cell, a Whatman GF/D glass fiber separator, a 1 M $LiPF_6$ in ethylene carbonate and dimethylcarbonate (50/50 by volume, Sigma Aldrich) electrolyte, and a lithium foil anode (Sigma Aldrich). Two cells were prepared to gauge stability at high and low voltages separately, and cycled at a rate of 2.5 mA per gram of PZIL.

1.26 Safety

Oxalyl chloride or $(COCl)_2$ is a compound which can present hazards to unaware users. Though it is well known that this compound can react violently with water, it is not as well known that the same effect may be produced in nonaqueous environments if steps are not taken to contain the reaction. The reaction steps for Swern-Oxidation should be followed as described above with the formation of the catalytically active $(COCl)_2$ prepared in a separate flask from the reactor containing the sulfonate. DMSO should be used in catalytic quantities during this reaction to prevent any violent reaction. Further the addition of the active oxalyl chloride to the sulfonate should take place at low temperature, high dilution, and slow addition rates since the reaction is highly spontaneous.

2 Limiting Current Fraction Analysis Using Symmetric Li/Li Cells

Although limitations such as electrode polarization limit the lengthscales that are probed by MHz electrochemical impedence spectroscopy to lenthscales comparable to the size of the electrical double-layer of the electrode, truly long-range ion transport much be accomplished in order to extract usable ionic current from an electrolyte. The Balsara-Bruce-Vincent type electrochemical measurements presented in this section are used as a simultaneous demonstration of DC ionic conduction in the presence of lithium plating and stripping reactions as well as a measure of the portion of current in the electrochemical cell which can be attributed to lithium motion. We note that, despite modern critiques[4], these experiments represent the state-of-the-art method to understand the selectivity of polymer electrolytes. Although advanced electrophoretic NMR techniques may be able to give a more complete picture of transport in electrolytes, these methods have not been well validated in polymer electrolytes.

2.1 Analysis of EIS Data obtained on Li/Li symmetric cells containing the Im-TFSI PZIL r=0.9 electrolyte

The EIS scan collected on the Li/Li symmetric cell contains contributions from interfacial resistance as well as the bulk resistance of the Im-TFSI PZIL r=0.9 electrolyte. Consequently, an appropriate equivalent circuit contains two R/Q elements, as shown in Figure S3.

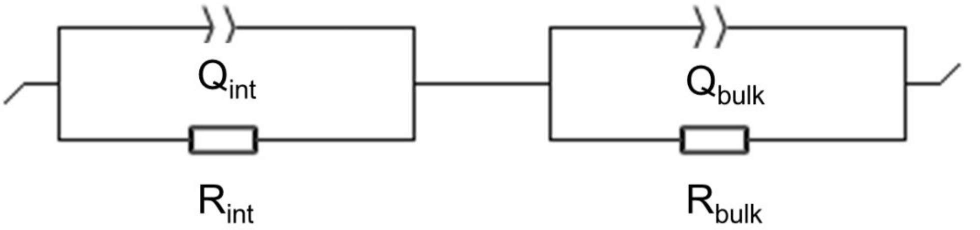

Figure S3: The Equivalent circuit model used to fit the EIS data in the Bruce-Vincent cell.

The above model is used to fit the EIS data collected prior to the start of the polarization experiments, and at 20-minute intervals during the experiment. Figure S4 shows a Cole-Cole representation of the data prior to polarization and after a steady current was reached. The parameters used to generate the fitting functions are given in Table S1.

Table S1: Values of Equivalent Circuit Fitting Parameters Before and After Polarization

	$\mathbf{Q_{int}}$ $[\mathbf{nF \cdot s^{a_{int} - 1}}]$	$\mathbf{R_{int}}$ $[\mathbf{k\Omega}]$	$\mathbf{a_{int}}$ $[-]$	$\mathbf{Q_{bulk}}$ $[\mathbf{pF \cdot s^{a_{bulk} - 1}}]$	$\mathbf{R_{bulk}}$ $[\mathbf{k\Omega}]$	$\mathbf{a_{bulk}}$ $[-]$
Before Polarization	2.8_{05}	1.3_{016}	0.78_{15}	$18._{61}$	1.0_{442}	0.91_{24}
After Polarization	5.5_{98}	2.2_{257}	0.60_{63}	9.5_{5}	1.0_{765}	1.0

Henceforth, the values of these EIS fitting parameters are denoted with a subscript ‘0’ when they refer to values measured prior to polarization, and with a subscript ‘ss’ when they refer to post-polarization values. A rise in the interfacial resistance is observed during the polarization process, but the bulk resistance remains largely unchanged. Although large changes in the impedance spectra are not observed, these small changes may be suggestive of some slight instability of the Li|PZIL interface. The electrochemical stability of the electrolyte is further discussed in S5.

For this cell, the cell area was 6.283 mm^2 and the cell thickness was 0.492 mm. This corresponds to a bulk ionic conductivity before polarization of 0.75 mS/cm, a value which is in relatively good agreement with the blocking electrode conductivity at this temperature of 0.89 mS/cm. These values are in good agreement and do not differ by greater than the experimental uncertainty of fitting.

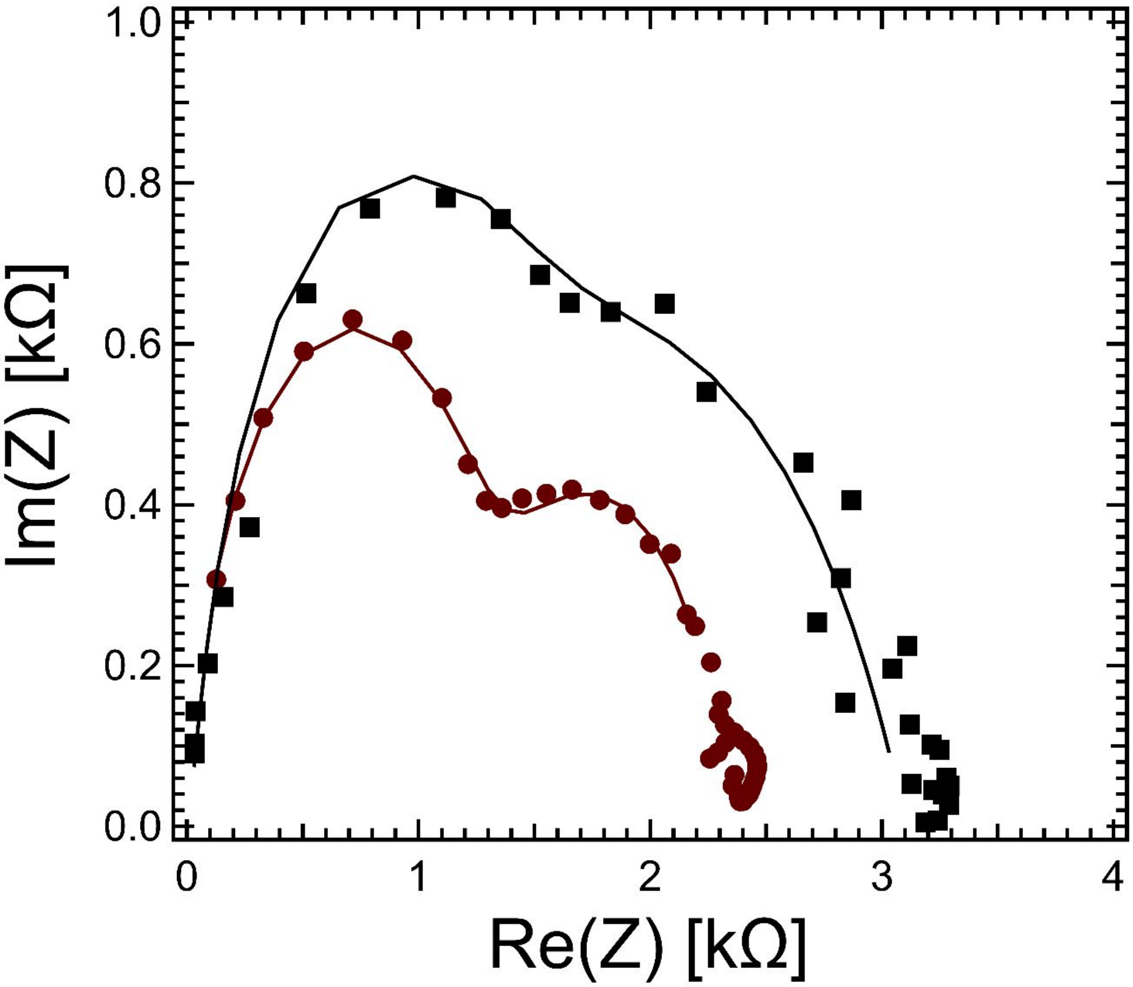

Figure S4: The EIS spectrum of the polymers before (red circle) and after (black square) polarization of the cell. The markers indicate the measured points, and the solid lines indicate the fits to the equivalent circuit using the model depicted in Figure S3 and the parameters in data table S1.

2.2 Analysis of Polarization Current for Im-TFSI PZIL of r=0.9

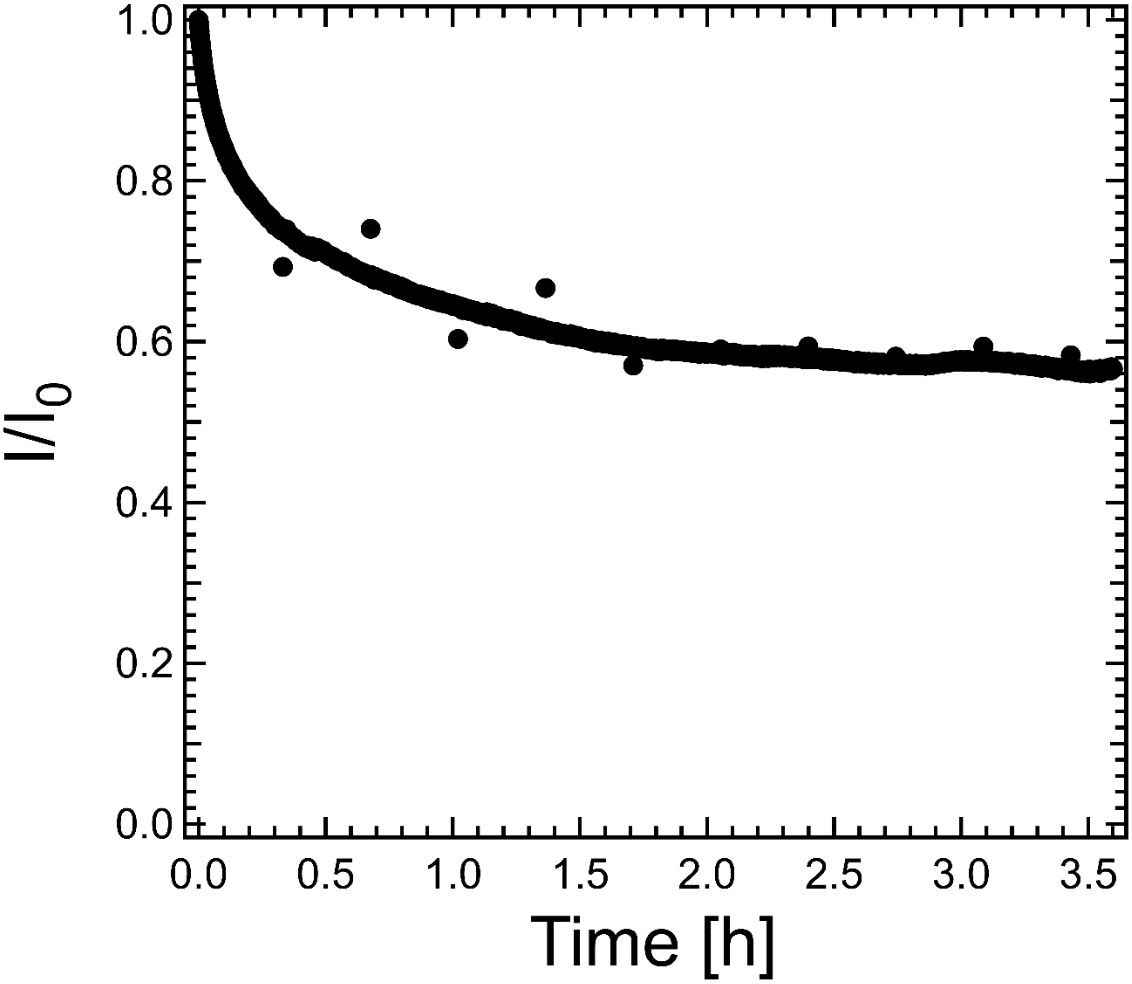

Figure S5: Normalized current versus time graph of the cell undergoing polarization. In this case, the initial current I_0 (8.33 μAmperes) observed experimentally, and the calculated value of I_Ω (8.53 μAmperes), differ somewhat due to the delay between sampling the current and applying the polarization.

The normalized current of the cell is shown above. Equilibration of the cell takes 1-2 hours, which is consistent with other reports, though this equilibration time may vary based on factors such as the cell geometry and conductivity of the electrolyte. Outlier points can be observed after each EIS step due to small disturbances in the voltage of the cell from the oscillating voltage applied during EIS.

The limiting current fraction is computed using Equation S3:

$$\rho_{+,0} = \frac{I_{ss}(\Delta V - I_0 R_{int,0})}{I_0(\Delta V - I_{SS} R_{int,SS})} \qquad \text{Eqn. S3}$$

Where, in accordance with Balsara and coworkers, ρ_+ is used to define the limiting current fraction of the cell. The additional subscript of $\rho_{+,0}$ is used to clarify that this limiting current measure is based on the initial current measurement before polarization, I_0. Since the current may rapidly decay in the first several seconds of measurement, a slightly more accurate measure of the limiting current can be determined using Equation S4:

$$\rho_{+,\Omega} = \frac{I_{ss}(\Delta V - I_{\Omega} R_{int,0})}{I_{\Omega}(\Delta V - I_{SS} R_{int,SS})} \qquad \text{Eqn. S4}$$

Where I_{Ω} is defined in Equation S5:

$$I_{\Omega} \equiv \frac{\Delta V}{R_{int,0} + R_{bulk,0}} \qquad \text{Eqn. S5}$$

We compute both estimates of the limiting current fraction, and we see a moderate difference using the two methods, due to the rapid decay of current and the finite amount of time required to sample the current. We report both metrics here but consider $\rho_{+,\Omega}$ to be a superior indicator of the limiting current fraction. This current fraction is sometimes reported as the ‘transference number’ in some literature but is reported here as the current fraction as this definition helps to distinguish it from the transference number, which has a strict definition relevant to electrochemistry.

Table S2: The two selectivity metrics determined from analysis of the symmetric Li/Li cell.

ΔV Cell [mV]	$\boldsymbol{\rho_{+,0}}$	$\boldsymbol{\rho_{+,\Omega}}$
20	0.56_9	0.53_8

Table S3: Some relevant information about the cell used in this experiment including the electrolyte area and thickness, the initial current, the initial current density (J_0), and the initial area specific interfacial resistance.

Area [mm^2]	**Thickness [mm]**	**I_0 [μA]**	**J_0 [μA/mm^2]**	**R_{int}/Area [kΩ/mm^2]**
6.28_3	0.49_2	8.33	1.33	0.20_7

2.3 Analysis of EIS and Polarization data obtained on Li/Li symmetric cells containing the EthIm-TFSI ZIL r=0.1 Electrolyte

In the EIS data for the EthIm-TFSI ZIL r=0.1, it was found that a slightly altered equivalent circuit gave better and more consistent fitting. This alternative equivalent circuit is given in Figure S6. No significant interfacial resistance is detected in the EIS spectrum. This may be a result of the superior electrode-electrolyte contact present in the small molecule electrolyte, since this material can be cast as a liquid and was allowed to crystallize in contact with the lithium electrode or a consequence of the superior stability of the ZIL to the PZIL in the presence of lithium.

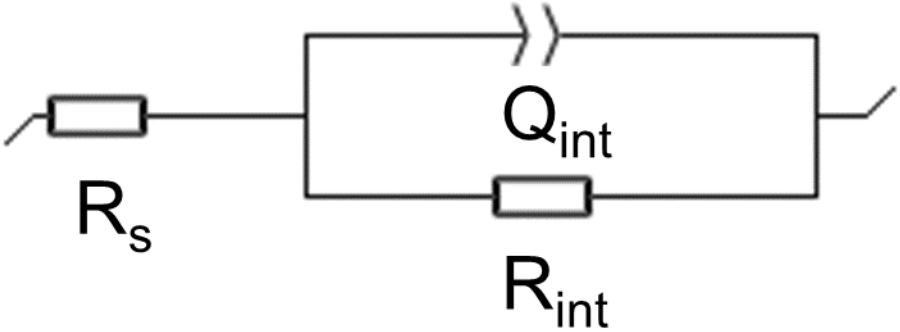

Figure S6: The Equivalent circuit model used to fit the EIS data in the Bruce-Vincent cell.

Table S4: Best-fit values for the equivalent circuit (Figure S6) used to generate fits in Figure S7.

	$\mathbf{R_s}$ $[\mathbf{p\Omega}]$	$\mathbf{Q_{bulk}}$ $[\mathbf{nF \cdot s^{a_{bulk}-1}}]$	$\mathbf{R_{bulk}}$ $[\mathbf{k\Omega}]$	$\mathbf{a_{bulk}}$ $[-]$
Before Polarization	6.905	0.637	3.453	0.804
After Polarization	3.263	0.630	3.939	0.804

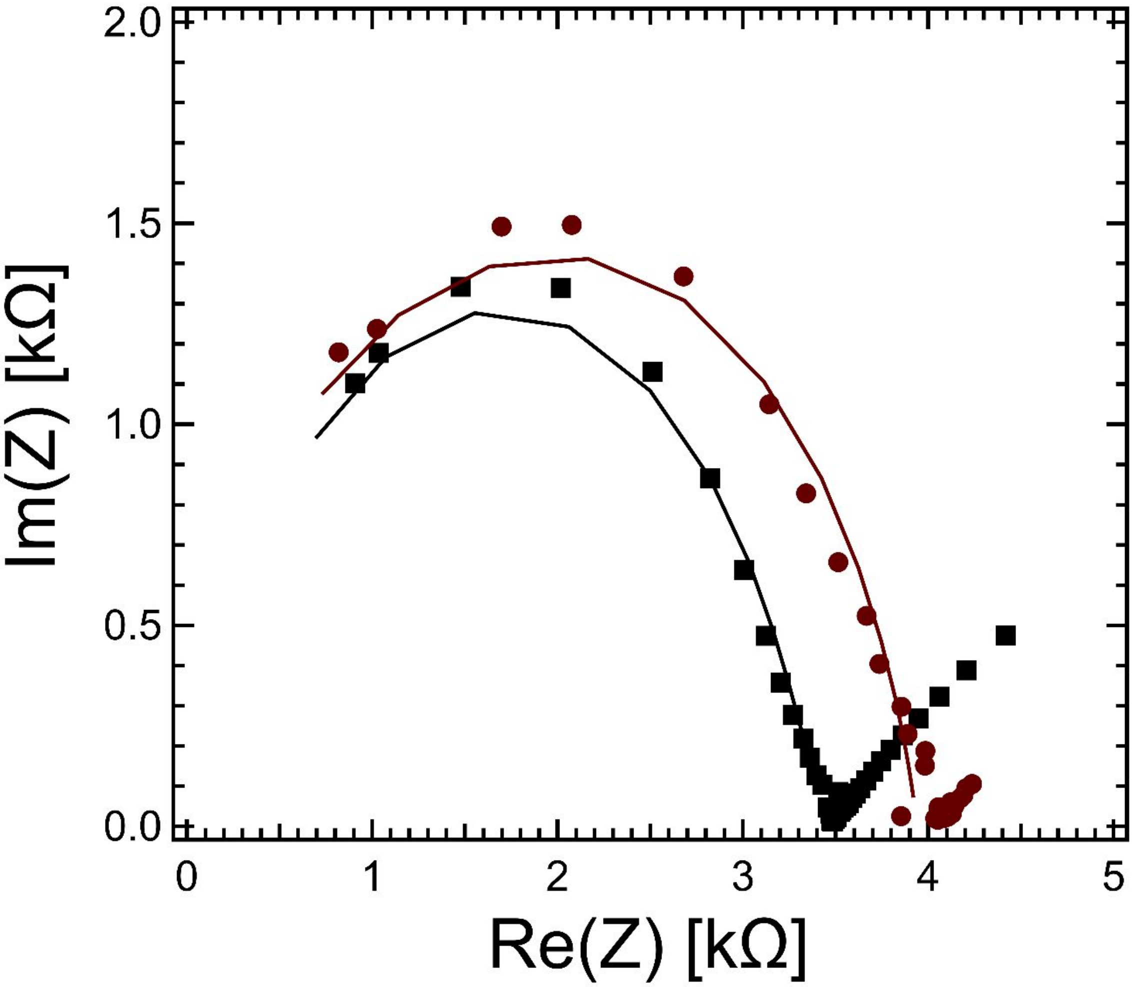

Figure S7: The EIS spectrum of the polymers before (red circle) and after (black square) polarization of the cell. The markers indicate the measured points, and the solid lines indicate the fits to the equivalent circuit using the model depicted in Figure S6 and using parameters outlined in Table S4.

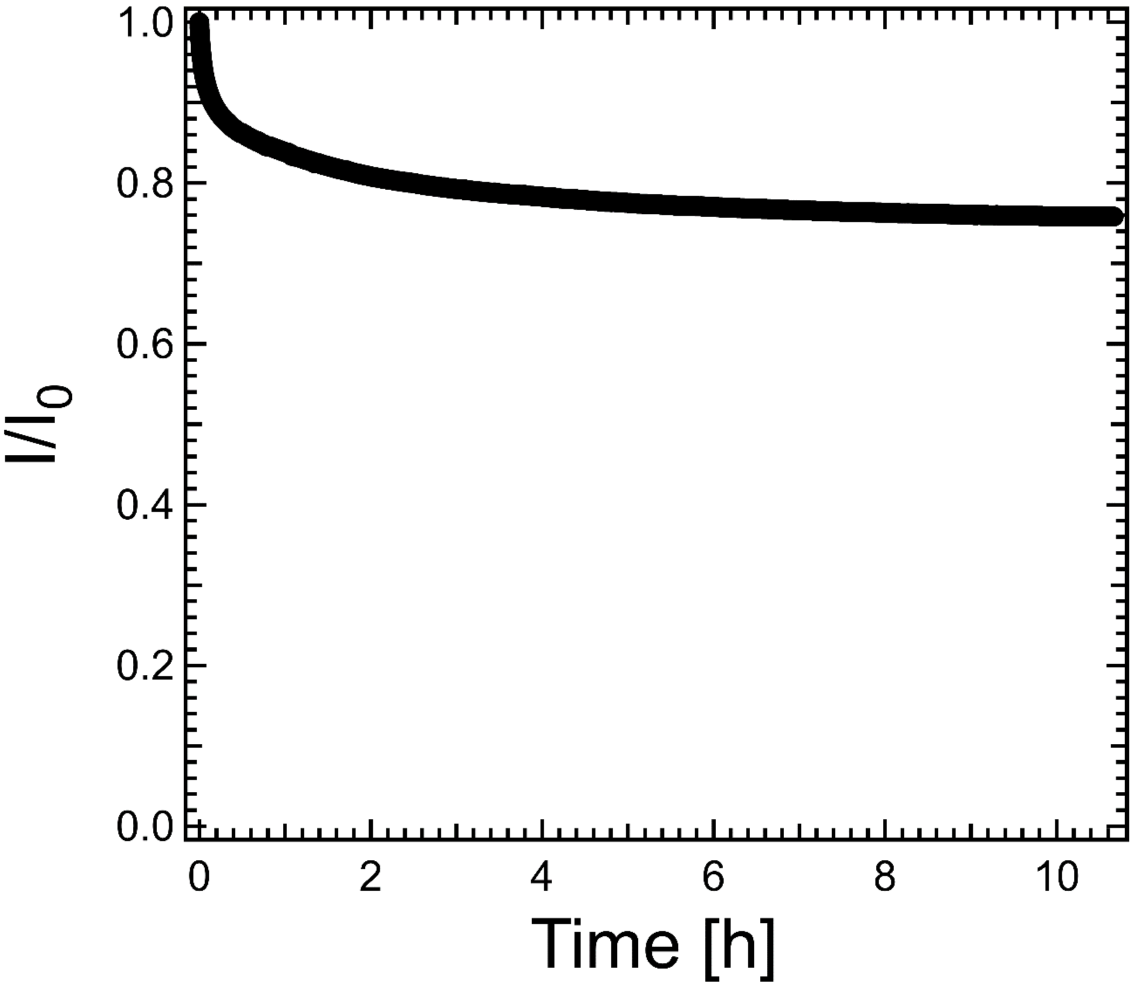

Figure S8: Normalized current versus time graph of the cell undergoing polarization. In this case, the initial current I_0 (5.53 μAmperes) observed experimentally, and the calculated value of I_Ω (5.79 μAmperes), differ somewhat due to the delay between sampling the current and applying the polarization.

The analysis from section S2.2 was again applied to determine the values of the limiting current using the two metrics described. Notably, interfacial resistance plays a significantly reduced role in this system.

Table S5: The two selectivity metrics determined from analysis of the symmetric Li/Li cell.

ΔV Cell [mV]	$\rho_{+,0}$	$\rho_{+,\Omega}$
20	0.76	0.73

Table S6: Some relevant information about the cell used in this experiment including the electrolyte area and thickness, the initial current, and the initial current density (J_0).

Area [mm^2]	**Thickness [mm]**	**I_0 [μA]**	**J_0 [μA/mm^2]**
50.27	0.8	5.53	0.110

2.4 Analysis of EIS and Polarization data obtained on Li/Li symmetric cells containing the Am-TFS-C6F5 ZIL r=0.9 Electrolyte

Analysis of the symmetric cell for the Am-TFS-C6F5 electrolyte follows the same procedure as outlined above for the other systems.

Table S7: Values of Equivalent Circuit Fitting Parameters Before and After Polarization

	$\mathbf{Q_{int}}$ $[\mathbf{\mu F \cdot s^{a_{int}-1}}]$	$\mathbf{R_{int}}$ $[\mathbf{k\Omega}]$	$\mathbf{a_{int}}$ $[-]$	$\mathbf{Q_{bulk}}$ $[\mathbf{nF \cdot s^{a_{bulk}-1}}]$	$\mathbf{R_{bulk}}$ $[\mathbf{k\Omega}]$	$\mathbf{a_{bulk}}$ $[-]$
Before Polarization	0.20_{07}	6.4_{45}	5.9_{16}	1.0_{7}	5.5_{57}	0.79_{27}
After Polarization	0.34_{70}	7.9_{40}	0.55_{82}	1.3_{04}	5.7_{78}	0.79_{19}

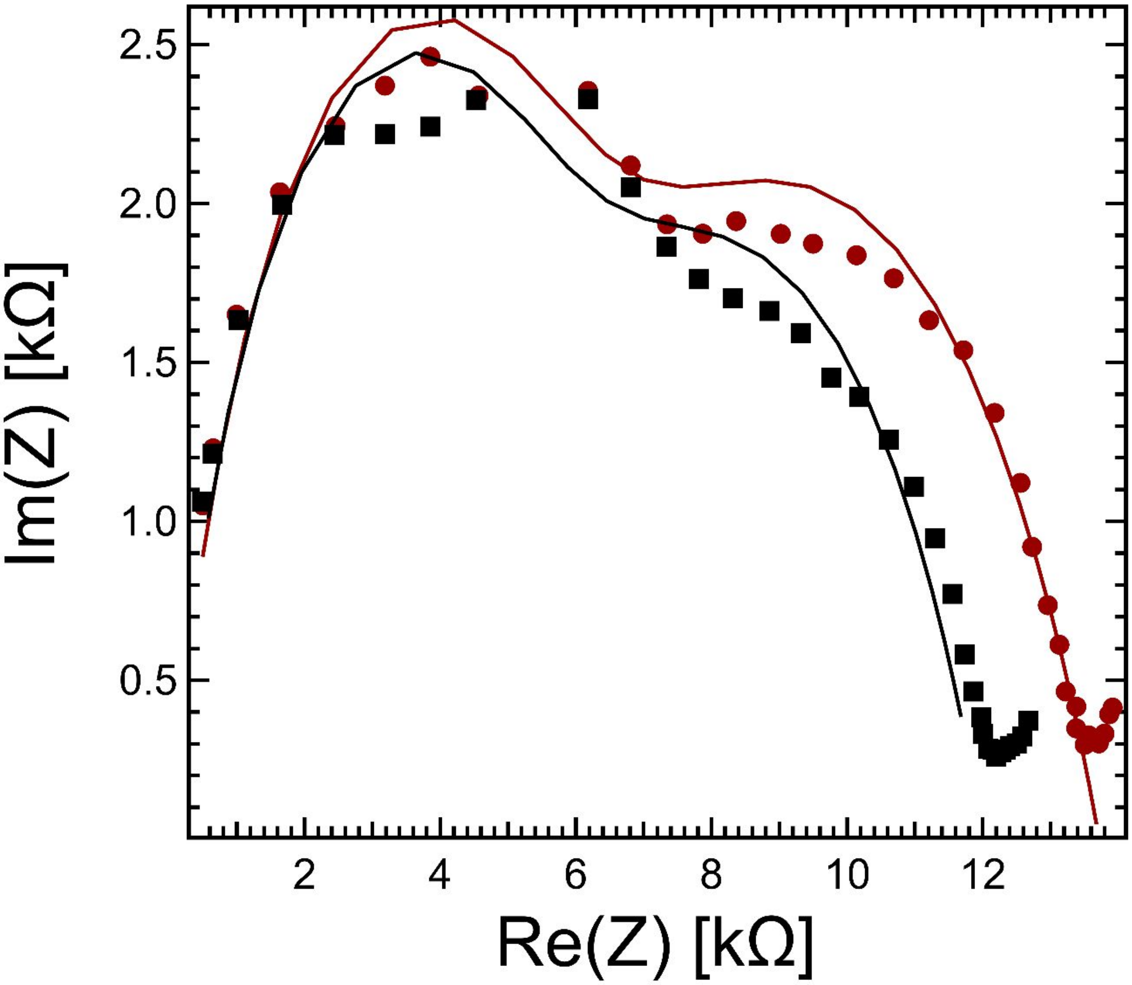

Figure S9: The EIS spectrum of the polymers before (red circle) and after (black square) polarization of the cell. The markers indicate the measured points, and the solid lines indicate the fits to the equivalent circuit using the model depicted in S3 and the parameters in Table S7.

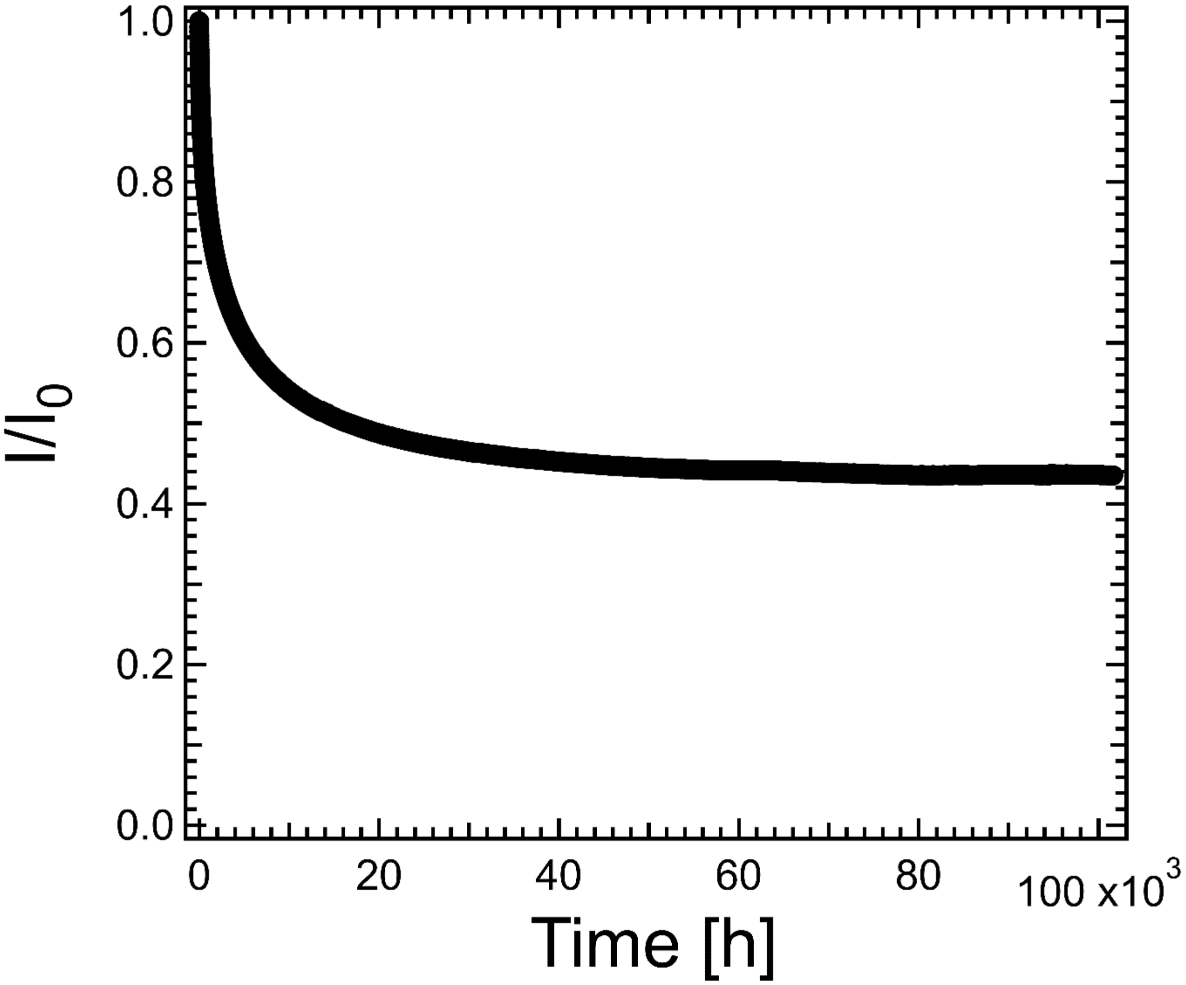

Figure S10: Normalized current versus time graph of the cell undergoing polarization. In this case, the initial current I_0 (2.30 μAmperes) observed experimentally, and the calculated value of I_Ω (1.66 μAmperes) differ somewhat.

Table S8: The two selectivity metrics determined from analysis of the symmetric Li/Li cell.

ΔV Cell [mV]	$\rho_{+,0}$	$\rho_{+,\Omega}$
20	0.19	0.47

Table S9: Some relevant information about the cell used in this experiment including the electrolyte area and thickness, the initial current, the initial current density (J_0), and the initial area specific interfacial resistance.

Area [mm^2]	**Thickness [mm]**	**I_0 [μA]**	**J_0 [μA/mm^2]**	**R_{int}/Area [kΩ/mm^2]**
28.3	0.39	2.30	0.081_{27}	0.19_{63}

3 Solid-State NMR

3.1 Discussion of Solid-State NMR for Im-TFSI PZIL

The 1D ^{7}Li NMR data collected on the salt-containing PZILs indicate that lithium exists in multiple environments. A fit of the ^{7}Li spectrum (Figure S11A) reveals two Gaussian line-shapes centered at similar overlapping chemical shifts (1.08 and 1.32 (calibrated using a 1.0 M LiCl (aq) sample)) but with different linewidths. The narrow component accounts for 24% of the total integrated intensity, while the broad component accounts for 76%. The similar chemical shifts of two signals suggest that all the Li^+ ions, which are solely introduced by the Li^+/bTFSI$^-$ salt, exist in rather similar bonding environments. The NMR linewidths are inversely proportional to the molecular relaxation timescales (T2) of the Li^+ and suggest that ~24% of Li ions exist in an environment with faster dynamics, and ~76% of the Li ions in environments associated with slower dynamics. In contrast, the 1D ^{19}F NMR spectrum (Figure S11D) reveals two fluorine populations with clear differences in chemical shift and yet a less dramatic difference in line-width as compared to the ^{7}Li data. These ^{19}F environments are attributed to polymer-bound TFSI$^{–}$ and free fluorine coming from the bTFSI$^-$ counterion.

^{7}Li $T_{1\rho}$ relaxometry measurements were performed and corroborate the observation from 1D NMR that Li^+ exists in two dynamic environments. $T_{1\rho}$ measurements use a spin-lock radiofrequency pulse (here, of 10 kHz), which serves to probe ion dynamics on the order of milliseconds and are more selective to typical diffusion timescales of interest than standard T_1 or T_2 relaxation measurements. Figure S11.1C shows a fit of the $T_{1\rho}$ signal decay curve when a single dynamic mode is considered and when two dynamic environments are considered. For all temperatures measured, the data require two dynamic timescales to obtain an accurate fit, consistent with the two lithium environments identified with 1D NMR. Additionally, the relative populations of the two lithium environments are in good agreement with the two fractions identified from 1D NMR, with ~74% of the lithium showing a $T_{1\rho}$ of 240 microseconds and ~ 26% displaying a relaxation at 1.2 milliseconds.

The multiple dynamic environments detected for lithium were further verified by pulsed-field gradient (PFG) NMR methods, which revealed multiple ^{7}Li diffusion coefficients and only a single ^{19}F diffusion environment. PFG-NMR measurements were carried out using a standard variable magnetic field gradient Bruker diffusion pulse sequence (diffste) which includes a stimulated echo, serving to protect the signal from shorter relaxation times observed in these solid-like samples. The PFG measurements used herein probe diffusion across lengthscales roughly in the 0.1-1 μm characteristic diffusion lengthscale, making this a much larger lengthscale probe of the ion dynamics than the relaxometery or lineshape analyses. A reasonable fit of the curve representing the evolution of the ^{7}Li signal intensity versus magnetic field gradient strength at a fixed diffusion time (Figure S11B) requires two exponential decay functions describing two distinct lithium dynamic environments. The relative populations of the two environments are consistent with relaxometry and 1D NMR results with ~26% of the lithium exhibiting a diffusion coefficient of $7.59 \cdot 10^{-12}$ $m^2s^{–1}$ and ~74% exhibiting a lower diffusivity of $9.16 \cdot 10^{-13}$ $m^2s^{–1}$ (Figure S11F). The ^{19}F diffusion curve can be reasonably fit with one exponential decay function corresponding to a self-diffusion coefficient of $1.28 * 10^{-12}$ $m^2s^{–1}$, as shown in Figure S11E, even though 1D experiments indicated two chemical environments for fluorine. The presence of a single observable diffusion ^{19}F timescale is most likely due to the low mobility of polymer-bound Im-TFSI$^-$ units leading to very slow decay of the corresponding ^{19}F NMR signal that is essentially filtered out in the PFG-NMR measurements.

Overall, analyses of the scattering data and microscopic diffusion information altogether suggest that the fast mode of Li$^+$ conduction occurs within crystalline domains of the electrolyte. The Walden plot analysis qualitatively demonstrates the presence of a solid-like mechanism of conduction in this polymer material. While solid-like conduction can occur in amorphous super-T_g polymers when the dynamics of strand rearrangement is much slower than ion rearrangement, it is more likely to occur in a 'frozen structure,' such as the crystalline domains detected by WAXS. Consequently, these results suggest that Li$^+$ diffusion occurs via two mechanisms: a fast ballistic or hopping-type transport mechanism within the crystalline domains of the polymer, and a slower, liquid-like diffusion process within amorphous regions. The presence of two lithium environments validated by 1D NMR line-shape analysis, $T_1\rho$ relaxometry, and PFG-NMR measurements is consistent with this hypothesis. In contrast, TFSI$^-$ ions probed by ^{19}F NMR exhibit significant motion in only the amorphous regions of the electrolyte. This observation is consistent with the Andersen-Stuart[5] and related barrier-type models[6-8], which predict that larger ions will experience a larger barrier for diffusion in dense domains such as crystallites. Here, dense crystalline regions lead to selective Li transport due to the large size difference between the TFSI$^-$ and Li$^+$ ions, which could account for the complete filtering-out of PFG-NMR signal decay due to ^{19}F nuclei in the crystalline regions of the electrolyte.

This understanding leads to a consistent picture of ionic motion through the bulk PZIL material, with crystalline domains acting as highly Li$^+$-selective transport regions and dual-ion conducting amorphous domains exhibiting slightly preferential diffusion of TFSI$^-$ ions as illustrated by Figure 6. The single diffusion coefficient measured by ^{19}F PFG-NMR is attributed to the amorphous-phase conduction of the TFSI$^-$ ion, the lack of a second coefficient being consistent with the notion that TFSI$^-$ ion is highly hindered within the crystallites (and polymer-bound Im-TFSI$^-$ units are immobile). The 'slow mode' diffusion coefficient of lithium is also likely to correspond to the amorphous-phase conductivity of this species, as this phase is likely to have a reduced strand density resulting in a 'Coulombically-dominated' energy barrier for diffusion, which favors TFSI$^-$ motion over Li$^+$. Consequently, the 'fast mode' of lithium conduction corresponds to a ballistic/hopping transport within crystalline regions of the material.

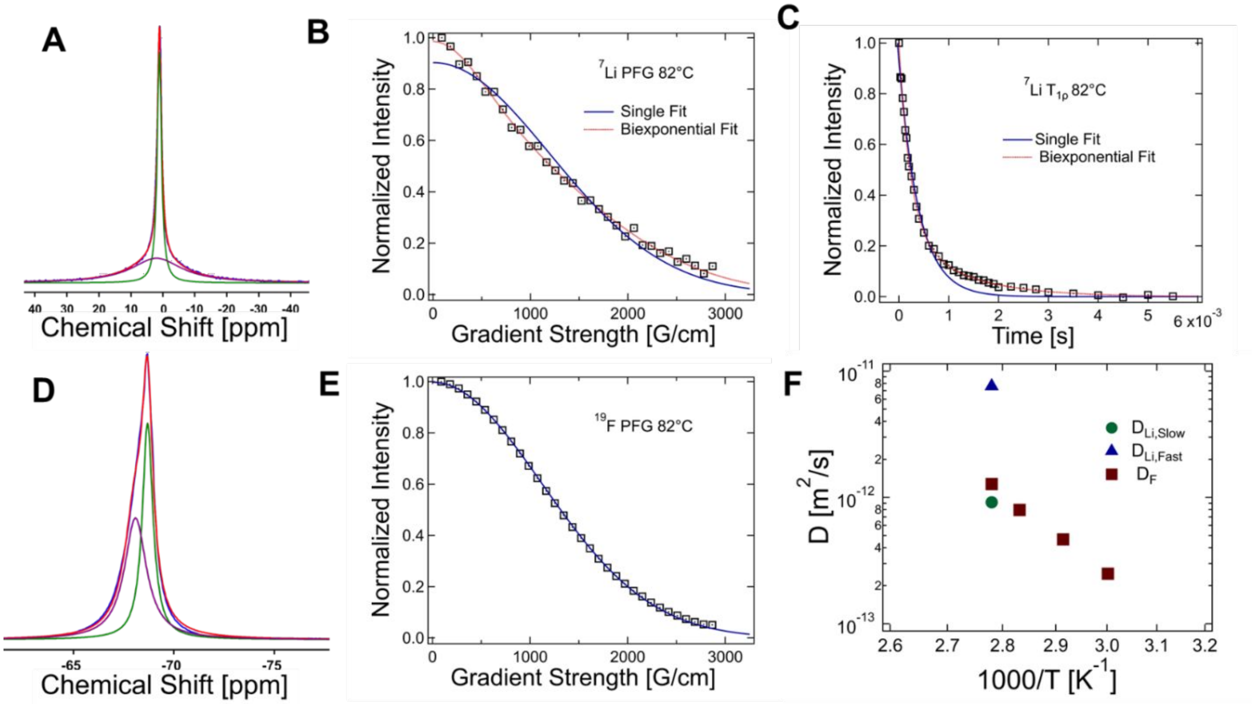

Figure S11: A) Line shape analysis of the 1D ^{7}Li NMR spectrum. The blue curve is the experimental data, the pink curve is the broad Gaussian component and the green curve is the narrow gaussian component with the red curve representing the sum of these components. The fit using two Gaussian lines centered at very similar resonant frequencies demonstrates that lithium exists in two environments that are chemically similar but display different dynamics. B) The Li^7 pulsed field gradient profile with fits based on one and two components. The diffusion profile requires two signal components to fit the decay, with relative weights in line with the populations of the two lithium environments determined from the fit of the 1D ^{7}Li NMR line shape in A). C) The ^{7}Li T_{1p} relaxometry curve with one- and two-component fits reveals once again that two lithium populations are necessary to fit the decay curve. The size of these populations again agrees with the 1D and PFG-NMR results. D) The ^{19}F line shape analysis with the same curve labels as in panel A. In this case, the widths of the curves are similar, but the chemical shifts differ more significantly, suggesting the presence of two chemical environments, tentatively assigned to polymer-bound and free fluorine-containing species. E) The ^{19}F diffusion curve can be fit assuming a single diffusion mode, suggesting that all mobile fluorine exists in a similar diffusing environment. F) The diffusion coefficients obtained from PFG-NMR experiments as a function of inverse temperature demonstrate that the amorphous conductivities of the lithium and fluorine are similar, suggesting that the high conductivity of these electrolytes is derived from the motion of lithium through the crystalline domains of the material.

3.2 A Note on Spectrum Fitting

Several expressions are used to fit the diffusion and relaxometry data herein. These expressions contain an exponential decay function such as Equation S6. Typically, when a single exponential decay function does not provide an adequate fit the poor fitting can be remedied by either modifying the exponential by adding a ‘stretch’ to the exponential as in equation or by adding a second exponential decay function which represents another distinct dynamic population.

It is frequently the case that both approaches may improve the data fit, however the interpretation of these two fitting modes differs significantly. While a stretched exponential indicates broadening of dynamics within a single population, multiple exponentials indicate multiple populations with different dynamics. To resolve this issue of ambiguous fitting, fitting was performed via the following procedure: 1) Begin from a stretched exponential fit, if the fit collapses to the single-exponent limit use the single-exponential fit, otherwise maintain this stretched exponential fit 2) if the stretched-exponential fit fails, add a second exponential mode. In this manner, a second exponential mode is only added if the stretched exponential fit fails to describe the data, this approach will only accept the hypothesis of multiple dynamic populations when dynamic broadening fails to account for the dynamics.

When fitting the lineshapes of NMR spectra both Gaussian and Lorentzian fits were considered. Regardless of this choice, two components are required to fit the lineshape of both the 1D lithium and fluorine spectra

7.3 Fitting of 1D Lithium NMR Spectrum

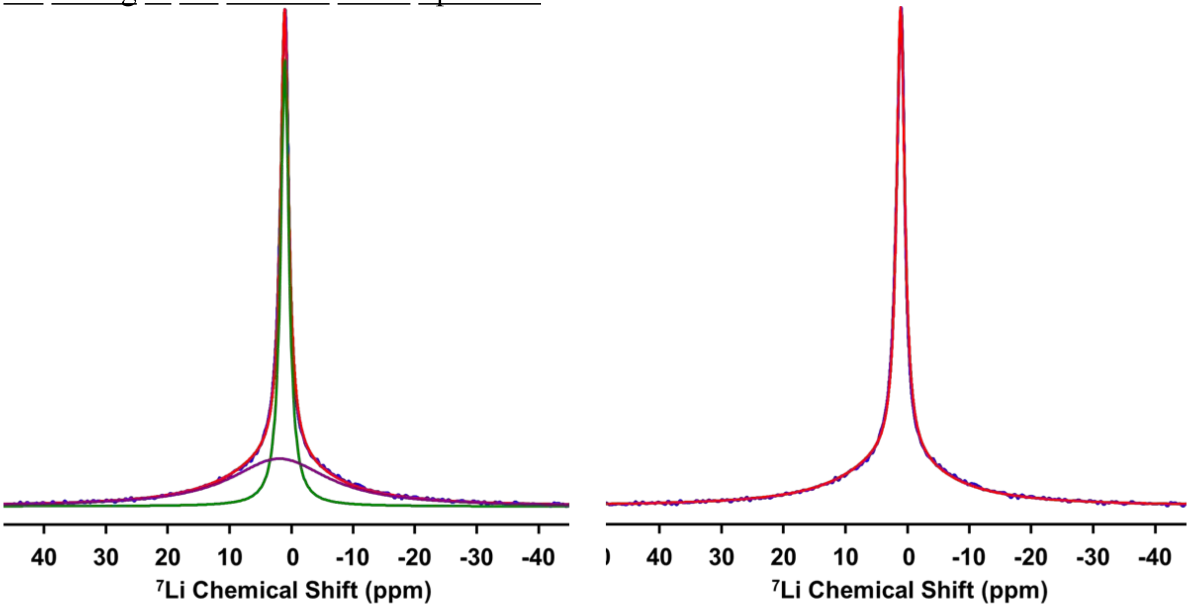

Figure S12: The image from Figure S11 is expanded so that the agreement between experimental lineshape and the fitted shape. The green and purple components represent individual Gaussian components to the fit and the red shape is the sum of these components. The blue curve is the experimental lineshape. The right panel reproduces the figure on the left, but the individual components have been removed from this panel for clarity.

3.3 ^{19}F T_1 Measurements of Im-TFSI PZIL

T_1 decay curves presented in this section have been fit using a single exponential decay function of the form:

$$I = I_0 \exp\left(-\frac{t}{T_1}\right) \qquad \text{Eqn. S6}$$

where I is the observed NMR signal intensity, T_1 is the NMR spin-lattice relaxation time, t is the experimental signal decay time, and I_0 is the initial signal intensity at time t=0.

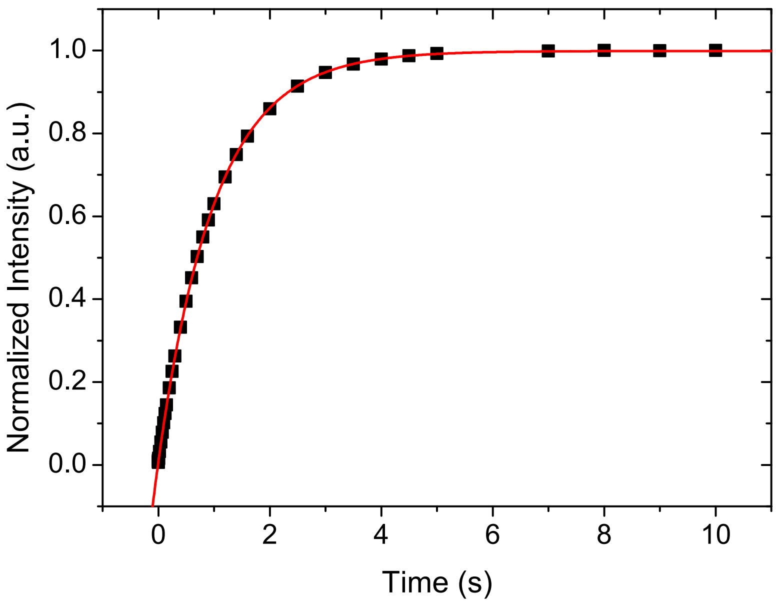

Figure S13: The normalized intensity versus time curve for a ^{19}F T_1 experiment on the Im-TFSI PZIL with r=0.9 at a temperature of 355 K. The black squares correspond to measured data and the red curve is a single exponential fit (Equation S6).

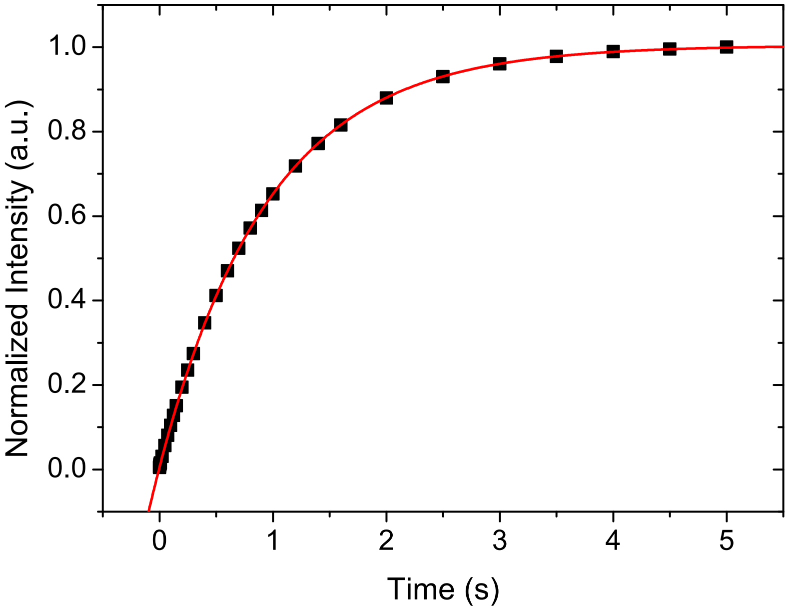

Figure S14: The normalized intensity versus time curve for a ^{19}F T_1 experiment on the Im-TFSI PZIL with r=0.9 at a temperature of 346 K. The black squares correspond to measured data and the red curve is a single exponential fit (Equation S6).

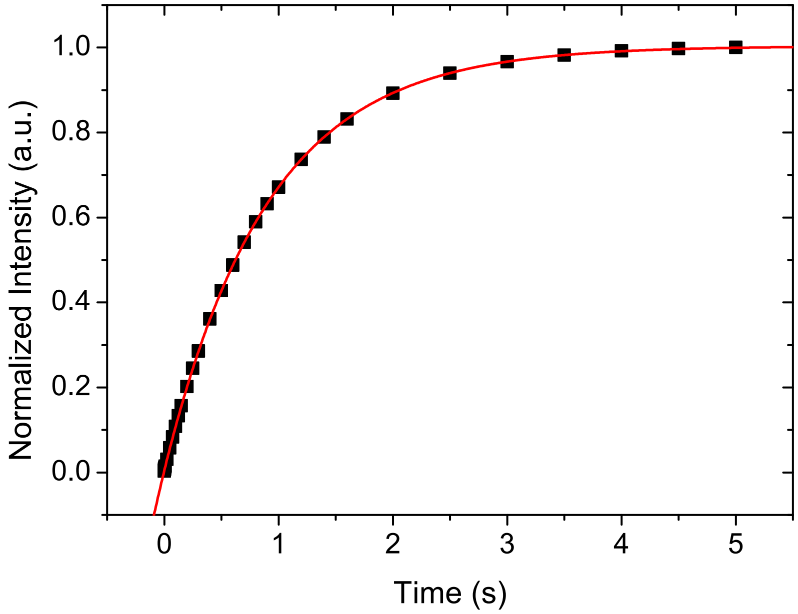

Figure S15: The normalized intensity versus time curve for a ^{19}F T_1 experiment on the Im-TFSI PZIL with r=0.9 at a temperature of 337 K. The black squares correspond to measured data and the red curve is a single exponential fit (Equation S6).

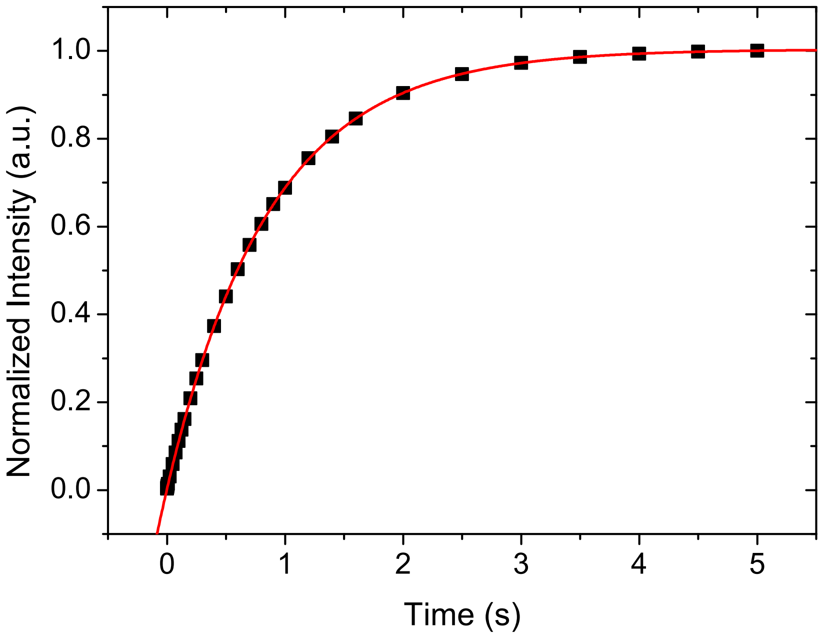

Figure S16: The normalized intensity versus time curve for a ^{19}F T_1 experiment on the Im-TFSI PZIL with r=0.9 at a temperature of 328 K. The black squares correspond to measured data and the red curve is a single exponential fit (Equation S6).

Table S10: Parameters obtained from single-component fits of the ^{19}F T1 relaxation decay curves in Fig S13-16.

Temperature [C]	I_0	A	T_1 [ms]
355	1.013 ± 0.001	0.992 ± 0.001	1013 ± 1
346	1.0043 ± 0.0003	0.9948 ± 0.0002	958.3 ± 0.8
337	1.0035 ± 0.0002	0.9961 ± 0.0001	907.5 ± 0.6
328	1.0036 ± 0.0003	0.9974 ± 0.0002	865.5 ± 0.7

7.4 ^{7}Li $T_{1\rho}$ Experiments of Im-TFSI PZIL

$T_{1\rho}$ decay curves presented in this section have been fit using the single exponential decay function presented previously (Equation S6), and using a double exponential decay function of the form:

$$I = I_1 \exp\left(-\frac{t}{T_{1\rho,1}}\right) + I_2 \exp\left(-\frac{t}{T_{1\rho,2}}\right) \qquad \text{Eqn. S7}$$

where I is the observed NMR signal intensity, $T_{1\rho,i}$ is the NMR spin-lattice relaxation time in the rotating frame of reference for component i, t is the experimental signal decay time, and I_i is the initial signal intensity at time t=0 for component i.

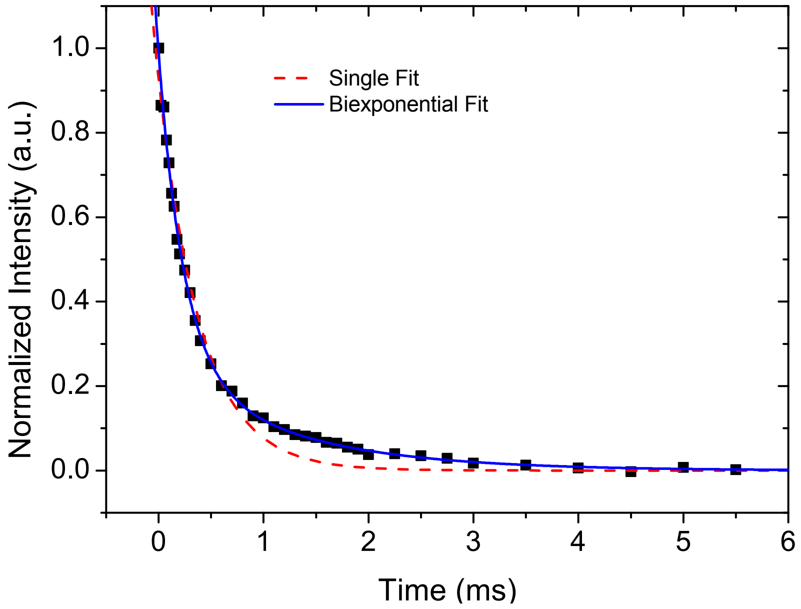

Figure S17: The normalized intensity versus time curve for a ^{7}Li $T_{1\rho}$ experiment on the Im-TFSI PZIL with r=0.9 at a temperature of 355 K. The black squares correspond to measured data and the red and blue curves are fits using single (Equation S6) and biexponential functions (Equation S7), respectively.

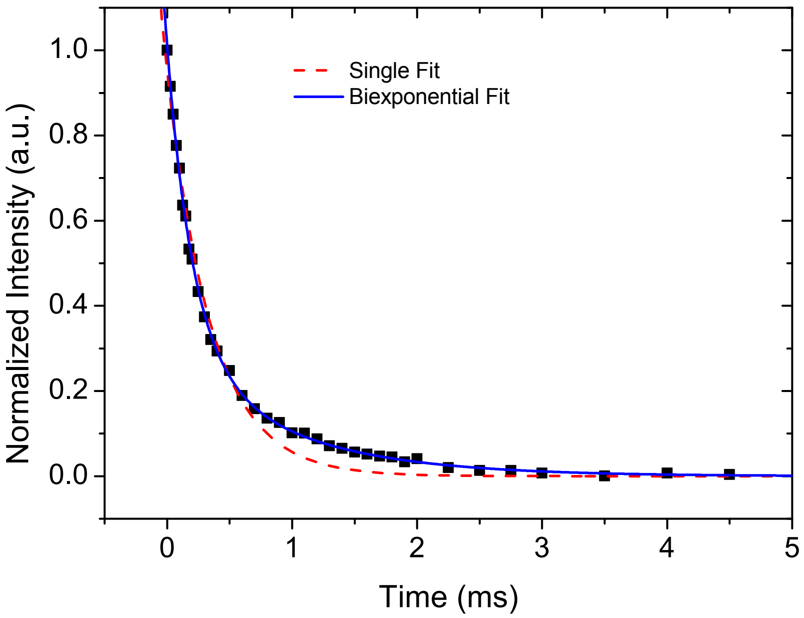

Figure S18: The normalized intensity versus time curve for a ^{7}Li $T_{1\rho}$ experiment on the Im-TFSI PZIL with r=0.9 at a temperature of 346 K. The black squares correspond to measured data and the red and blue curves are fits using single (Equation S6) and biexponential functions (Equation S7), respectively.

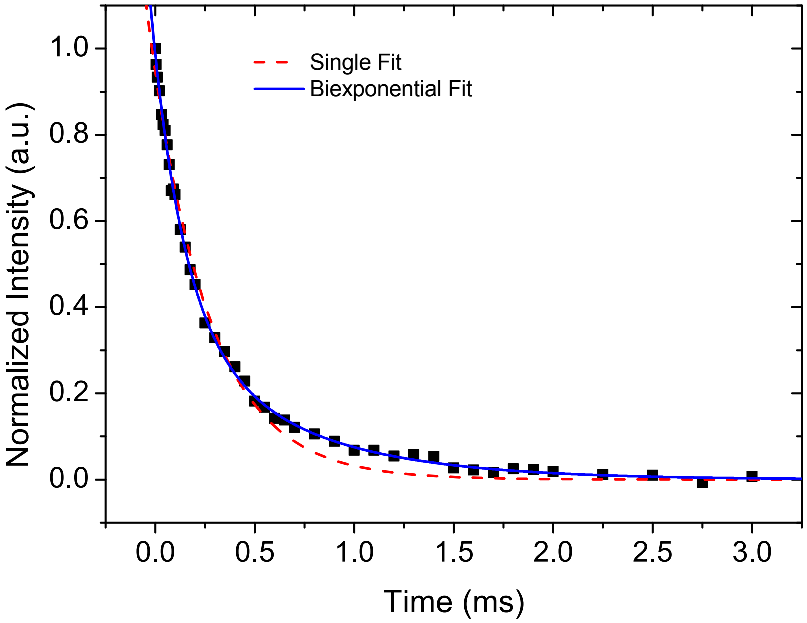

Figure S19: The normalized intensity versus time curve for a ^{7}Li $T_{1\rho}$ experiment on the Im-TFSI PZIL with r=0.9 at a Temperature of 337 K. The black squares correspond to measured data and the red and blue curves are fits using single (Equation S6) and biexponential functions (Equation S7), respectively.

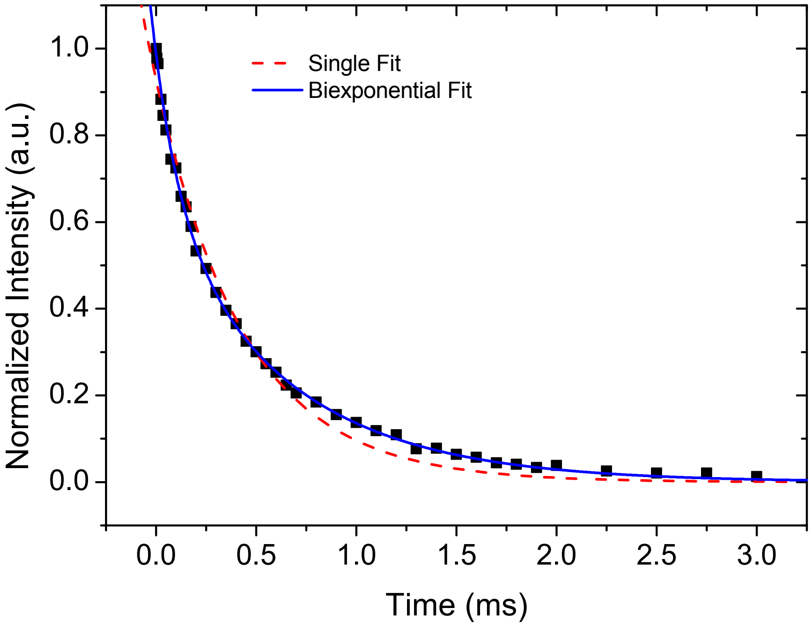

Figure S20: The normalized intensity versus time curve for a ^{7}Li $T_{1\rho}$ experiment on the Im-TFSI PZIL with r=0.9 at a temperature of 328 K. The black squares correspond to measured data and the red and blue curves are fits using single (Equation S6) and biexponential functions (Equation S7), respectively.

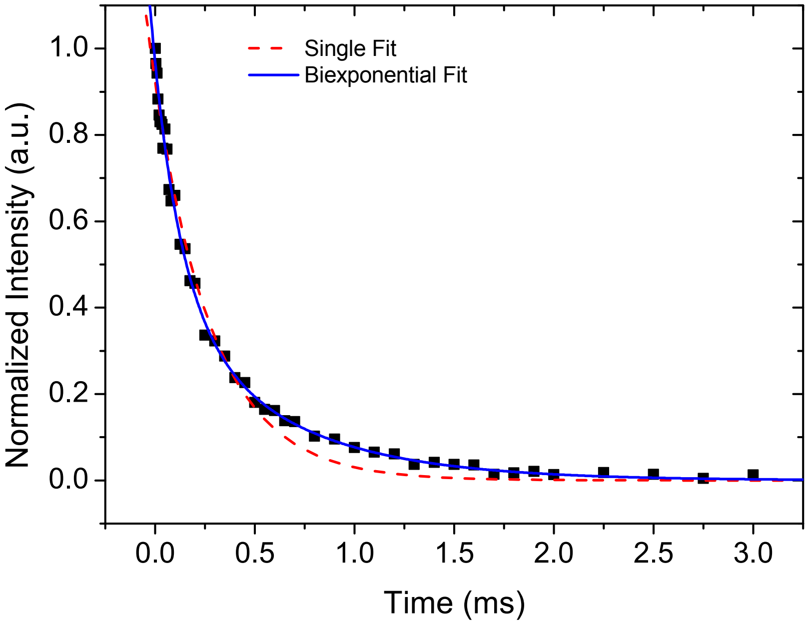

Figure S21: The normalized intensity versus time curve for a ^{7}Li $T_{1\rho}$ experiment on the Im-TFSI PZIL with r=0.9 at a temperature of 320 K. The black squares correspond to measured data and the red and blue curves are fits using single (Equation S6) and biexponential functions (Equation S7), respectively.

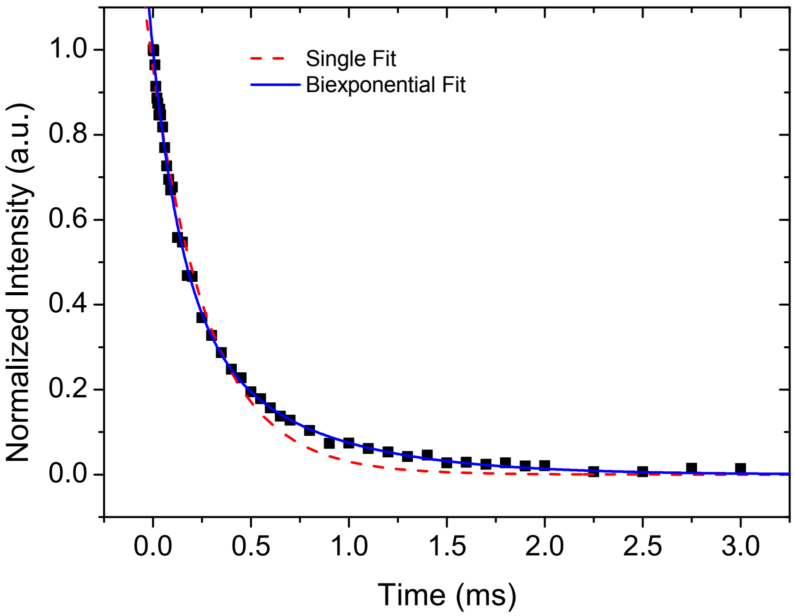

Figure S22: The normalized intensity versus time curve for a ^{7}Li $T_{1\rho}$ experiment on the Im-TFSI PZIL with r=0.9 at a temperature of 311 K. The black squares correspond to measured data and the red and blue curves are fits using single (Equation S6) and biexponential functions (Equation S7), respectively.

All $T_{1\rho}$ decay curves presented in Fig S17-S22 are not accurately described using a single exponential function (Equation S6) and instead require a biexponential function shown in Equation S7. ^{7}Li $T_{1\rho}$ parameters obtained from these biexponential fits are presented in Table S11. As mentioned previously, there is good agreement between the intensities of the two ^{7}Li $T_{1\rho}$ components and the two lithium diffusion modes at a temperature of 355 K. Additionally, the first mode (with shorter $T_{1\rho}$) decreases in prominence compared to the second mode as temperature is reduced. This observation is consistent with a pattern where motion through the superionic mode becomes the dominant mode of lithium transport in the electrolyte as temperature is reduced.

Table S11: Parameters obtained from two-component fits of the ^{7}Li $T_{1\rho}$ decay curves presented in Figures S17-22.

Temperature [K]	**I_1**	**$T_{1\rho,1}$ [µs]**	**I_2**	**$T_{1\rho,2}$ [ms]**
355	0.736 ± 0.03	238 ± 17	0.252 ± 0.03	1190 ± 50
346	0.715 ± 0.03	205 ± 9	0.297 ± 0.03	916 ± 20
337	0.633 ± 0.03	132 ± 10	0.353 ± 0.03	649 ± 26
328	0.622 ± 0.05	163 ± 11	0.364 ± 0.05	626 ± 55
320	0.5922 ± 0.05	151 ± 12	0.405 ± 0.06	588 ± 55
311	0.556 ± 0.07	142 ± 17	0.413 ± 0.07	593 ± 77

3.5 ^{7}Li Pulsed Field Gradient Diffusion Profile of Im-TFSI PZIL

Single and double exponential functions used to fit the PFG NMR decay curves presented in sections 3.4 and 3.5.

$$I = I_0\exp\left(-D\gamma^2G^2\delta^2\left(\Delta - \frac{\delta}{3}\right)\right) \qquad \text{Eqn. S8}$$

$$I = I_1\exp\left(-D_1\gamma^2G^2\delta^2\left(\Delta - \frac{\delta}{3}\right)\right) + I_2\exp\left(-D_2\gamma^2G^2\delta^2\left(\Delta - \frac{\delta}{3}\right)\right) \qquad \text{Eqn. S9}$$

Where D is the self-diffusion constant, γ is the gyromagnetic ratio, G is the gradient field strength, δ is the gradient pulse duration, and Δ is the time between gradient pulses.

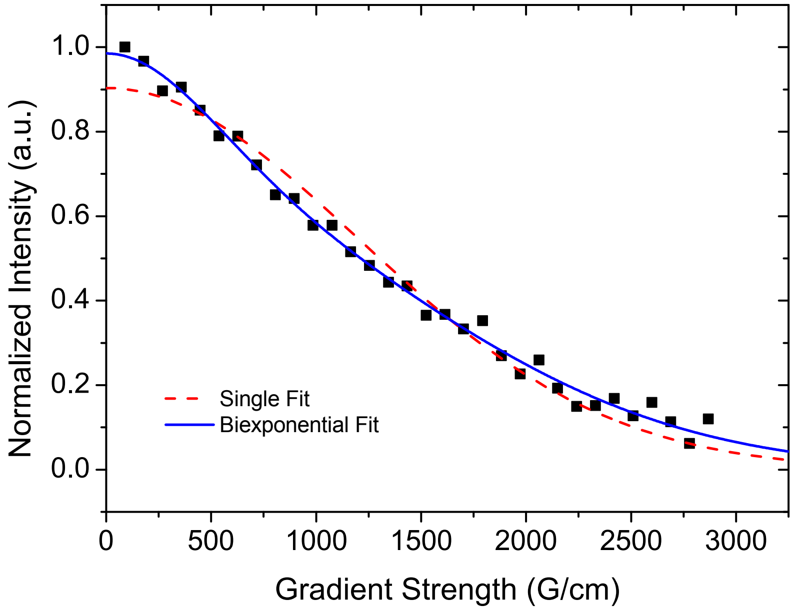

Figure S23: The normalized intensity versus gradient strength curve obtained from a ^{7}Li PFG NMR measurement on the Im-TFSI PZIL with r=0.9 at a temperature of 355 K. The black squares correspond to measured data and the red and blue curves are fits using single (Equation S8) and biexponential functions (Equation S8), respectively.

Pulsed field gradient NMR measurements at a temperature of 355 K indicate two transport modes for lithium. This claim is supported by the significant improvement in the fit of the PFG NMR signal decay curve when using two diffusing components as compared to when using a single component. This analysis is further supported by the remarkable consistency between the relative intensities of the two lithium diffusion modes determined across NMR relaxometry, PFG NMR, and NMR lineshape analysis.

Table S12: Parameters obtained from a biexponential fit of the ^{7}Li PFG NMR data in Fig. S23.

Temperature	D1 [m2/s]	D2 [m2/s]	I1	I2	Δ [ms]	δ [ms]
355 K	$(9.16 \pm 0.5)\cdot 10^{-13}$	$(7.59 \pm 0.5)\cdot 10^{-12}$	0.738	0.262	100	1.65

3.6 ^{19}F Pulsed Field Gradient Diffusion Profiles of Im-TFSI PZIL

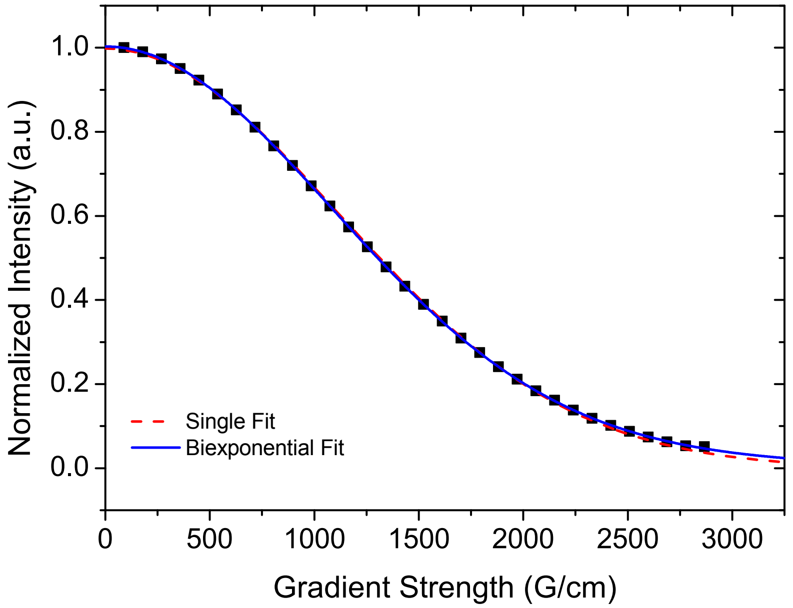

Figure S24: The normalized intensity versus gradient strength obtained from a ^{19}F PFG NMR measurement on the Im-TFSI PZIL with r=0.9 at a temperature of 355 K. The black squares correspond to measured data and the red and blue curves are fits using single (Equation S8) and biexponential functions (Equation S9), respectively. The single exponential fit appears to fully capture the behavior of the curve, suggesting that a single diffusive mode is sufficient to describe the motion of fluorine in this polymer.

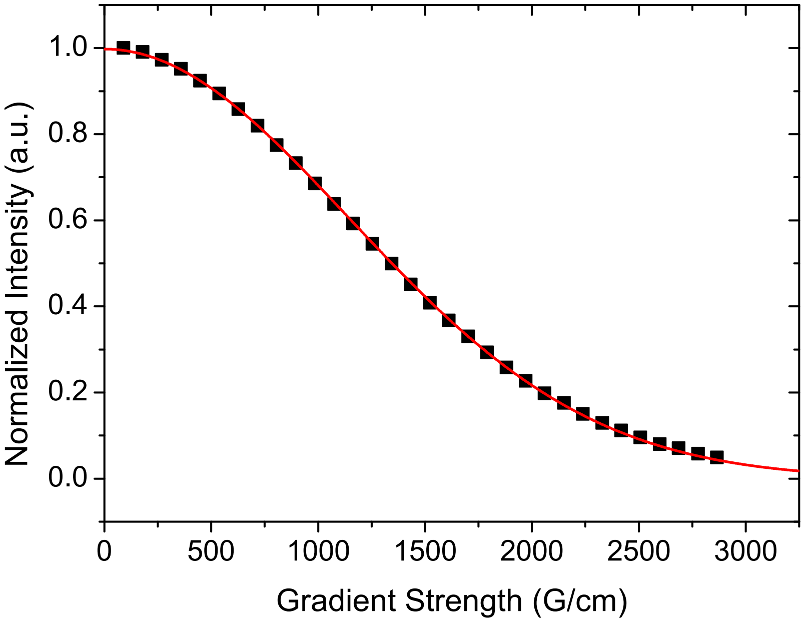

Figure S25: The normalized intensity versus gradient strength obtained from a ^{19}F PFG NMR measurement on the Im-TFSI PZIL with r=0.9 at a temperature of 346 K. The black squares correspond to measured data and the red curve is fit using a single exponential function (Equation S8) . The single exponential fit appears to fully capture the behavior of the curve, suggesting that a single diffusive mode is sufficient to describe the motion of fluorine in this polymer.

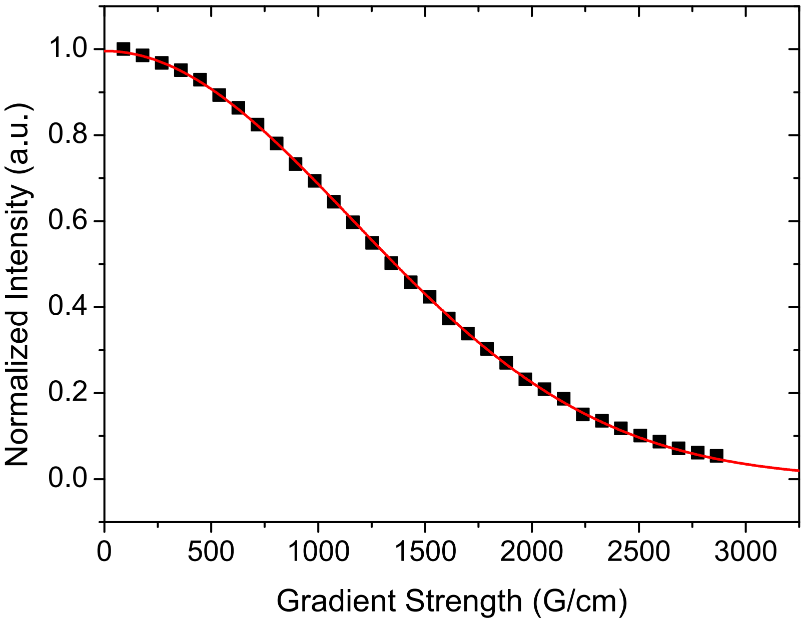

Figure S26: The normalized intensity versus gradient strength obtained from a ^{19}F PFG NMR measurement on the Im-TFSI PZIL with r=0.9 at a temperature of 337 K. The black squares correspond to measured data and the red curve is fit using a single exponential function (Equation S8). The single exponential fit appears to fully capture the behavior of the curve, suggesting that a single diffusive mode is sufficient to describe the motion of fluorine in this polymer.

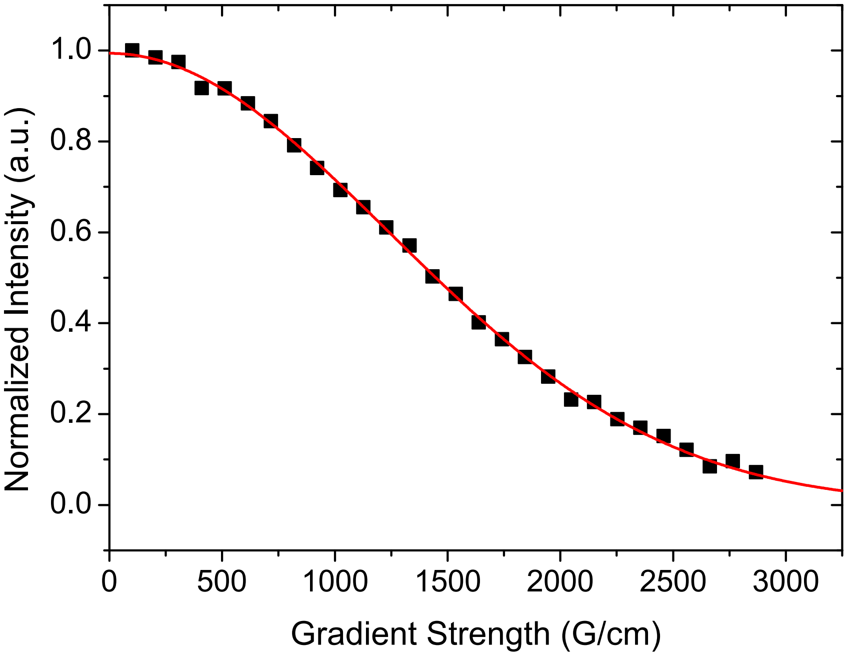

Figure S27: The normalized intensity versus gradient strength obtained from a ^{19}F PFG NMR measurement on the Im-TFSI PZIL with r=0.9 at a temperature of 328 K. The black squares correspond to measured data and the red curve is fit using a single exponential function (Equation S8). The single exponential fit appears to fully capture the behavior of the curve, suggesting that a single diffusive mode is sufficient to describe the motion of fluorine in this polymer.

Table S13: Parameters obtained from single-component fits of the ^{19}F PFG NMR data in S24-S27.

Temperature	**D [m2/s]**	**I0**	**Δ [ms]**	**δ [ms]**
355	$(1.275 \pm 0.006)\cdot10^{-12}$	0.998	50	1.0
346	$(7.96 \pm 0.006)\cdot10^{-13}$	0.998	53	1.2
337	$(4.65 \pm 0.02)\cdot10^{-13}$	0.996	65	1.4
328	$(2.49 \pm 0.02)\cdot10^{-13}$	0.994	77	1.65

3.7 Lithium-Ion transport number of Im-TFSI PZIL

The lithium-ion transport number of the Im-TFSI PZIL is defined as the product of the concentration of lithium and the average diffusivity of lithium divided by the product of concentration (c) and diffusivity (D) for all other mobile ionic species as shown in Equation S9.

$$t_{Li} = \frac{\langle D_{Li} \rangle c_{Li}}{\sum \langle D_i \rangle c_i} \qquad \text{Eqn. S9}$$

Where the index 'i' corresponds to any ionic species in the system and the brackets correspond to a number-average. In this case, we have demonstrated that the total ionic conductivity of the system is reduced by orders of magnitude in the absence of the $Li^+/TFSI^-$ salt – suggesting that this dopant provides the majority of the mobile ionic species in the system. Consequently, it is approximated that the only relevant mobile ionic species are the Li^+ and $TFSI^-$. Importantly, the neutral pair of Li/TFSI may contribute to the observed diffusion of Lithium and TFSI. The motion of neutral pairs is a component of the distinction between t_+ and ρ_+ (further discussed in the manuscript). An additional simplification of Equation S9 is made by substituting the fact that $c_{Li}=c_{TFSI}$, which is universal for 1:1 salts. Equation S10 gives a relation which is used to practically evaluate the lithium transport number of this system. Where the average diffusion coefficient is calculated from the biexponential fit

$$t_{Li} = \frac{D_{Li,1} I_{Li,1} + D_{Li,2} I_{Li,2}}{D_{Li,1} I_{Li,1} + D_{Li,2} I_{Li,2} + D_{TFSI}} \qquad \text{Eqn. S10}$$

Equation S11 demonstrates the evaluation of this expression to obtain a lithium transport number.

$$t_{Li} = \frac{9.16 \cdot 10^{-13} \cdot 0.738 + 7.59 \cdot 10^{-12} \cdot 0.262}{9.16 \cdot 10^{-13} \cdot 0.738 + 7.59 \cdot 10^{-12} \cdot 0.262 + 1.275 \cdot 10^{-12}} = 0.676 \qquad \text{Eqn. S11}$$

3.8 ^{7}Li Pulsed Field Gradient Diffusion Profile of Am-TFSI PZIL

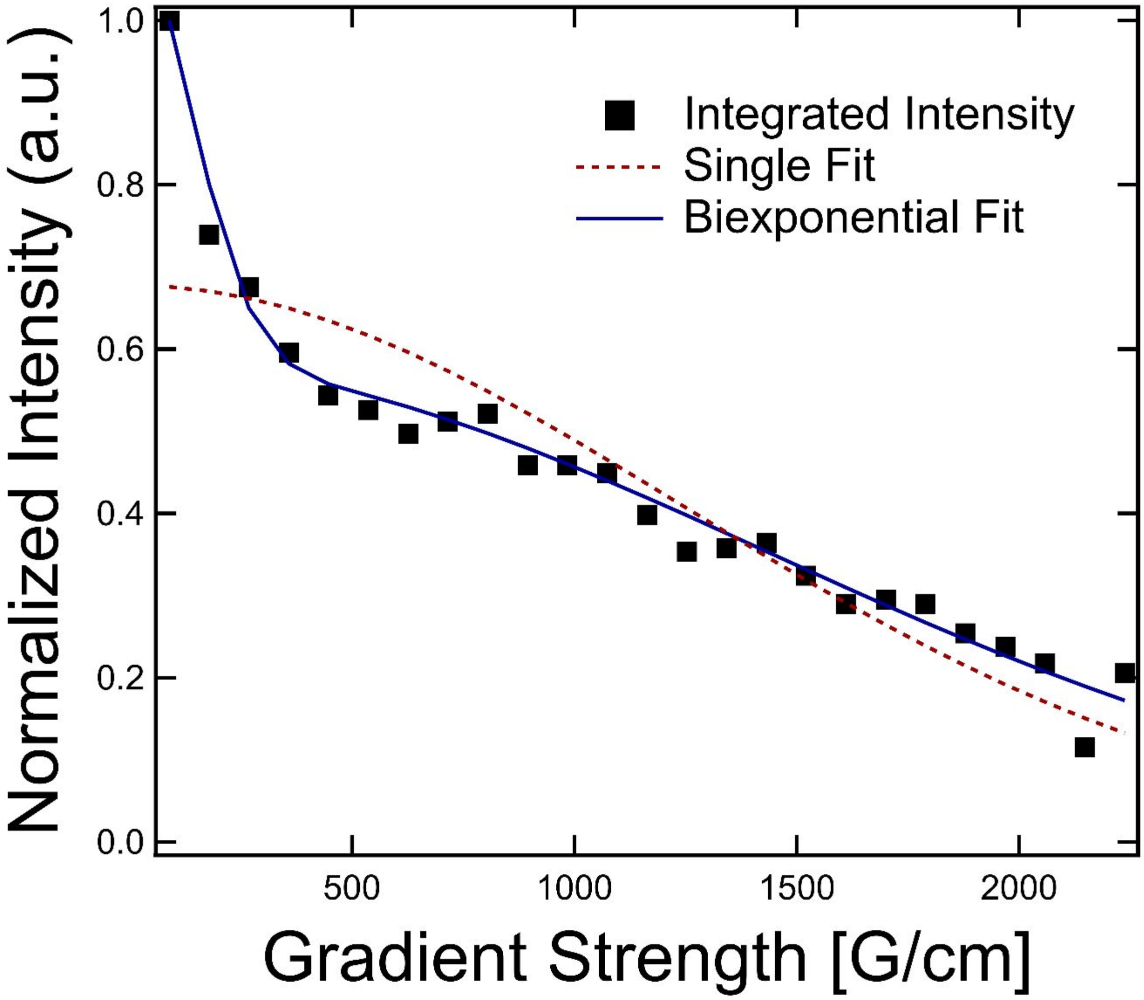

Figure S28: The normalized intensity versus gradient strength curve for a ^{7}Li PFG NMR experiment of the Im-TFSI PZIL with r=0.9 at a Temperature of 355 K. The black points correspond to measured data and the red and blue curves are fits to single (Equation S8) and biexponential functions (Equation S9), respectively.

The ^{7}Li PFG NMR decay curve clearly contains two components with widely different diffusion behaviors, as evidenced by the poor fit obtained using a single exponential function. Diffusion parameters for the two lithium environments obtained from biexponential fits of the data using Equation S9 are shown in Table S14.

Table S14: Parameters obtained from a biexponential fit of the ^{7}Li PFG NMR data in Figure S28.

Temperature	D1 [m2/s]	D2 [m2/s]	I1	I2	Δ [ms]	δ[ms]
355 K	$(7.84 \pm 0.07) \cdot 10^{-13}$	$(8.48 \pm 0.2) \cdot 10^{-11}$	0.530	0.471	42	1

3.9 ^{19}F Pulsed Field Gradient Diffusion Profile of Am-TFSI PZIL

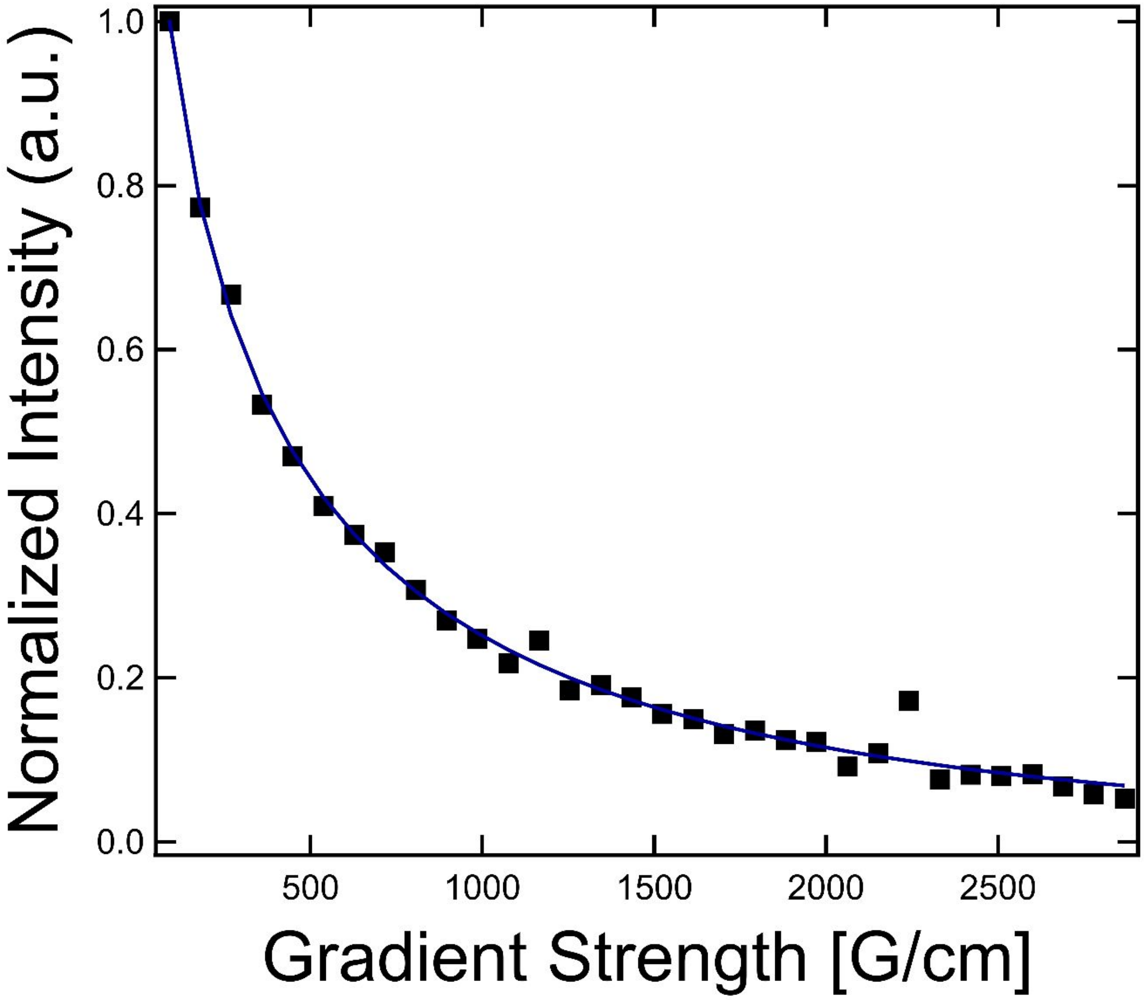

Figure S29: The normalized intensity versus gradient strength curve for a ^{19}F PFG NMR experiment of the Im-TFSI PZIL with r=0.9 at a Temperature of 355 K. The black points correspond to measured data and the blue curve is a fit to single stretched exponential function (Equation S12).

The best fit of the ^{19}F PFG NMR decay curve in Fig S29 was obtained using a single-component, stretched exponential (β is the stretch factor):

$$I = I_0 \exp\left(-\left[D\gamma^2 G^2 \delta^2 \left(\Delta - \frac{\delta}{3}\right)\right]^{\beta}\right) \qquad \text{Eqn. S12}$$

Table S15: Parameters obtained from a single-component, stretched exponential fit of the ^{19}F PFG NMR data in Fig S29.

Temperature	D [m^2/s]	β	I_0	Δ [ms]	δ[ms]
355 K	$(1.96 \pm 0.7)\cdot 10^{-11}$	0.248 ± 0.02	1.95 ± 0.2	42	1

3.10 Lithium-Ion transport number of Am-TFSI PZIL

Evaluation of the transport number uses the procedure described in S7.6 as shown in Equation S13.

$$t_{Li} = \frac{7.84 \cdot 10^{-13} \cdot 0.53 + 8.48 \cdot 10^{-11} \cdot 0.471}{7.84 \cdot 10^{-13} \cdot 0.53 + 8.48 \cdot 10^{-11} \cdot 0.471 + 1.96 \cdot 10^{-11}} = 0.673 \qquad \text{Eqn. S13}$$

Notably, the diffusivities from NMR are nearly an order of magnitude faster for the Am-TFSI PZIL than the Im-TFSI PZIL, however these is not a correspondent increase in the ionic conductivity of the Am-TFSI PZIL as measured by EIS. Accordingly, the NMR measurements in this case greatly overpredict the ionic conductivity, presumably due to significant ion pairing in the Am-TFSI PZIL.

4 Additional Structural Analysis of the Zwitterion

The structure of the ZIL was further characterized. In Figure S30, optical microscopy images of the ZIL (A) and the cast ZIL electrolyte (S30B) are shown. These microscopy images demonstrate the crystalline nature of the compound. Figure S30C shows a snapshot of the crystallographic structure of the ZIL in the absence of lithium salt. This ZIL assembles into a $Pna2_1$ spacegroup and has a site of crystallographic disorder. Complete crystallographic information for this compound can be accessed using at the Cambridge Crystallography Data Centre (Deposition Number 2122282).

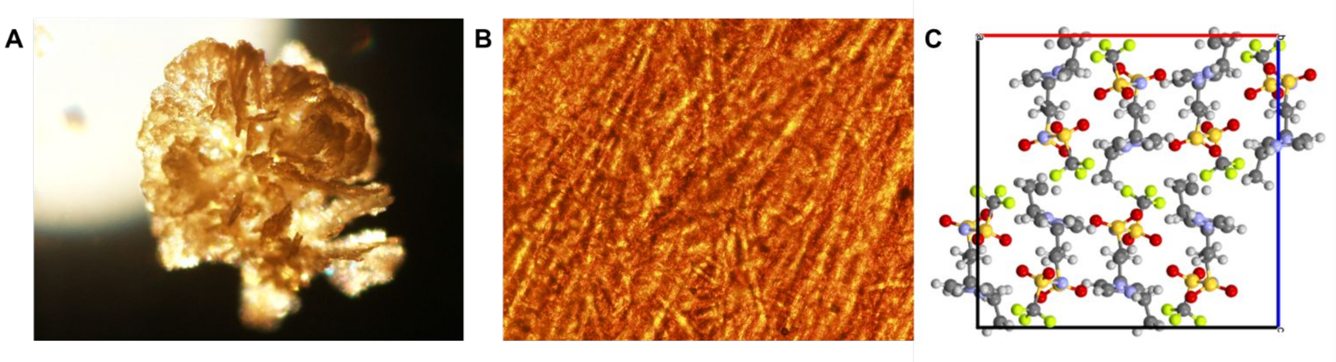

Figure S30: A) An optical microscopy image of the ZIL molecule after 3x recrystallization. B) An optical microscopy image of the ZIL electrolyte which was solvent cast from acetontirile along with ~5% by mass LiTFSI salt (estimated to range between 4-6%). C) The structure of the ZIL crystal (without salt) viewed along the ‘b’ direction. The unit cell is belongs to a $Pna2_1$ spacegroup and there is a site of crystallographic disorder at the terminal carbon of the ethyl pendance chain (attached to the 1-position of the imidazolium ring). The crystallographic information file for this crystal has been deposited with the Cambridge Crystallographic Data Centre.

5 Room temperature stability of Im-TFSI PZIL r=0.9 versus Lithium

A composite cathode made of the PZIL mixed with carbon additives and PTFE was charged and discharged against a lithium foil anode using a standard organic liquid electrolyte (1 M $LiPF_6$ in ethylene carbonate and dimethylcarbonate) to assess the voltage stability of the PZIL at room temperature. All testing was performed galvanostatically with a current of 2.5 mA/g. This method is preferred over cyclic voltammetry experiments, which overestimate the electrochemical stability of solid-state electrolytes[9] The presence of carbon additives (typically missing in Cyclic Voltammetry experiments) can catalyze degradation of the solid-electrolyte and is needed to accurately gauge electrochemical stability. Additionally, the fast sweep rates in CV experiments and poor electronic conductivity of solid-electrolytes limit the degradation current that can be detected. Galvanostatic cycling overcomes this limitation by cycling at a slow constant current, which provides sufficient time for the electrolyte to equilibrate and fully react at the set potential. The stability (voltage) window of the electrolyte is comprised between the potentials at which capacity starts to increase significantly (e.g., past 10 mAh g^{-1}) as measured in the (dis)charge curves. Here, the stability window lies between 3.8V and 1.16 V vs. Li for Im-TFSI PZIL. This room temperature stability window makes Im-TFSI PZIL suitable for industrially relevant lithium-ion cathode materials such as $LiFePO_4$, which operates around 3.5 V vs. Li.

We do note that there is significant capacity outside of this voltage window that may be the result of electrochemically catalyzed reactions of the electrolyte. Several possible reactions may occur including breaking of the amide bond or reactions of the RAFT end groups. We believe that additional efforts to engineer a more voltage-stable PZIL may be necessary for practical implementation of this class of electrolyte.

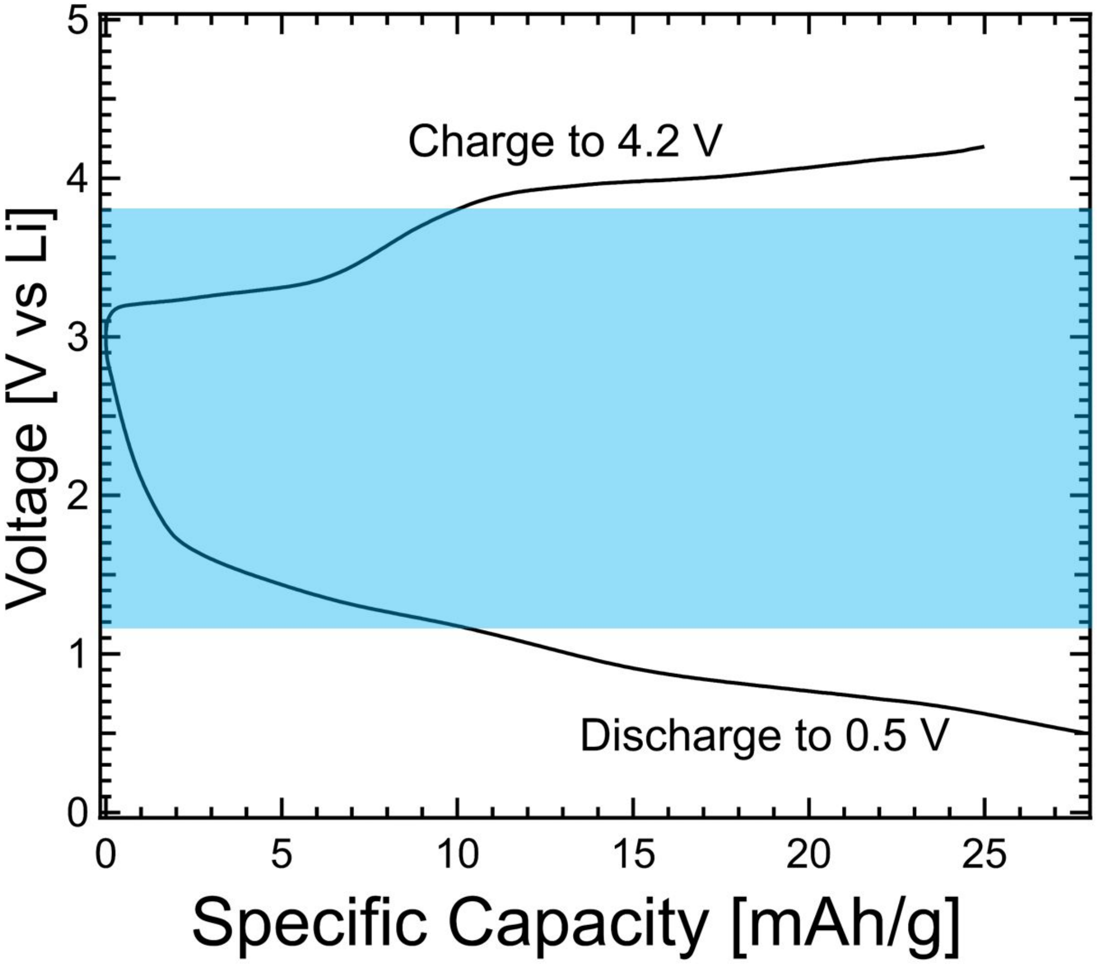

Figure S31: This figure shows the capacity Voltage against lithium versus the capacity for the cell described above. A stability window is defined with the blue square as the voltage range where the cell exhibits minimal capacity (capacity<10mAh/g).

6 Evaluating the High-Salt Limit

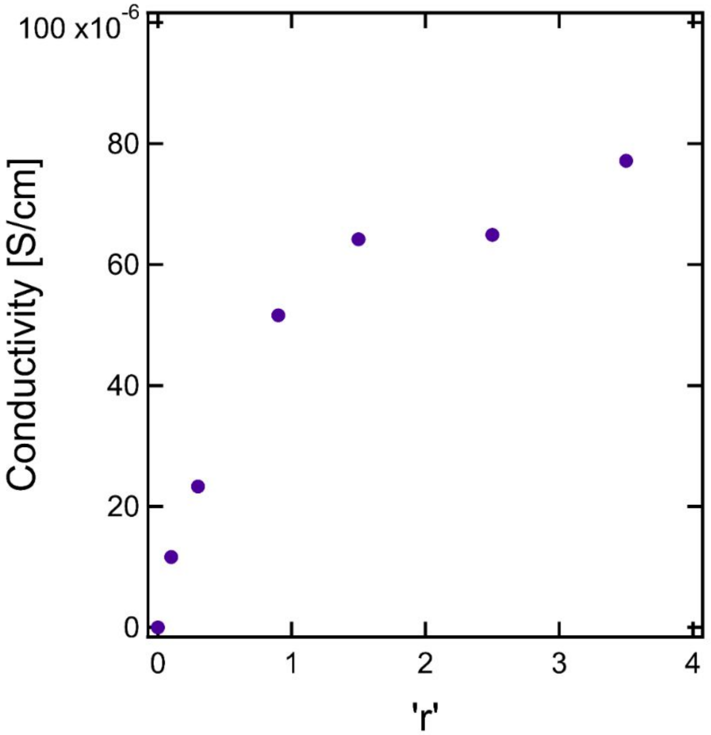

Figure S32: Higher monomer/salt ratios have been evaluated (without full characterization) to determine the optimal formulation range for these PZILs. Although the conductivity monotonically increases throughout this composition range, the lower salt formulations are the primary subject of investigation in the current report since these offered the best tradeoff of mechanical properties and ion conduction.

Table S16: This table demonstrates the precipitous drop in the calorimetric glass transition temperature as large quantities of salt are added to the electrolyte.

Salt Loading (r-ratio)	T_g [°C]
0	25
0.1	11
0.3	2
0.9	-5
1.5	-12
2.5	-35
3.5	-42

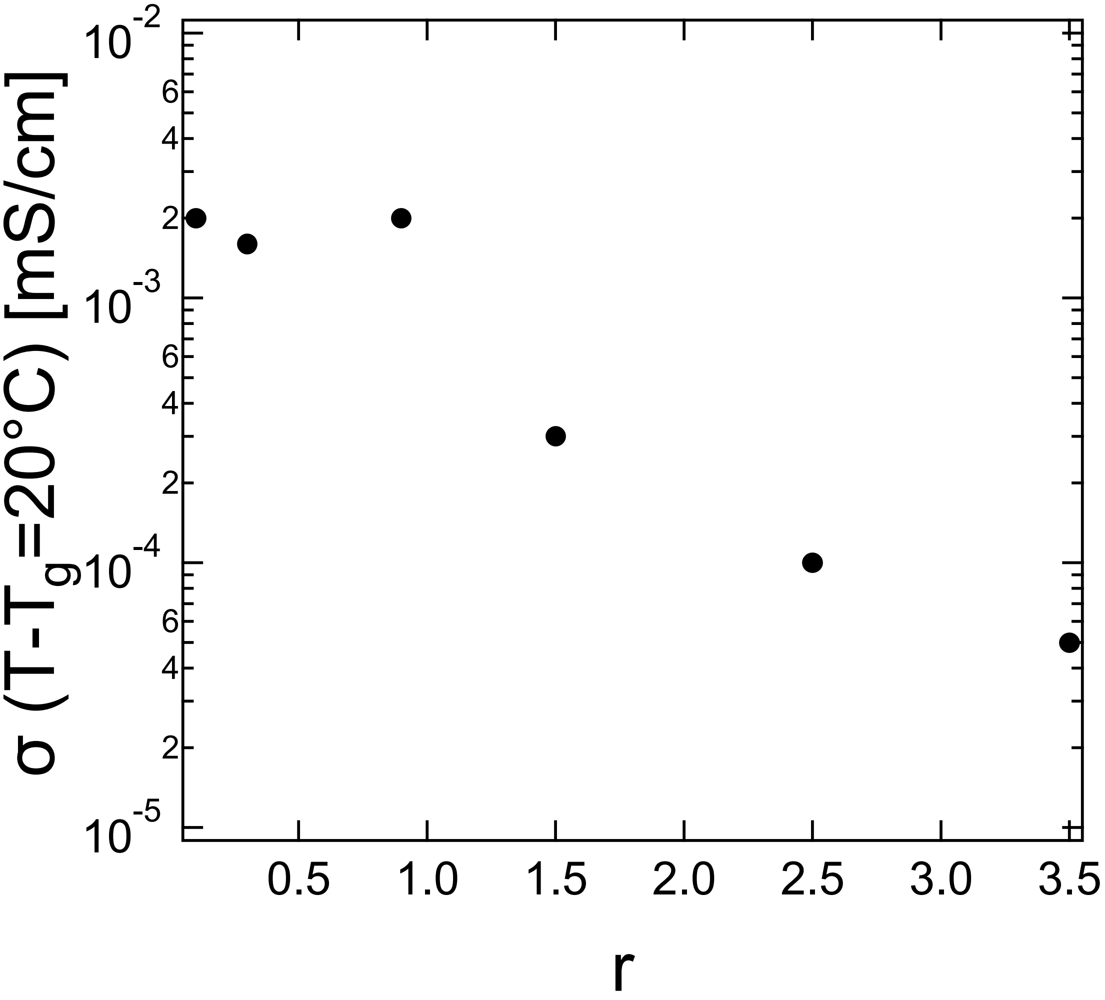

Figure S33: Ionic conductivity (normalized by glass transition temperature) plotted against the salt concertation as parameterized by r. A precipitous drop in normalized conductivity is observed at the same concentration at which Bragg peaks disappear. There is indeed a precipitous drop in conduction through this transition. This suggests that as the crystalline structure melts, a more conventional vehicular transport mechanism dominates. This difference is even more pronounced when the number of charge carriers is considered since the number-density of mobile charges is proportional to salt concentration.

7 Thermal Analysis

7.1 Thermogravimetric Analysis of Materials

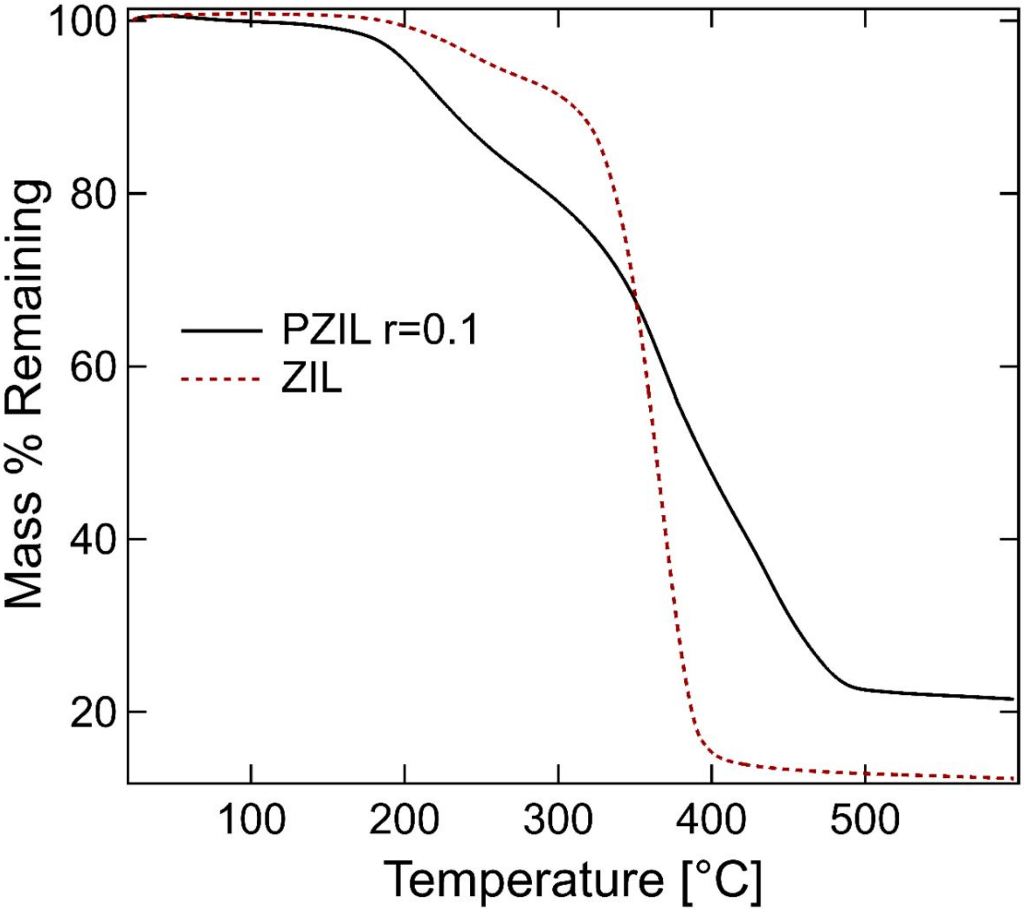

Figure S34: The decomposition profiles of the ZIL and PZILs are shown in the TGA curve with a ramp rate of 10C/minute. The onset of mass loss for the PZILs, indicated by the temperature at which 1% of mass has been lost, is found to be 180°C, so this temperature was utilized as a maximum temperature for further thermal analysis. Evidently there are two reaction stages for degradation of both the PZILs and the ZIL indicated by the presence of an initial drop in the mass % remaining at ~200°C and a second more severe drop at ~350°C.

7.2 Lithium bTFSI Melting Curve

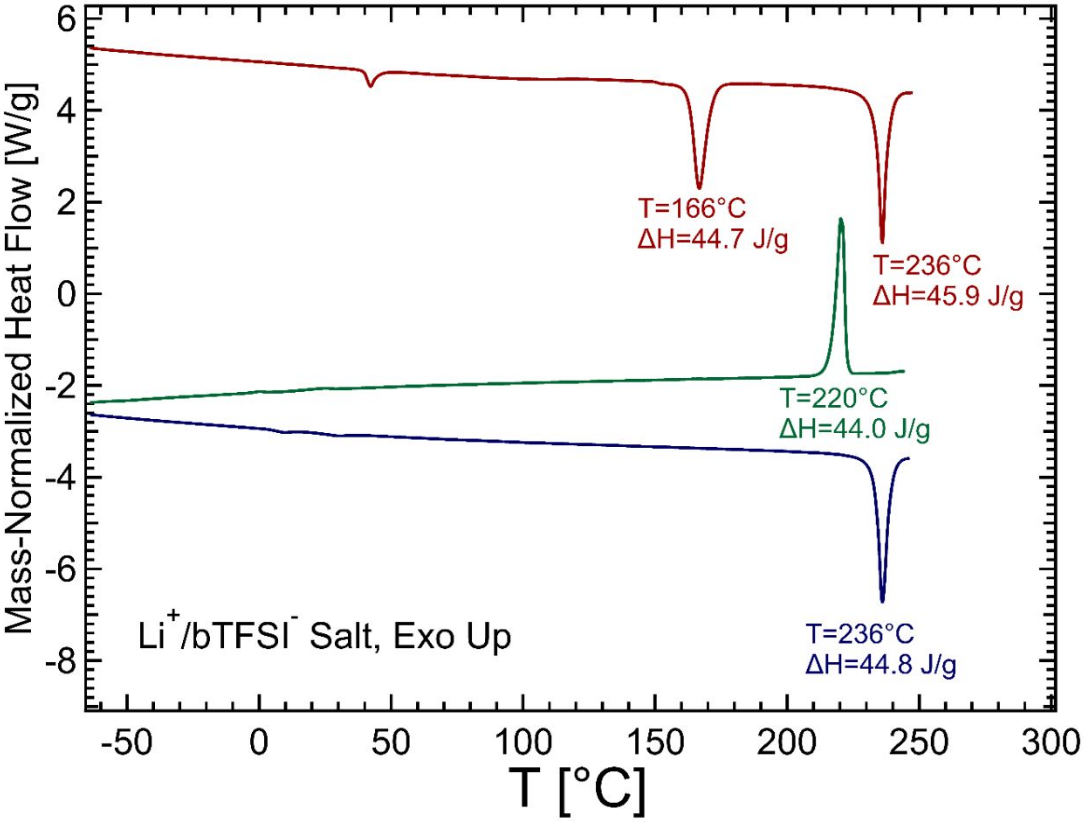

Figure S35: Understanding the melting behavior of the Li^+/$TFSI^-$ salt is important in distinguishing the features seen in the polymer from the salt. The curves are shifted so that the order of scans is chronological when descending. Upon the first heating major endothermic peaks are observed at 166 and 236 °C. According to the literature, these endothermic features can be attributed to a solid-solid transition (reported at 152° C in the literature) and a melting temperature (reported at 234 °C), respectively. An additional peak at 50°C may be an artifact or a feature of some adsorbed species coming off the salt. Upon cooling, a single crystallization feature is observed with an enthalpy that approximately matches the melting enthalpy of the crystals upon heating. A solid-solid transition peak is not observed, likely due to the fast cooling rate of the sample. Upon reheating the sample, the melting feature is observed again, with similar enthalpy to the observed 1st melting enthalpy and crystallization enthalpies. Note that the enthalpies associated with these transitions are approximate (±20%) due to limited resolution in the mass of the sample.

7.3 Melting Behavior of the ZIL

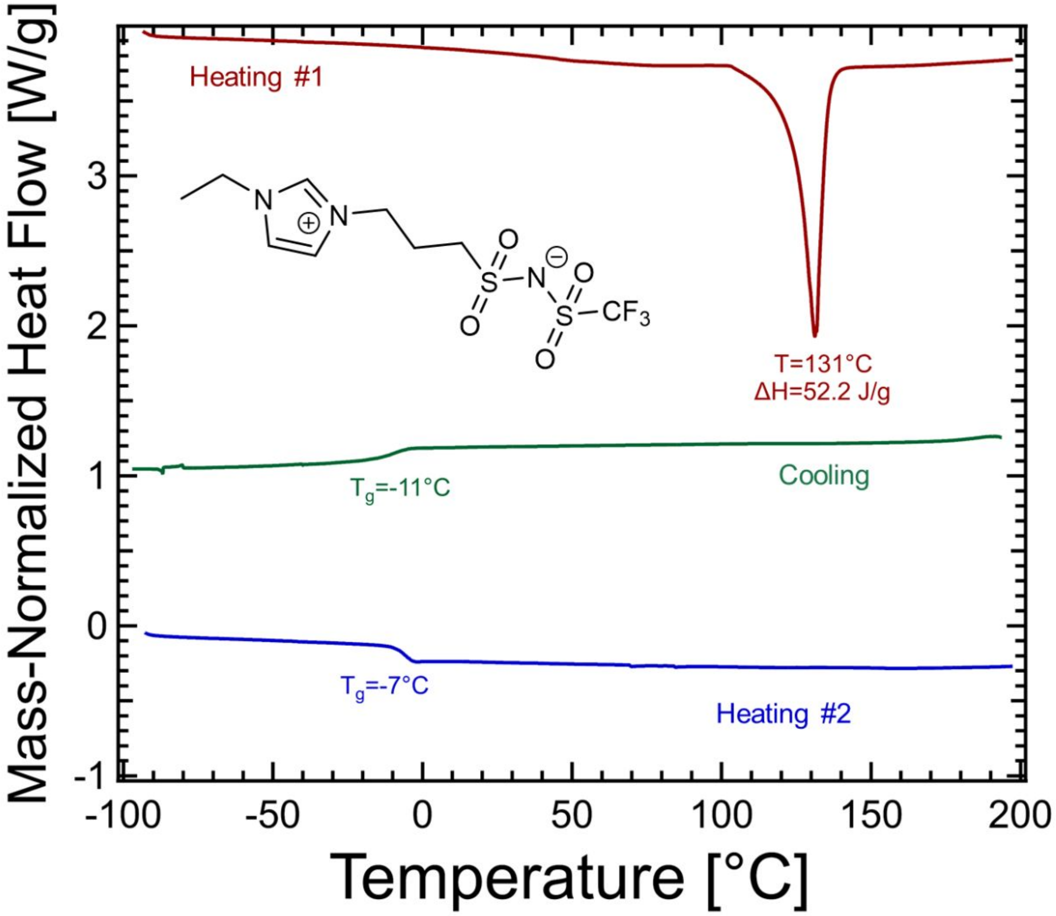

Figure S36: Another useful reference system to consider is the zwitterionic liquid (inset). This above figure shows a heat-cool-heat cycle of this zwitterion small molecule where the curves are formatted so that they are sequential in time as read from top to bottom and the curves have been shifted for clear viewing. The first heating results in a sharp melting transition as may be expected of a crystalline material. However, upon cooling no crystallization peak is observed and the material instead undergoes a glass transition around -11°C. We observe that this amorphous liquid state is maintained within this ZIL for >24 hours but the material eventually converts back to a crystalline solid. The sluggish crystallization kinetics of this molecule are consistent with observations by Ohno et al. that many organic zwitterionic compounds comprised of IL-type salts gradually crystallize, but sometimes take weeks[10] to return to the crystalline state. The sluggish crystallization kinetics of the small molecule ZIL are worth considering in the following analysis of the polymers, which may exhibit even more sluggish crystallization due to the polymer-bound nature of the ZILs. Note that the enthalpy of the crystallization is an approximate value (±20%) due to limited resolution of the sample mass.

7.4 Calorimetric Analysis of PZILs

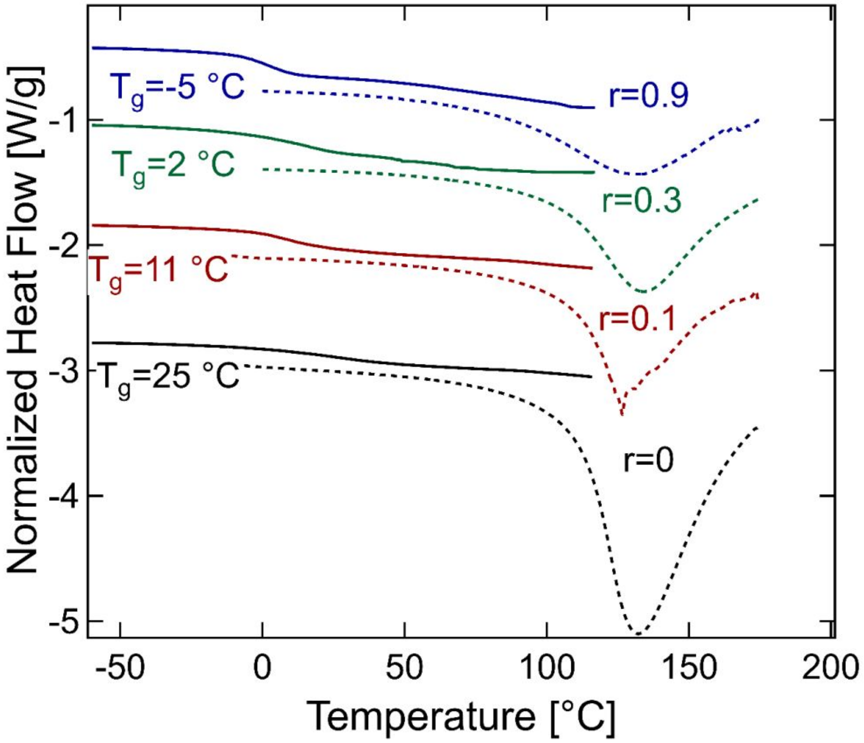

Figure S37: The first pass of the calorimetric cycle is indicated by the dotted line; the second heating is indicated by the solid line. In the first pass, an endotherm is evident for all samples, typically an endotherm in DSC is typical of either 1) a melting temperature or 2) an enthalpy of vaporization of a volatile component. Since there is no removal of any volatile component evident in TGA analysis of the sample and since the samples were thoroughly dried and packed in a glovebox, we conclude that this peak is evidence of crystalline melting. The melting temperatures in all cases are relatively constant at ~130°C. This is remarkably consistent with the melting temperature of the small molecule crystallite. We note again that agreement between the small molecule crystal and the polymer crystal is fortuitous in this case since tethering the molecule to the polymer backbone can change many of its properties. Upon a second heating cycle, only a glass transition is observed. This is consistent with the small molecule ZIL, in which the slow crystallization dynamics prevent the observation of a second melting.

The glass transition temperature observed in the second melting scan may differ significantly from the actual T_g observed in the electrolyte due to the interplay of crystallinity with T_g. Therefore the calorimetric T_g is unlikely to be the T_g experienced within the working polymer electrolyte. Consequently, it is the rheometric T_g which is preferred for all measures of dynamics and is used in the Walden plot of the main paper. Although it is not a central theme of this work, it does bear noting that the trend of salt concentration versus T_g shows that these variables are inversely related for the PZIL. We hypothesize that adding mobile salt charges reduces monomer-monomer interactions and results in faster dynamics, however this trend may bear additional study.

8 Stress Relaxation Experiment

An evident feature of the TTS curves presented in Figure S1 is the appearance of a low-frequency plateau at observed timescales, rather than terminal relaxation behavior. Evidently this inability to fully relax stress at long times is a consequence of the zwitterionic functionalities of the polymer since the linear, ZI-free chain would relax at these timescales. Although this long-time rheological behavior is beyond the scope of the current work, it was briefly probed in the r=0.9 sample via a stress relaxation experiment.

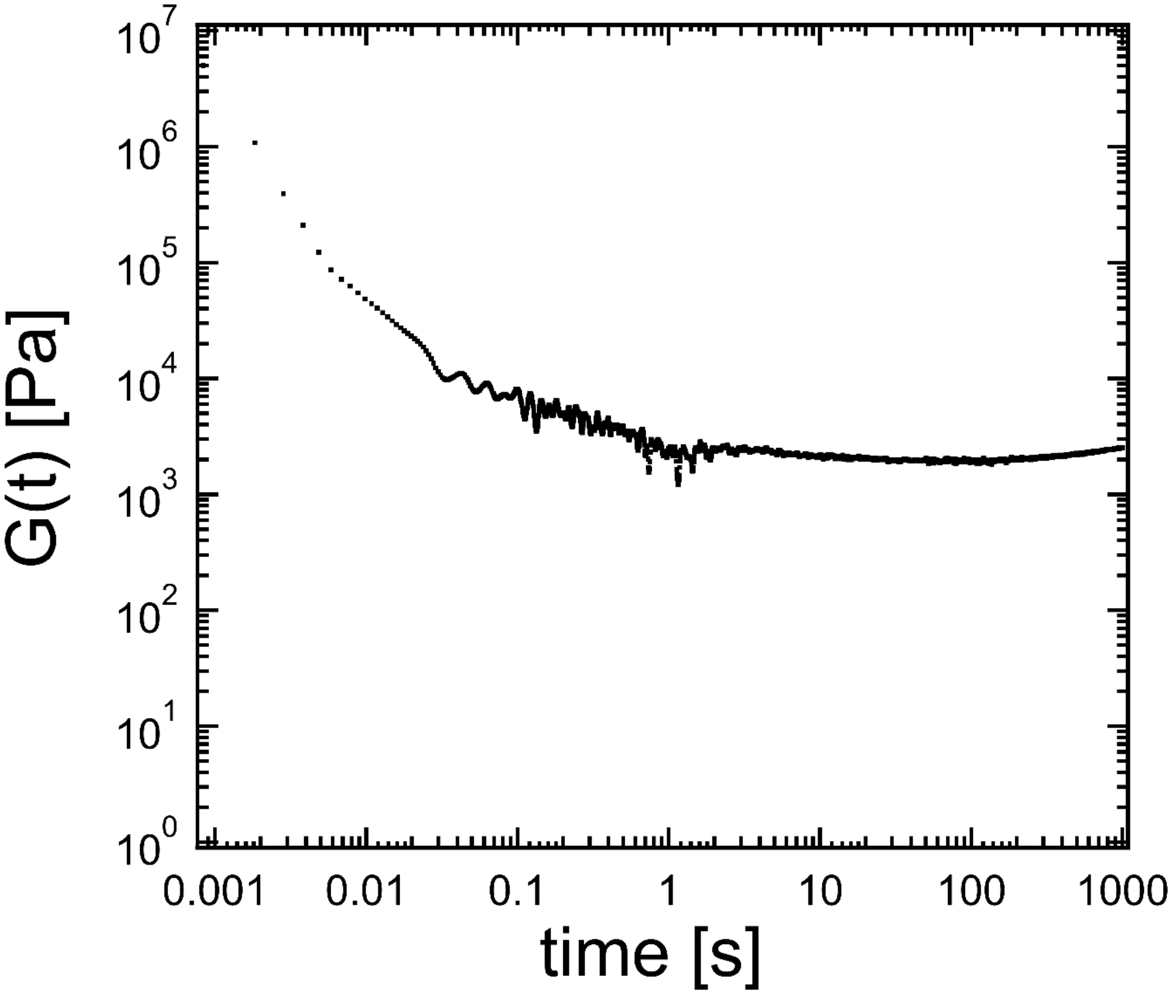

Figure S38: Stress relaxation of this polymer reveals no terminal behavior over a 1000 second window at 70°C. This delay in terminal relaxation could occur from interactions between zwitterions between chains, which are known to transiently crosslink the material. Evidently this crosslinking mechanism is not a permanent one since the polymer could be dissolved into polar organic solvents.

9 Raw Dielectric Spectroscopy Data

Dielectric spectroscopy measurements are used to evaluate the ionic conductivity of the electrolyte. We note that these AC-type measurements only probe the small-lengthscale and are taken in the range of small potentials (<100mV). High performance in these dielectric spectroscopy tests represents a necessary but not sufficient demonstration of the merits of the materials as battery electrolytes in real cells where transport much occur over macroscopic lengthscales (~cm) and at larger potentials (~3-6 V).

9.1 Salt-Free Polymer (r=0)

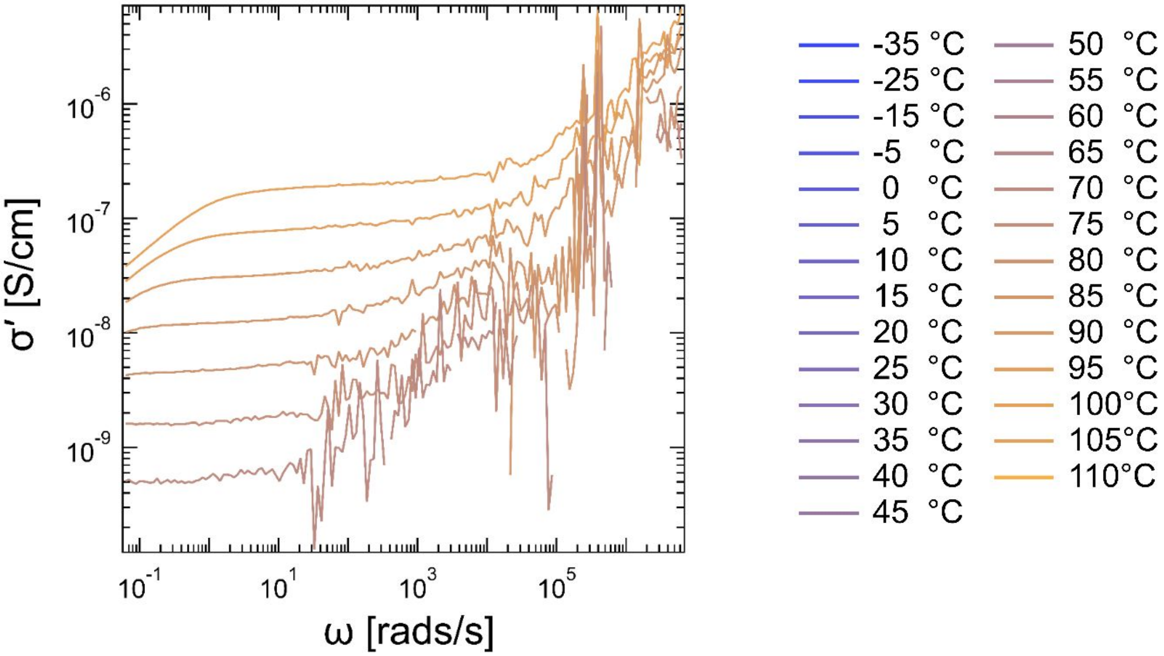

Figure S39: The real part of the conductivity is plotted against frequency for the salt-free polymer. The high frequency data is noisy, but a clear plateau at low frequencies can be observed corresponding to the DC conductivity of the samples. For the salt-free polymer, the loss tangent is not provided as this data is too noisy to be useful. The temperature legend correlates the colors and temperatures of all plots in this section.

9.2 Salt Loading r=0.1

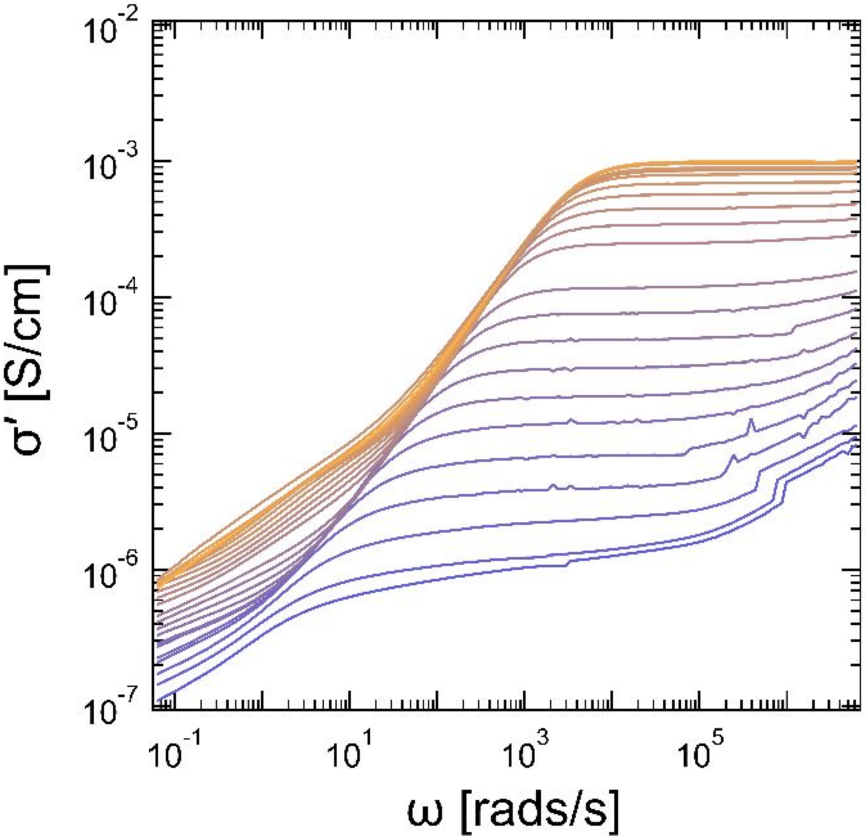

Figure S40: The real component of the conductivity is provided for the r=0.1 sample at temperatures ranging from -30 to 110 °C. A plateau corresponding to the DC conductivity occurs at high frequencies followed by electrode polarization at lower frequencies.

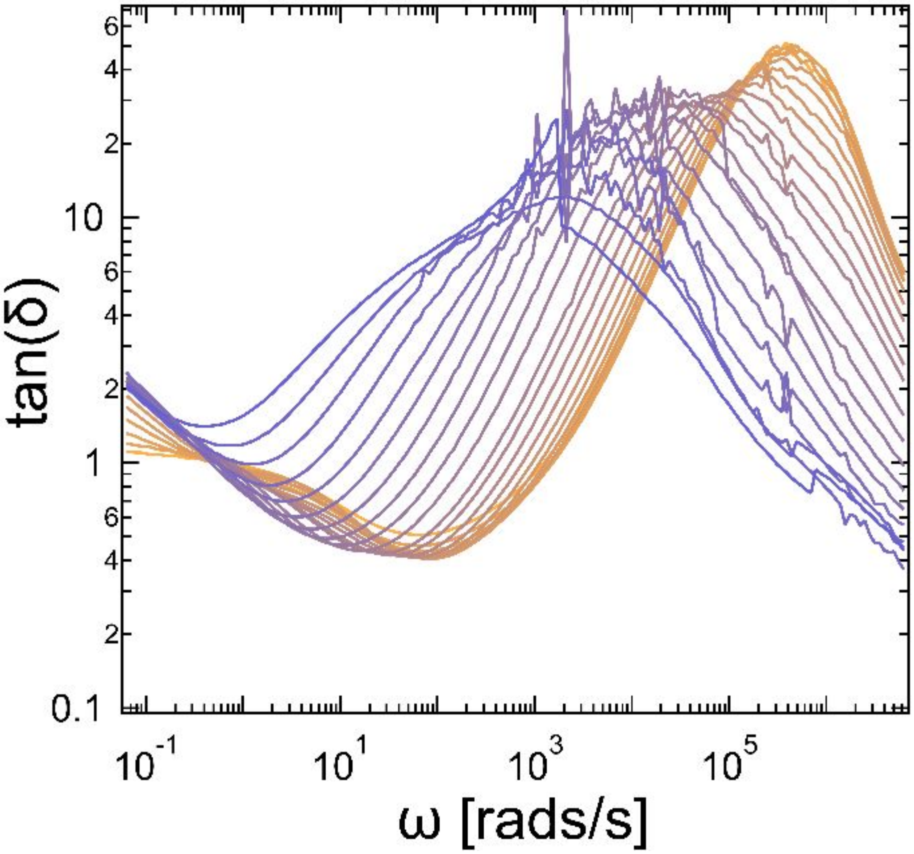

Figure S41: The loss tangent is provided as a function of frequency for the r=0.1 sample at temperatures ranging from -35 to 110 °C. The peak of this loss tangent at values much greater than unity indicates approximate DC behavior.

9.3 Salt Loading r=0.3

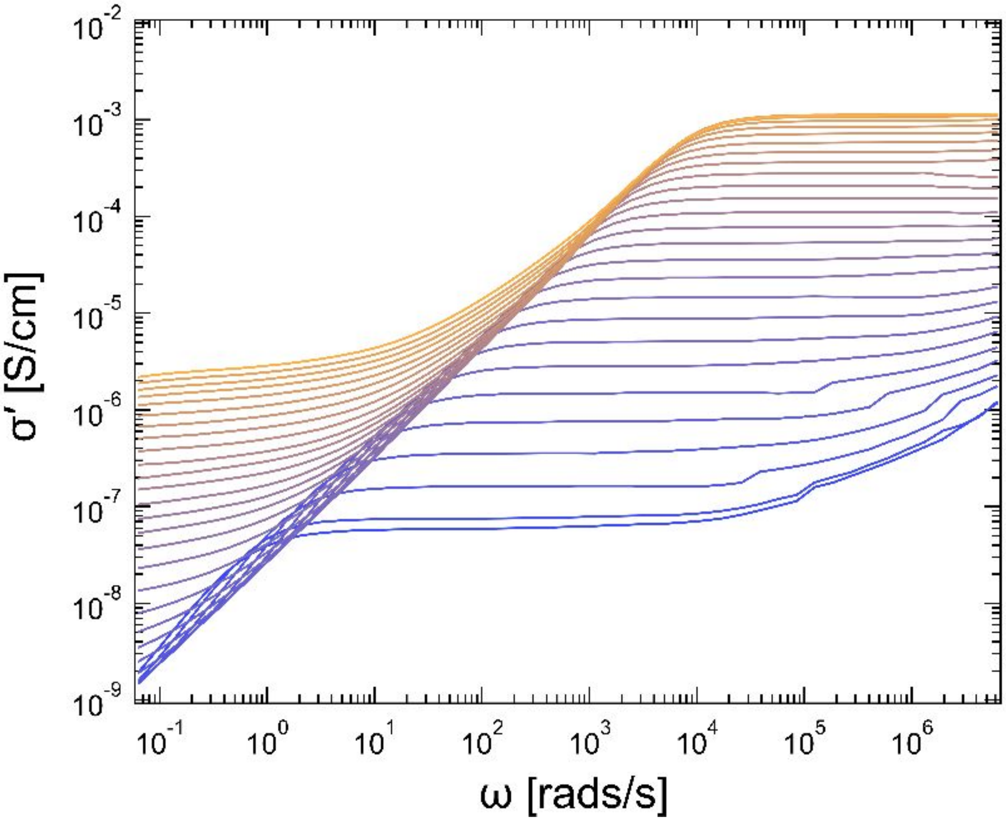

Figure S42: The real component of the conductivity is provided for the r=0.3 sample at temperatures ranging from -35 to 110 °C. A plateau corresponding to the DC conductivity occurs at high frequencies followed by electrode polarization at lower frequencies.

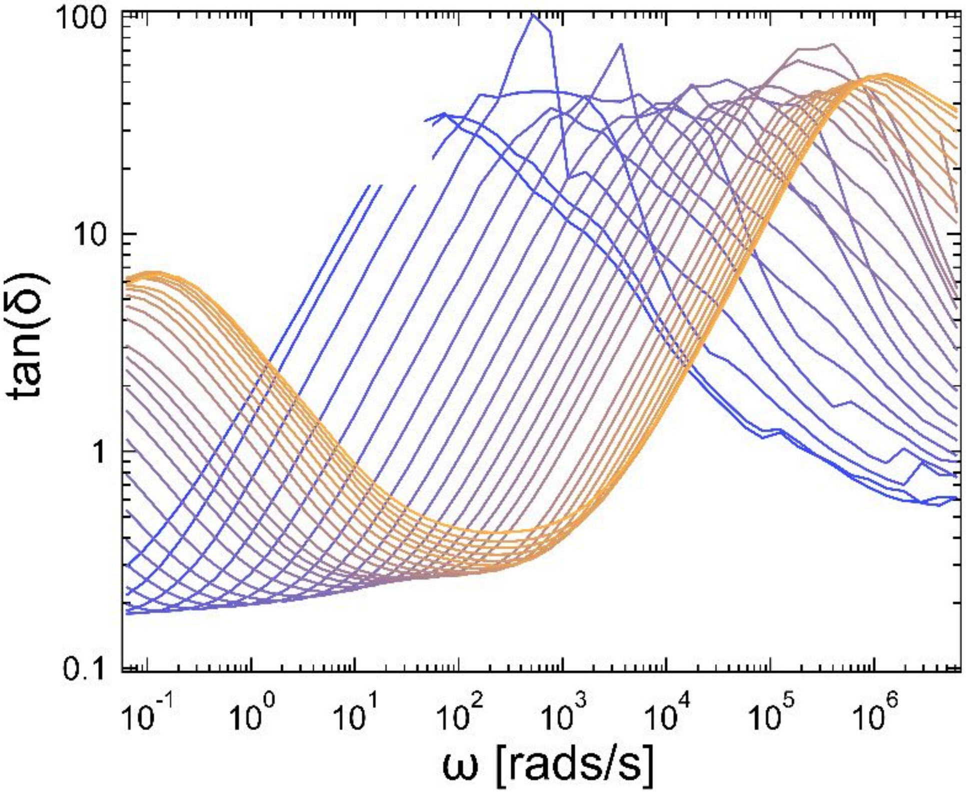

Figure S43: The loss tangent is provided as a function of frequency for the r=0.3 sample at temperatures ranging from -35 to 110 °C. The peak of this loss tangent at values much greater than unity indicates approximate DC behavior.

9.4 Salt Loading r = 0.9

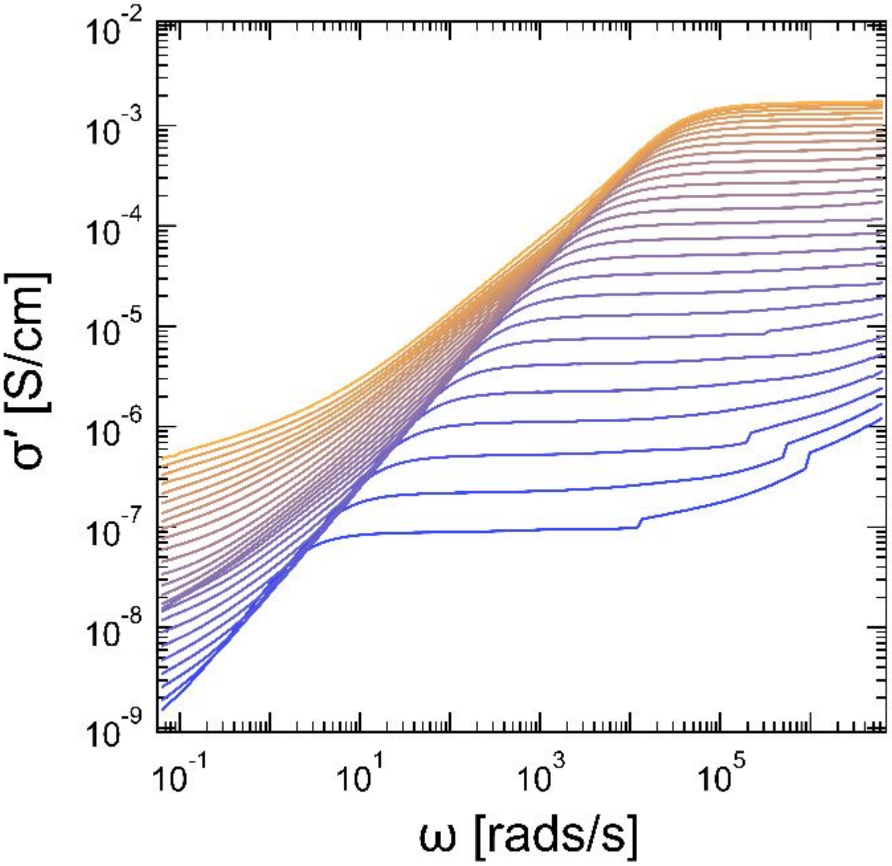

Figure S44: The real component of the conductivity is provided for the r=0.9 sample at temperatures ranging from -35 to 110 °C. A plateau corresponding to the DC conductivity occurs at high frequencies followed by electrode polarization at lower frequencies.

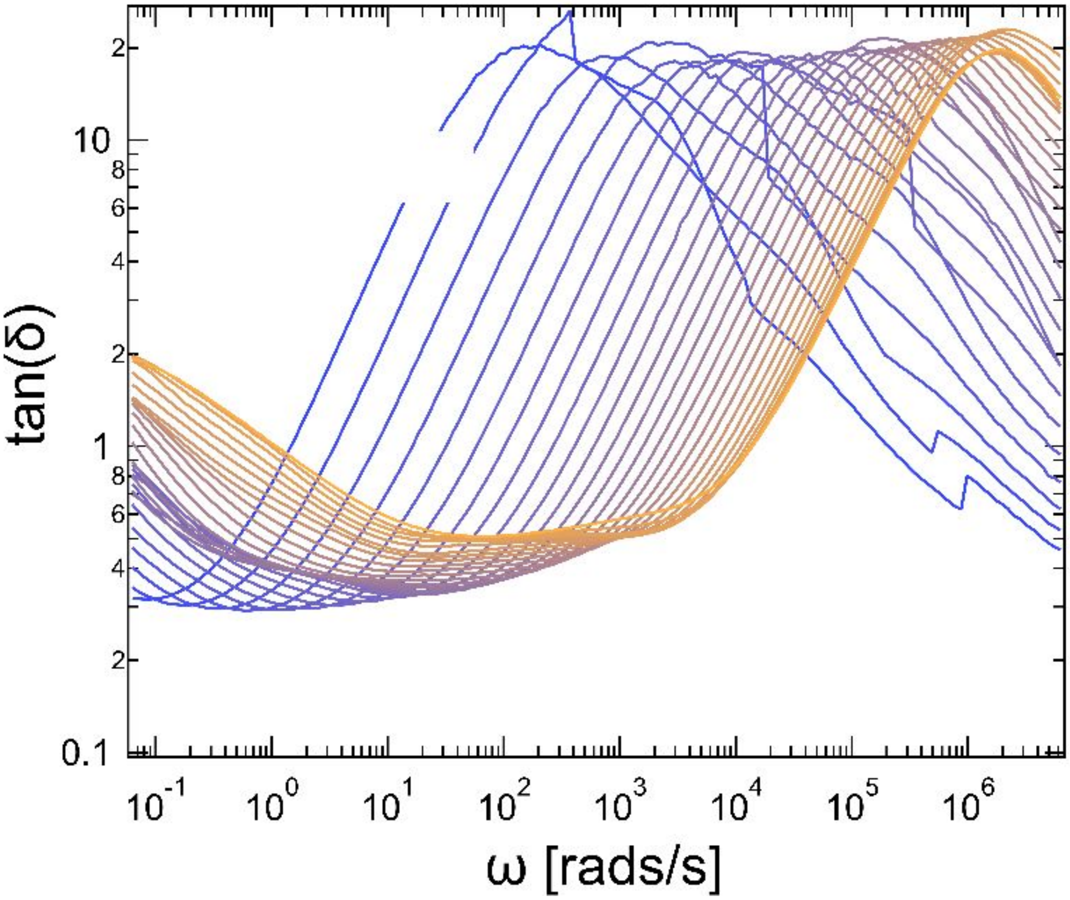

Figure S45: The loss tangent is provided as a function of frequency for the r=0.3 sample at temperatures ranging from -35 to 110 °C. The peak of this loss tangent at values much greater than unity indicates approximate DC behavior.

10 NMR Spectra

The NMR spectra in this section are cropped to focus on the relevant chemical shift regimes, no peaks were cropped from the spectra even when a limited chemical shift regime is shown. Solvation of the zwitterions by a single deuterated solvent was not always practical due to the unfavorable solvation of the zwitterions, consequently a secondary solvent was sometimes added to improve the solubility for analytical purposes only.

10.1 NMR Spectrum of Crude NHS Acrylate Polymer

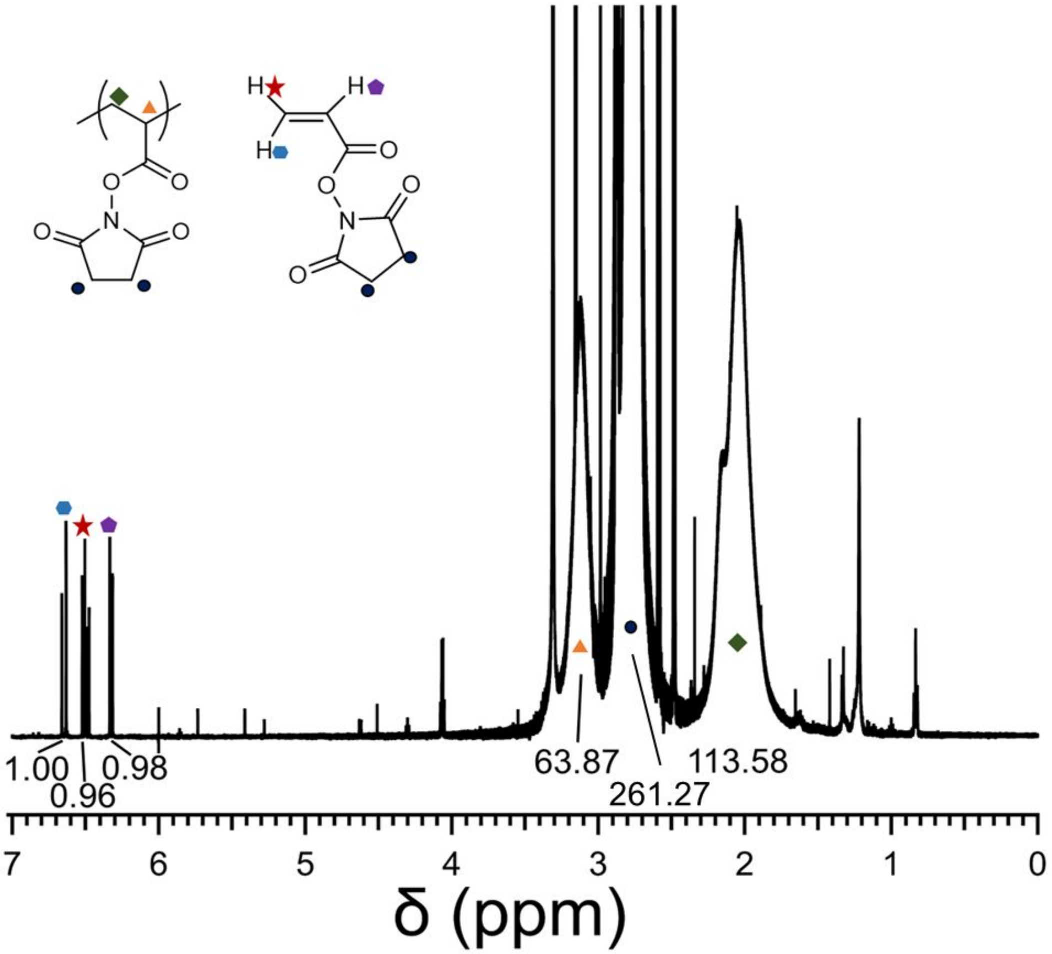

Figure S46: Crude ^{1}H NMR of the NHS ester acrylate after polymerization. The conversion of the polymerization is evaluated by comparison of the vinyl monomer peaks with the backbone peaks of the polymer (◆) to be 0.991. The corresponding number average degree of polymerization 248 and a molar mass of 42 kg/mol.

10.2 NMR of Purified NHS Acrylate Polymer

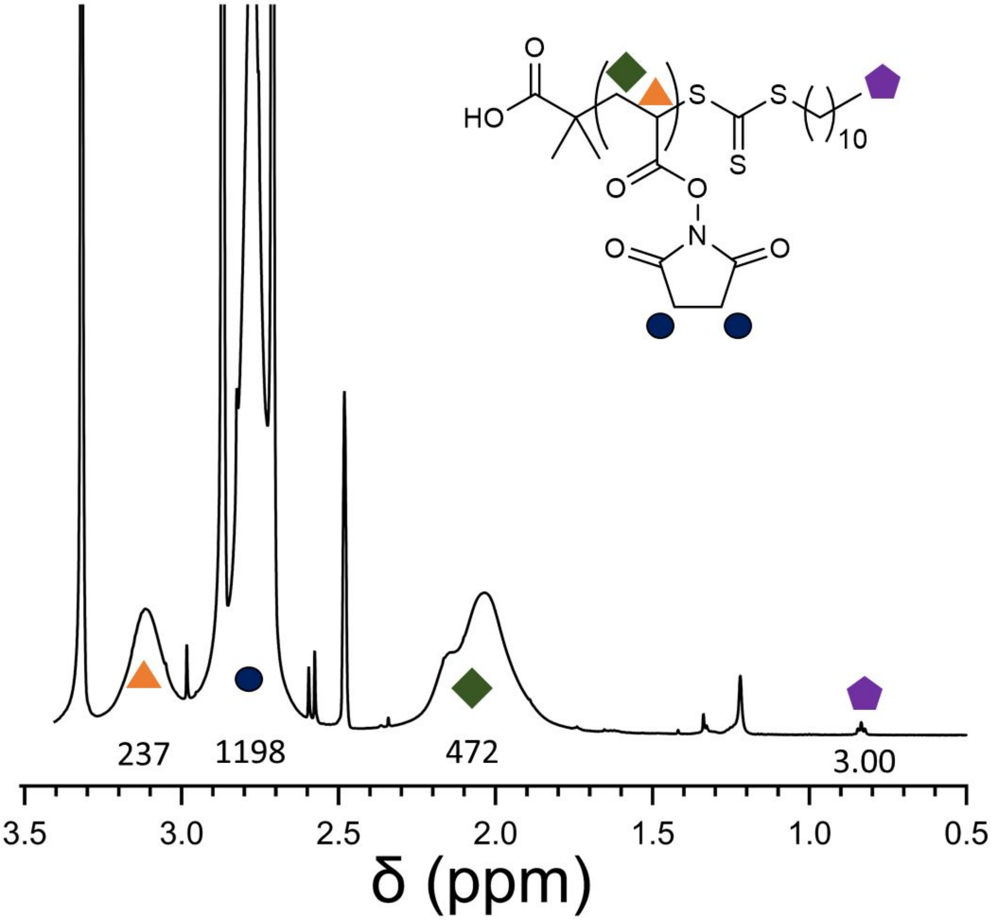

Figure S47: End group analysis based on the anticipated chain end of this polymer from idealized RAFT polymerization gives a number average degree of polymerization of 236.5, which corresponds to a number averaged molar mass of 40 kg/mol.

10.3 NMR of TFSI Br

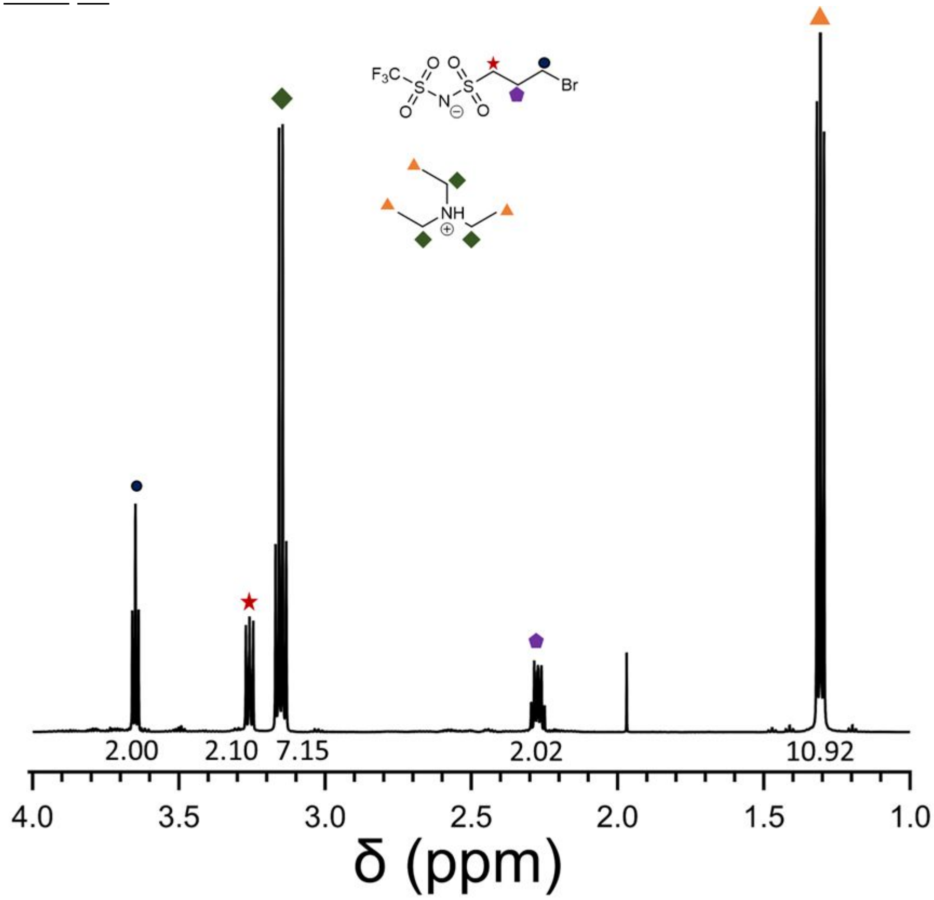

Figure S48: TFSI-Bromide compound after washes. Some excess triethylamine remains. Though the compound could be isolated more carefully by recrystallization of a version with an alternative counterion such as lithium or potassium, the triethylamine counterion is preferred in this case because counterion removal can be easily monitored by ^{1}H NMR.

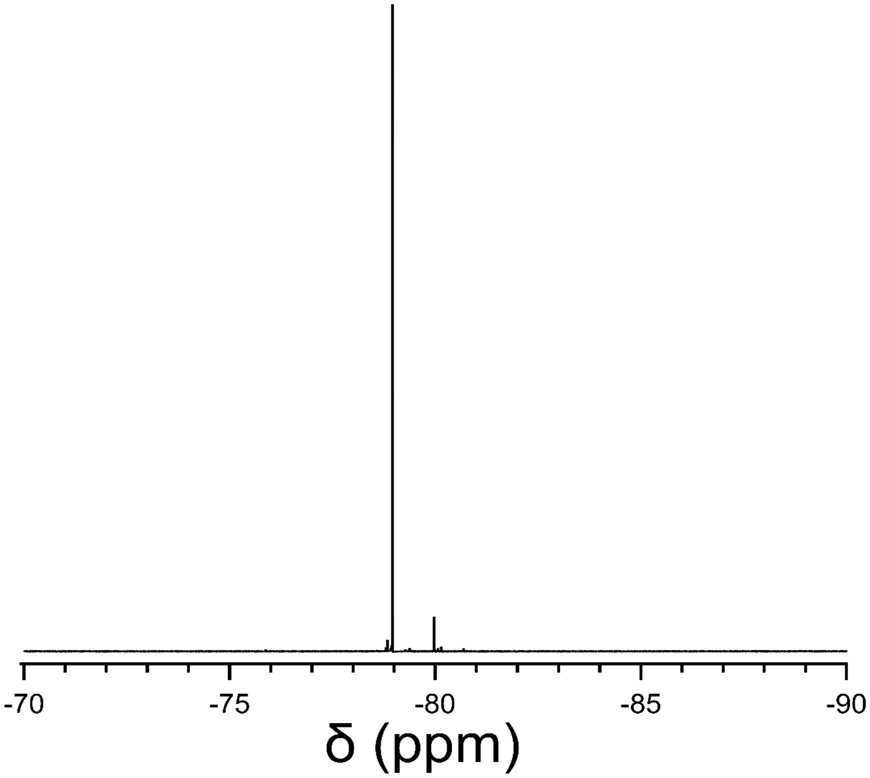

Figure S49: The preparation of the fluorine compound cannot be confirmed by ^{1}H NMR since no protons undergo a significant chemical shift upon conversion from the acid chloride to the TFSI product. The above spectrum is the ^{19}F 1D NMR of the small molecule. The presence of a fluorine peak at a chemical shift consistent with previous reports[11] is used instead to confirm the preparation of the correct product.

10.4 NMR of Imidazole Functionalized Polymer

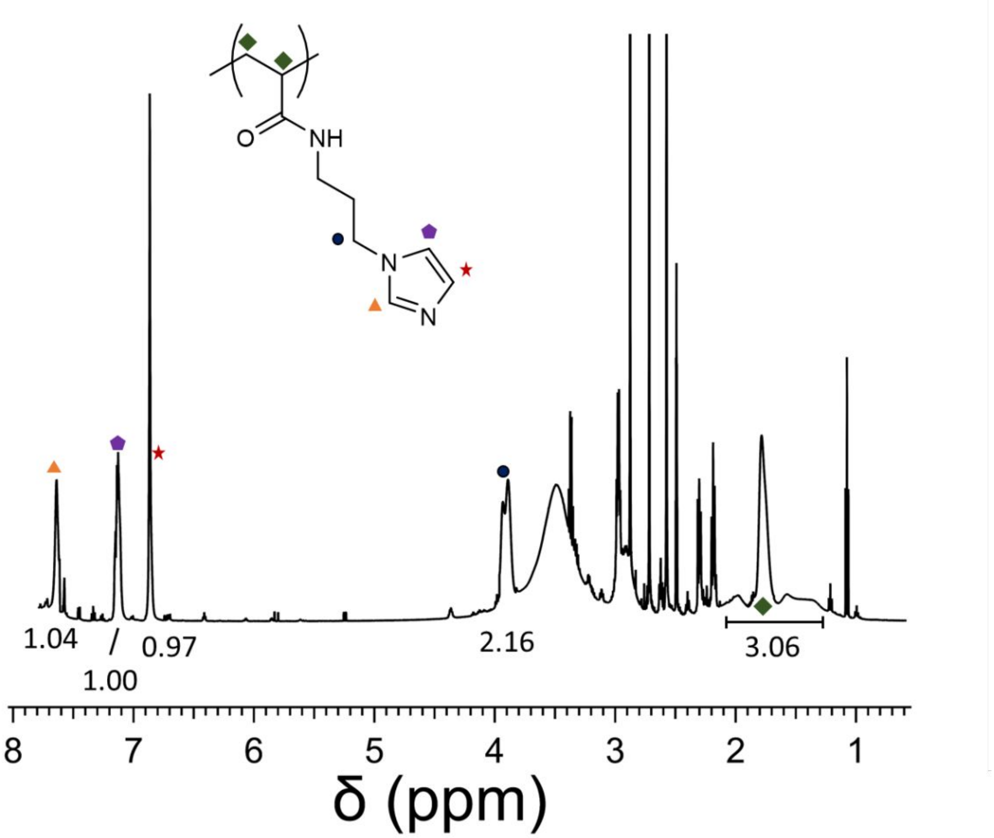

Figure S50: This ^{1}H NMR spectrum was taken of an aliquot of the polymer after the imidazole addition reaction had been allowed to proceed for 18 hrs. Polymer was isolated from this sample by reverse precipitation in dielthyl ether. The presence of imidazole peaks in good agreement with the integration for backbone peaks suggests that this crude sample has successfully undergone replacement of the NHS-acrylate group with aminopropyl imidazole. The crude peaks in this sample will be removed in subsequent dialysis steps after the conversion of the polymer to the zwitterionic form. The presence of a peak corresponding to the amide group is not present on this spectrum, presumably this is because this proton can exchange with the deuteriums from the deuterated methanol solvent.

10.5 NMR of Washed Product Polymer

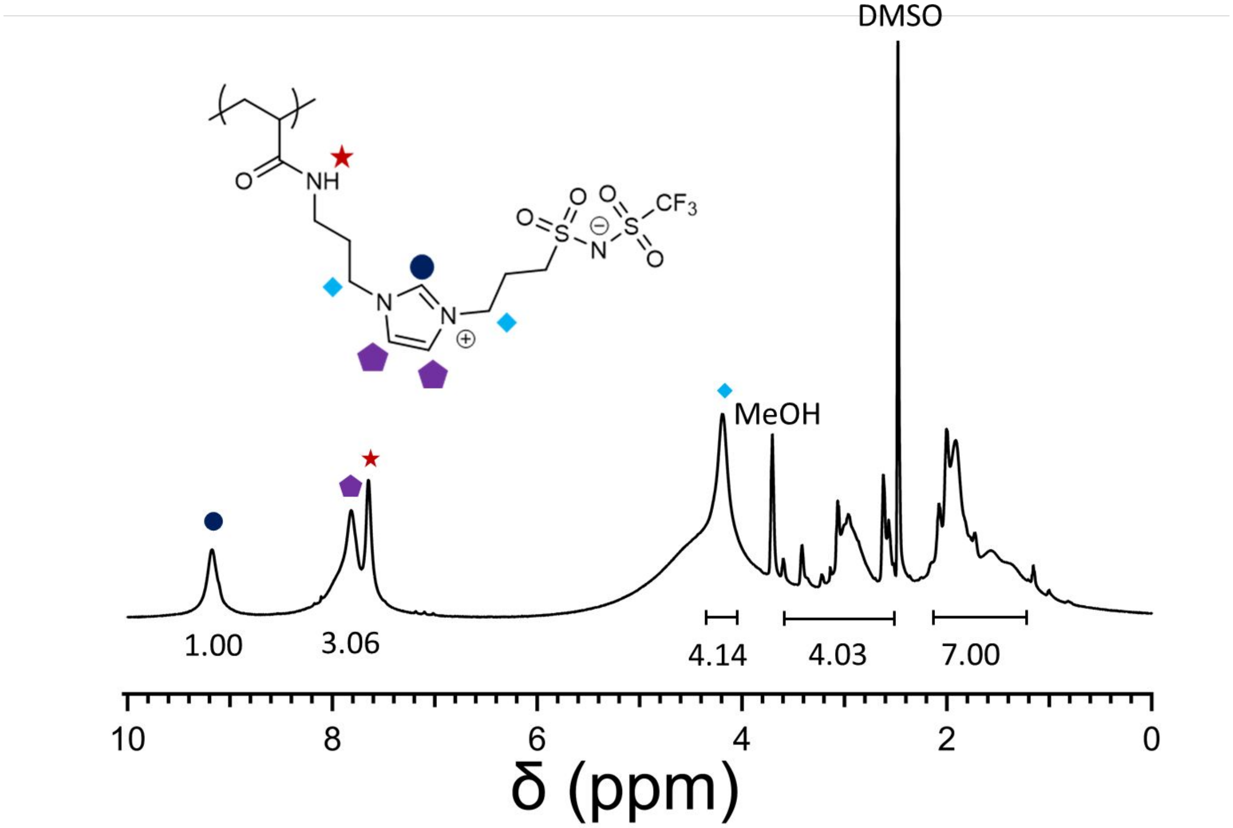

Figure S51: The ^{1}H NMR spectrum of the polymer indicates quantitative conversion of the imidazole polymer to the PZIL as suggested by the downfield shift of the proton at the 2-position of the ring consistent with deshielding as a result of aromatizing imidazole to imidazolium. Simultaneously, the protons at the 4 and 5 positions merge and shift downfield. The presence of an additional peak at 7.8 ppm is attributed to the amide peak, which was previously silenced in the d-MeOH, but is not silenced in this NMR, which was collected using d-DMSO as a solvent, which will not undergo much proton exchange. The lack of TEA peaks in this spectrum suggests quantitative removal of excess salts. Though the peaks upfield are broad and difficult to assign individually, their total integration suggests agreement with the anticipated structure. The presence of end group peaks at ~1ppm is still evident in this spectrum indicating that side-reaction of the end group has not occurred.

10.6 NMR of Zwitterionic Liquid

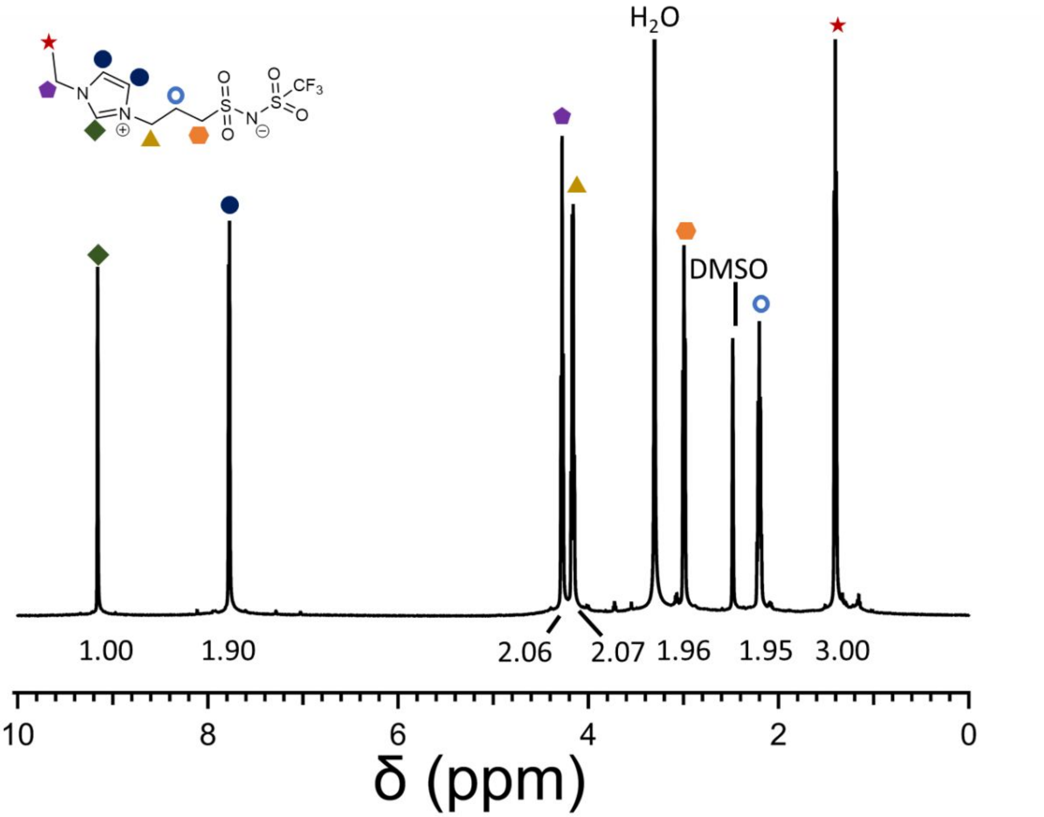

Figure S52: The ^{1}H NMR of this compound follows splitting patterns consistent with the proposed structure. NMR is taken on the sample prior to final drying. Residual water in the sample is consistent with the observed hydroscopic nature of the zwitterion, though no water is used in the purification steps.

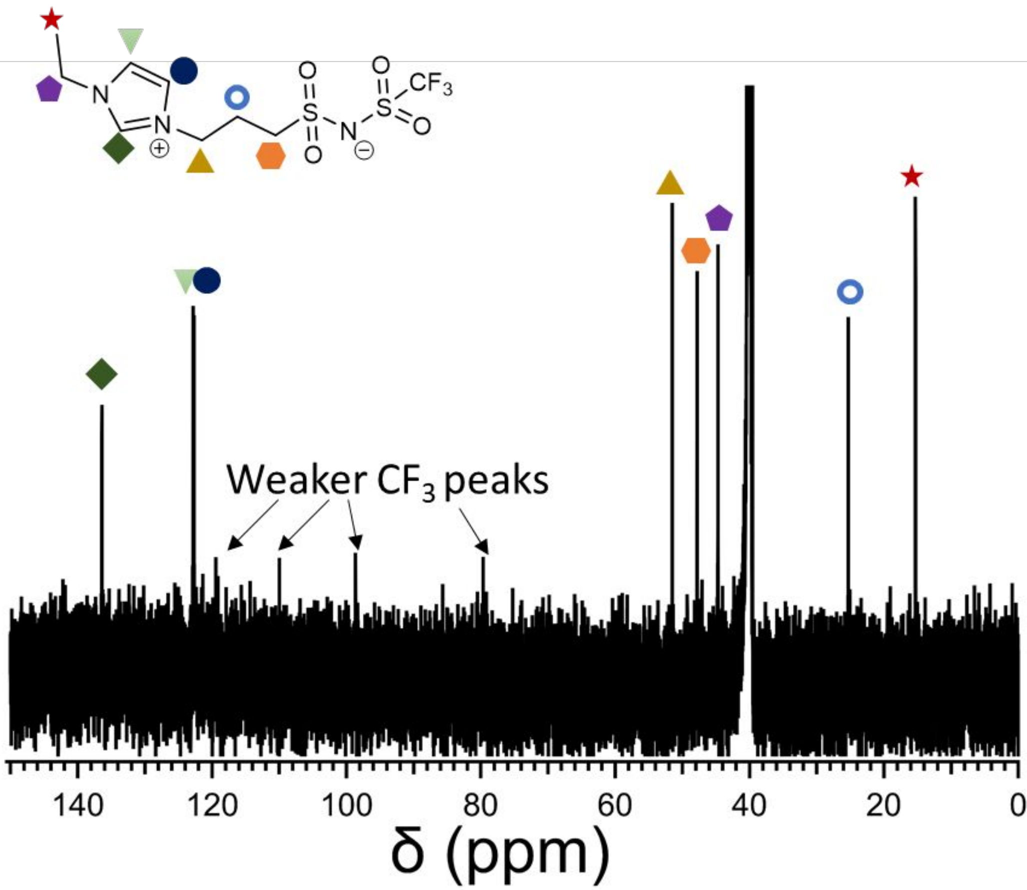

Figure S53: ^{13}C NMR shows peaks correspondent with the ZIL molecule. The CF_3 signal is triply split by the presence of fluorines, resulting in four evident signals corresponding to this carbon. The large peak at 40ppm corresponds to d-DMSO.

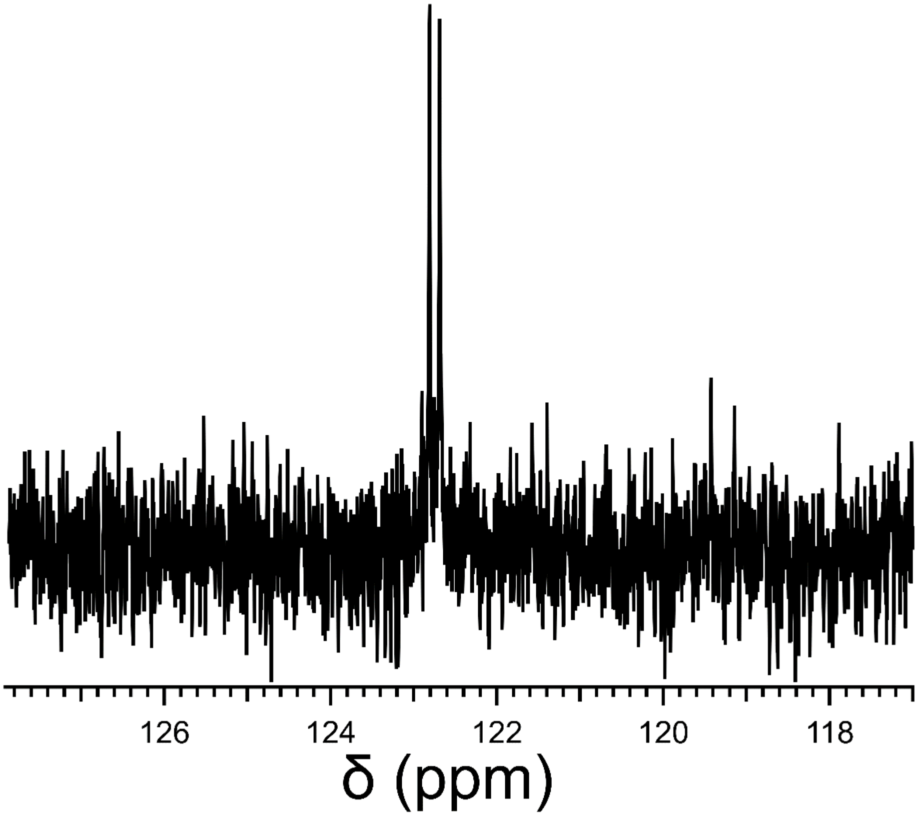

Figure S54: This figure shows a zoomed in region of the NMR spectrum above, it is presented here to demonstrate that there are two distinct signals near 123 ppm, a feature that is difficult to decipher in the zoomed-out spectrum.

10.7 NMR of Crude PDMAEA

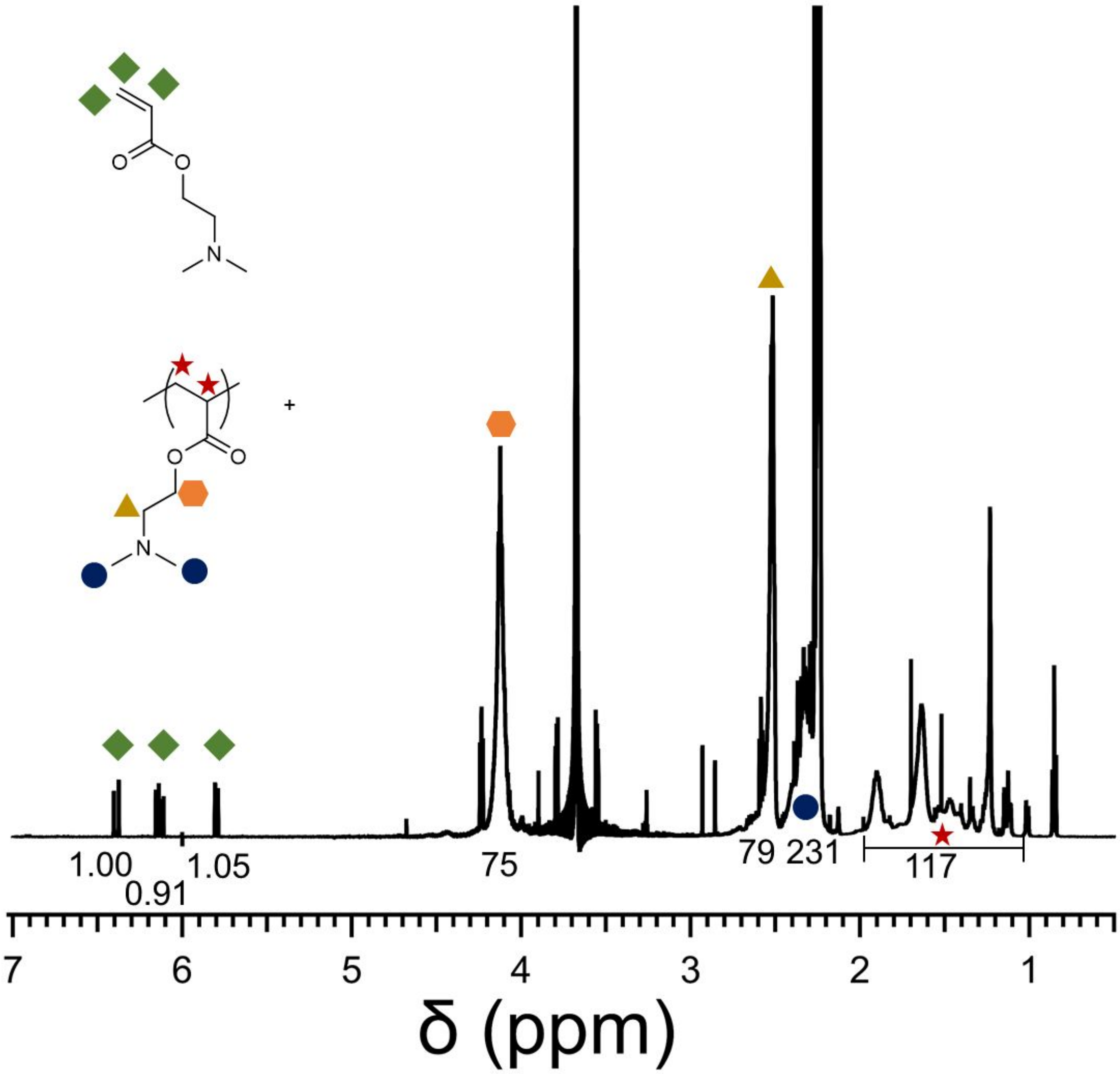

Figure S55: The conversion of the reaction is evaluated from analysis of the crude reaction product using the comparison of monomer vinyl peaks to the hydrogen signals from the carbon adjacent to the ester (orange hexagon). The conversion after 18hrs was nearly complete at 97.5%. Based on this conversion, a molar mass can be estimated assuming that each chain is initiated from a RAFT initiator. This estimate yields: $N_N = 243$, $M_N = 34.8$ kg/mol.

10.8 NMR of Purified PDMAEA

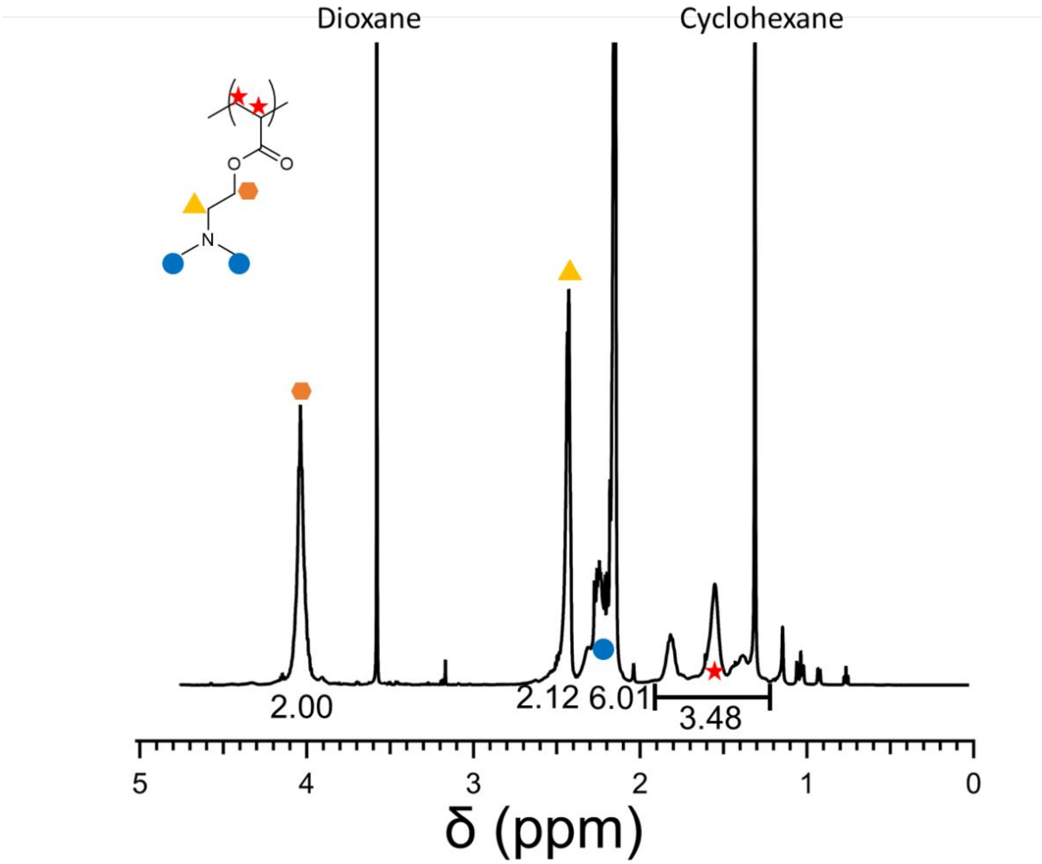

Figure S56: The precipitated polymer after drying for 24 hours at room temperature shows some residual solvent. This solvent is rigorously removed in the final steps but is not rigorously removed here since the polymer needs to be redissolved for post-polymerization functionalization reactions. The peaks characteristic of the polymer are observed in expected peak positions and in expected ratios. The backbone peaks integrate to a slightly higher intensity than anticipated (3.48 vs 3.00) due to the presence of the cyclohexane peak in this integral region.

The end group signal corresponding to the methyl chain end of the dodecyl group (t, δ=0.77 ppm) has an intensity ratio with the protons alpha to the ester of the repeat unit (b, δ=0.4.04 ppm) of 3/449, which corresponds to: $N_N = 224.5$, $M_N = 32.1$ kg/mol. This is in good agreement with estimates of polymer size from the crude NMR.

10.9 NMR of Purified Am-TFSI PZIL

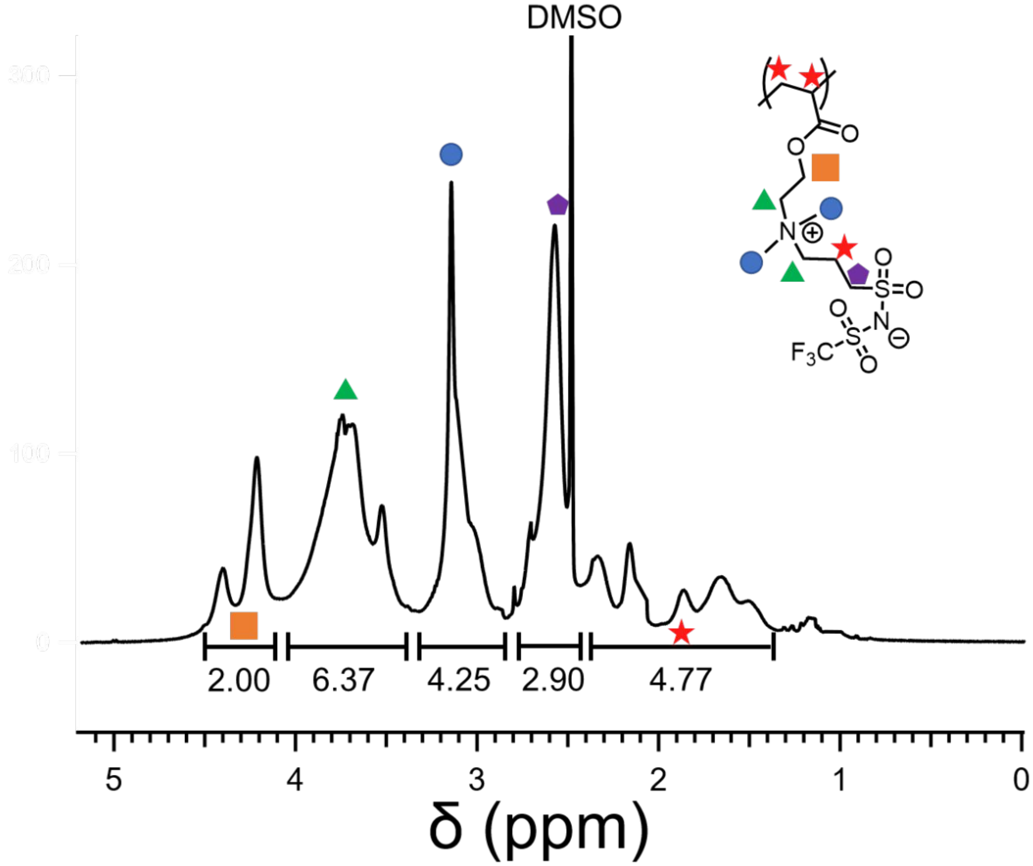

Figure S57: Upon quaternization of the neutral PDMAEA to the zwitterionic polymer, the most prominent proton signal at δ=2.2 ppm shifts downfield, suggesting quantitative conversion of the tertiary nitrogen to a quaternary form. This NMR was taken after drying the sample. The integration value of the peak corresponding to the purple hexagon is likely due to the convolution of DMSO and polymer peaks.

10.10 NMR of Cl-SA-C6F5

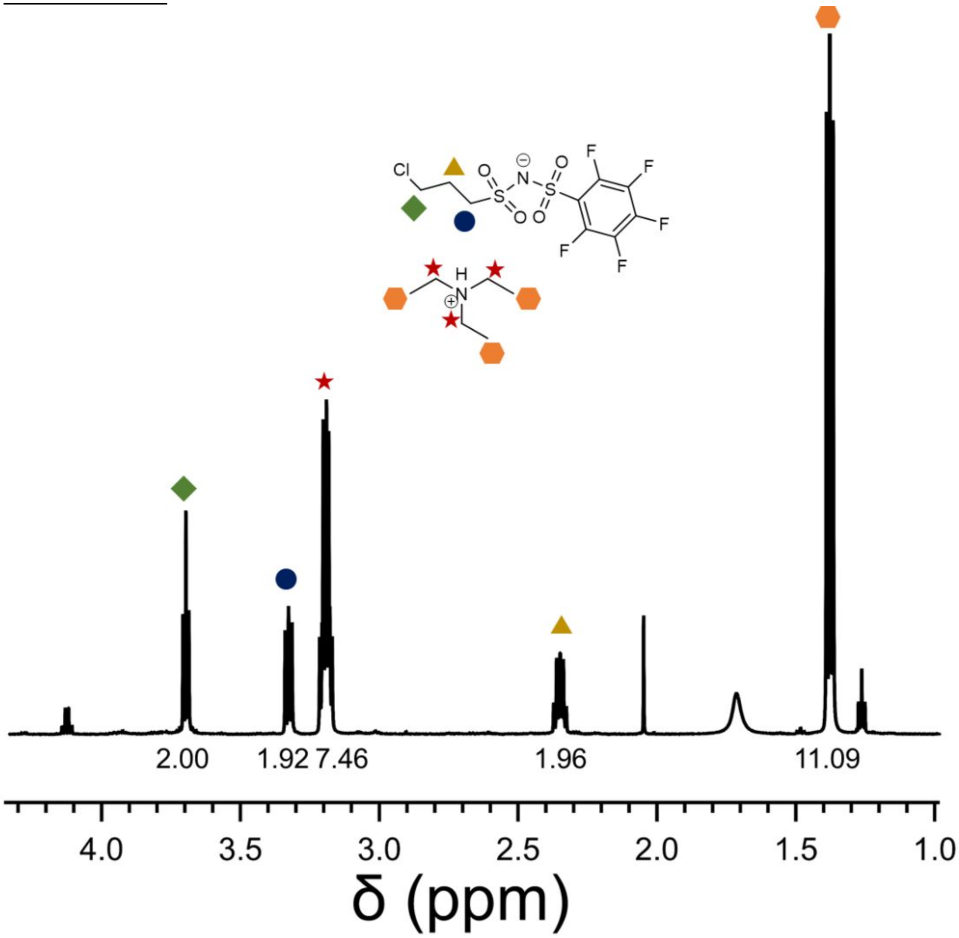

Figure S58: ^{1}H NMR shows the presence of the three peaks corresponding to the alkyl tail with expected splitting. Triethylamine is in slight excess, but this ion is removed in purification of the PZIL in a subsequent step.

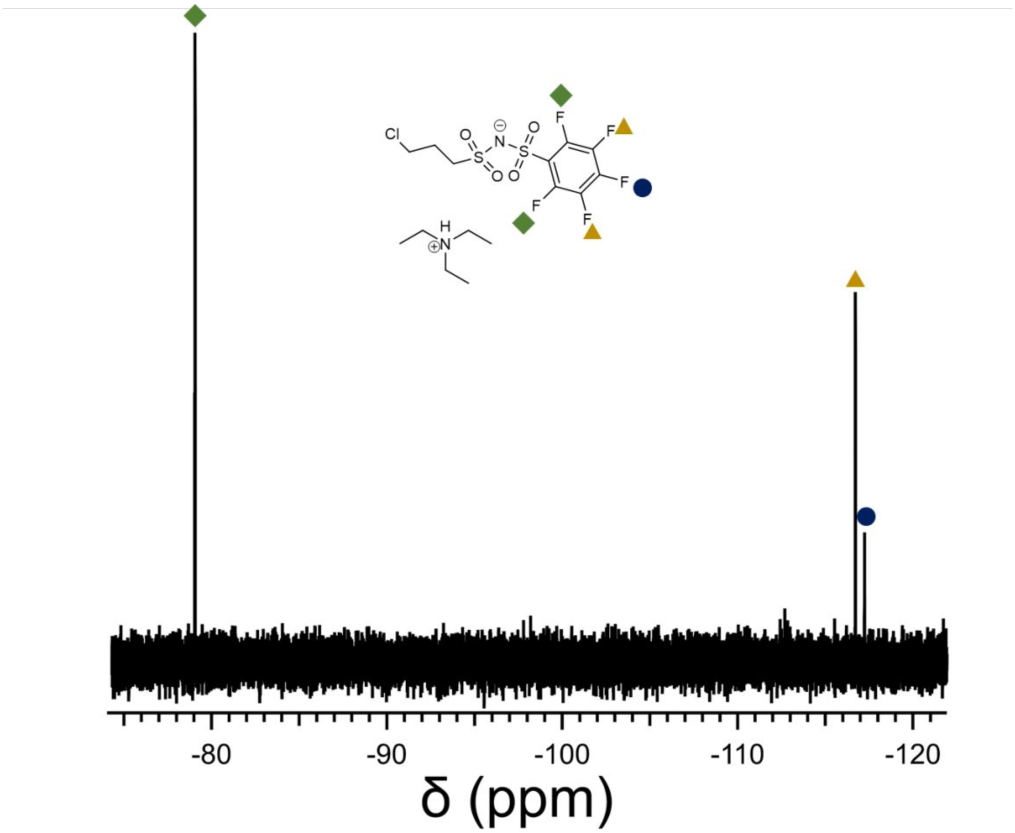

Figure S59: ^{19}F NMR demonstrates the presence of the three signal expected for the pentafluorphenyl group. The presence of the pentafluorophenyl group in the organic phase suggests that these fluorine signal come from the intended product.

11 Size Exclusion Chromatography

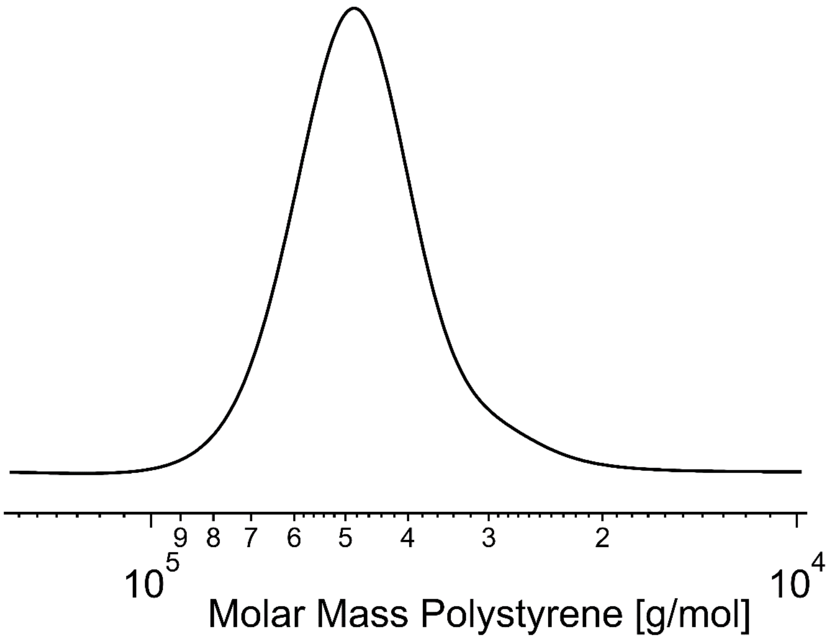

Figure S60: The normalized intensity is plotted against the calibrated equivalent mass of a narrow polystyrene standard.

Size exclusion chromatography (SEC) was performed on poly(N-(3-(1H-imidazol-1-yl)propyl)acrylamide) to determine the breadth of the molar mass distribution. The curve above shows the refractive index signal versus the calibrated molar mass of narrow polystyrene standards. The molecular mass data may be summarized in Table S1.

Table S17: The molecular weight of the polymer prior to conversion to the zwitterionic form estimated by NMR and SEC.

$M_{N,NMR}$ [a] [kDa]	$M_{N,SEC}$[b] [kDa]	Đ[b]
42.4	44.1	1.13

[a] Calculated by end-group analysis, assuming complete conversion of the NHS ester functionality

[b] Calculated assuming polystyrene standards, deviation from true molecular weight is anticipated since polystyrene may not be representative of the hydrodynamic volume occupied by this polymer.

1. Seamus D. Jones, Nicole S. Schauser, Glenn H. Fredrickson, Rachel A. Segalman, The Role of Polymer-Ion Interaction Strength on the Viscoelasticity and Conductivity of Solvent-Free Polymer Electrolytes. Macromolecules, (2020).
2. J. Wuttke, Laplace–Fourier Transform of the Stretched Exponential Function: Analytic Error Bounds, Double Exponential Transform, and Open-Source Implementation “libkww”. Algorithms **5**, 604-628 (2012).
3. Q. Chen, C. Huang, R. A. Weiss, R. H. Colby, Viscoelasticity of Reversible Gelation for Ionomers. Macromolecules **48**, 1221-1230 (2015).
4. T. N. T. Phan et al., Vinyl monomers bearing a sulfonyl(trifluoromethane sulfonyl) imide group: synthesis and polymerization using nitroxide-mediated polymerization. Polymer Chemistry **7**, 6901-6910 (2016).
5. H. Ohno, M. Yoshizawa-Fujita, Y. Kohno, Design and properties of functional zwitterions derived from ionic liquids. Physical Chemistry Chemical Physics **20**, 10978-10991 (2018).
6. O. L. Anderson, D. A. Stuart, Calculation of Activation Energy of Ionic Conductivity in Silica Glasses by Classical Methods. Journal of the American Ceramic Society **37**, 573-580 (1954).
7. D. McElfresh, D. G. Howitt, Activation Enthalpy for Diffusion in Glass. Journal of the American Ceramic Society **69**, C-237-C-238 (1986).
8. E. W. Stacy et al., Fundamental Limitations of Ionic Conductivity in Polymerized Ionic Liquids. Macromolecules **51**, 8637-8645 (2018).
9. A. Osaka, K. Takahashi, K. Ariyoshi, The elastic constant and molar volume of sodium and potassium germanate glasses and the germanate anomaly. Journal of Non-Crystalline Solids **70**, 243-252 (1985).
10. Y. Tian et al., Compatibility issues between electrodes and electrolytes in solid-state batteries. Energy & Environmental Science **10**, 1150-1166 (2017).